

The Dispersed Matter Planet Project Sample - Detection limits, Occurrence Rates and New Planets

Matthew R. Standing,^{1,2*} John R. Barnes,² Carole A. Haswell,² Adam T. Stevenson,^{2,3} João P. Faria,⁴ Erwan Quintin,¹ Zachary O. B. Ross,² Luca Fossati,⁵ James S. Jenkins,^{6,7} Douglas Alves,⁸ Daniel Staab²

¹European Space Agency (ESA), European Space Astronomy Centre (ESAC), Camino Bajo del Castillo s/n, E-28692 Villanueva de la Cañada, Madrid, Spain

²School of Physical Sciences, The Open University, Milton Keynes MK7 6AA, UK

³School of Physics & Astronomy, University of Birmingham, Edgbaston, Birmingham B15 2TT, UK

⁴Observatoire Astronomique de l'Université de Genève, Chemin Pegasi 51, CH-1290 Versoix, Switzerland

⁵Space Research Institute, Austrian Academy of Sciences, Schmiedlstraße 6, 8042 Graz, Austria

⁶Instituto de Estudios Astrofísicos, Facultad de Ingeniería y Ciencias, Universidad Diego Portales, Av. Ejército 441, Santiago, Chile

⁷Centro de Astrofísica y Tecnologías Afines (CATA), Casilla 36-D, Santiago, Chile

⁸Departamento de Astronomía, Universidad de Chile, Casilla 36-D, Santiago, Chile

Accepted 2026 February 18. Received 2026 February 18; in original form 2026 January 08

ABSTRACT

DMPP is a radial-velocity survey that aims to detect planets around stars exhibiting anomalous activity signatures, consistent with the presence of close-in evaporating planets. Here, we report the discovery of 7 new planetary signals in 5 different systems: DMPP-2 c & d, HD 67200/DMPP-6 b & c, HD 118006/DMPP-7 b, HD 191122/DMPP-8 b, and HD 200133/DMPP-9 b. We update the orbital parameters of the DMPP-1, DMPP-2, and DMPP-3 systems, along with those of the planetary systems orbiting HD 181433, HD 39194, and HD 89839. We derive detection limits for all 24 targets in our sample with adequate observational coverage, and test the DMPP hypothesis by calculating the occurrence rates for planets in this configuration. We find that the occurrence rates of planets in our sample with orbital periods shorter than 50 d and masses in the range 3–10 M_{\oplus} are $83.0^{+27.1}_{-24.4}$ %, for 10–30 M_{\oplus} are $27.0^{+15.0}_{-11.2}$ %, and for 30–100 M_{\oplus} are $13.9^{+11.8}_{-7.5}$ %. This is significantly higher than the occurrence rates reported by other radial velocity surveys, providing strong support for the DMPP hypothesis.

Key words: techniques: radial velocities – stars: low-mass – software: simulations – planets and satellites: detection

1 INTRODUCTION

The two most prolific exoplanet discovery methods to date, radial velocities (RVs) and transits, are generally applied with no significant *a priori* knowledge of the properties of the planets the target stars are likely to host. RVs were initially collected for FGK stars in the hope of detecting planets akin to the Solar System's giant planets on orbits exceeding 1 au (Cochran & Hatzes 1994). The first RV planet detection, 51 Peg b with a 4.23 d period and 0.05 au orbit was surprising (Mayor & Queloz 1995). Since both the transit and RV methods are particularly sensitive to close-in orbits (e.g. Haswell 2010), the known exoplanet population is skewed to short period, hot planets. For transit surveys the geometric selection effect for short orbital periods can be analytically corrected, and the sensitivity as a function of planet radius can be estimated with injection-recovery tests. Petigura et al. (2013) consequently showed that the fraction of stars hosting planets with radii exceeding 1 R_{\oplus} rises quite steeply with orbital period, being only $\sim 1\%$ at $P = 5$ d. Despite this property of the Galaxy's population of exoplanets, selection effects meant early discoveries were dominated by close-in planets, particularly transiting planets found by large scale ground-based transit searches

such as WASP (Pollacco et al. 2006) and the deeper survey carried out by *Kepler* (Borucki et al. 2010).

These hot planets exhibit some of the most extreme processes in planetary system evolution, including the sublimation of rocky planet surfaces due to intense irradiation (Rappaport et al. 2012). Mass loss from the closest-orbiting planets is common, and was first dramatically demonstrated in the Lyman α transits of HD 209458 b (Vidal-Madjar et al. 2003).

The inflated ultra-hot Jupiter WASP-12 b, with $P_{\text{orb}} = 1.09$ d, shows an enhanced transit depth in the near-UV compared to the optical (Fossati et al. 2010; Haswell et al. 2012), and an anomalous lack of the expected chromospheric emission cores in the Mg II h&k lines. This is consistent with absorption due to mass lost from Roche-lobe overflow (Haswell et al. 2012). Along with other hot Jupiter hosts, Fossati et al. (2013) showed that WASP-12 also shows anomalously low chromospheric emission cores in the Ca II H&K resonance lines. These planet hosts lie below the stellar chromospheric basal flux level (Schrijver 1987; Rutten et al. 1991), which is a lower limit exhibited by extremely inactive stars. The limit has been shown to be consistent with acoustic heating in the chromospheres of main sequence stars (Buchholz et al. 1998) where magnetic activity is absent. This minimum level for main sequence FGK stars lies at $\log R'_{\text{HK}} = -5.1$ (Henry et al. 1996; Wright 2004).

* E-mail: matthew.standing@esa.int

Main sequence stars with $\log R'_{\text{HK}} < -5.1$ therefore have impossibly low Ca II H&K line core emission, indicating an upper stellar atmospheric structure different from other stars, or alternatively their intrinsic line core emission has been absorbed by circumstellar material. Since the most extreme example of the sub-basal $\log R'_{\text{HK}}$ phenomenon was WASP-12 (Fossati et al. 2013), which hosts one of the hottest known giant planets, Occam’s razor strongly suggests the two phenomena are connected. Material dispersed from mass loss from close-orbiting planets can naturally give rise to circumstellar material (Haswell et al. 2012), and this material will naturally absorb starlight most strongly in the resonance line cores of abundant elements. These lines are precisely those which exhibit prominent stellar chromospheric emission. If we conclude planetary mass loss depresses a star’s apparent $\log R'_{\text{HK}}$ value, this leads to the corollary that main sequence stars exhibiting sub-basal $\log R'_{\text{HK}}$ can be identified *a priori* as the probable hosts of hot, mass-losing planets. This potentially provides an efficient short-cut to finding particularly rare and interesting exoplanets orbiting bright, nearby stars. The Dispersed Matter Planet Project aims to test and exploit this hypothesis.

Staab (2018) details a painstaking analysis of extant $\log R'_{\text{HK}}$ measurements to identify these probable hosts of hot, mass-losing planets. The steps taken to identify 39 main sequence stars with $\log R'_{\text{HK}} < -5.1$ from a supersample of 7864 stars catalogued by Pace (2013) included re-calibrating the conversions from S-index to $\log R'_{\text{HK}}$; selecting only stars with $0.4 < B-V < 1.2$ where the $\log R'_{\text{HK}}$ is well-calibrated, and using $B-V$ and M_V to identify a main sequence sample of 2716 stars. The 39 sub-basal objects became the targets of the Dispersed Matter Planet Project (DMPP, Haswell et al. 2020); they might be expected to harbour mass-losing planets in short period orbits.

RV observations of the DMPP sample has identified diverse planet systems, including DMPP-1, a compact multiplanet system (Staab et al. 2020); DMPP-2 a hot Saturn-mass planet (Haswell et al. 2020); DMPP-3Ab, a hot terrestrial, S-type circumprimary planet in a compact eccentric binary star system (Barnes et al. 2020; Stevenson et al. 2023); and DMPP-4, a naked eye star hosting either one or two sub-Neptune mass planets (Barnes et al. 2023). A summary of target observations for additional candidates was given by Haswell et al. (2020) with a comparison of the detection probabilities of the reported systems compared with a random selection of main sequence stars. Here, with further observations and a larger sample, we present new planet discoveries, a more complete, Bayesian analysis of detection sensitivities for each system and occurrence rates for the DMPP sample.

This paper comprises Section 2, outlining target selection and DMPP observational protocol; Section 3 describes our RV analysis using *kima* (Faria et al. 2018), and outlines the detection limit calculation methodology; Section 4 announces new planetary detections with associated activity analysis, and updated planet parameters, and presents occurrence rates for the survey, comparing them to occurrence rates from other RV surveys; we conclude in Section 5.

2 OBSERVATIONAL AND DATA PROTOCOLS

Observations were made on a number of observing runs, with the first observations as part of the DMPP programme made with HARPS (Pepe et al. 2002) in late 2015 and the most recent in early 2023. Motivated by the premise that the host stars harbor exoplanets in short-period orbits, individual observing runs initially intensively observed a handful of targets. By cycling through a small subsample of the DMPP targets, several observations of each chosen

star could be obtained during a single night of observing, ensuring sensitivity to short-period orbits. Signals became generally evident on the timescales > 1 d, with the result that the survey found low-mass planets on the timescales of a few days, i.e. the duration of the observing campaigns. The ESO P110 campaign in 2023, spanning 12 nights focused on long-term verification of already detected signals along with first epoch RVs for a number of previously unobserved targets. The main DMPP observations were made during ESO runs 096.C-0499(A), 097.C-0390(B), 098.C-0269(B), 099.C-0798(A) and 0100.C-0836(A), 107.22UN.001, 110.248C.001 and are supplemented for some targets by further archival HARPS observations (programme IDs detailed in the Data Availability statement). DMPP-3 was also observed in the ESPRESSO (Pepe et al. 2021) run 112.25LZ.001. DMPP-4 was observed with SOPHIE (Perruchot et al. 2008) and HARPS-N (Cosentino et al. 2012) in programmes supported by the OPTICON Trans-National Access Programme (FP7II, 2013–2016).

2.1 Observational protocol

The majority of the observations were carried out in visitor mode or delegated visitor mode at the ESO 3.6m telescope at La Silla with the High Accuracy Radial velocity Planet Searcher (HARPS). We used HARPS in High Accuracy Mode with our target spectra recorded on Fibre A and Fabry–Pérot (FP) reference spectrum on Fibre B to track the small instrument drifts relative to the nightly master reference spectrum. Before 2023, we used ThAr reference lamps, but switched to using the nightly master laser frequency comb and simultaneous Fabry–Pérot reference in P110. Service observations were also made with the Échelle SPectrograph for Rocky Exoplanets and Stable Spectroscopic Observations instrument (ESPRESSO) in singleHR mode ($R \sim 140,000$) at the ESO VLT telescopes.

2.2 Data reduction

To search for periodic signals in our data, we elected to re-reduce the RVs from the HARPS spectra, rather than using the automatically generated, cross-correlation function (CCF) derived Data Reduction Software (DRS) RVs. DRS data products derived from the CCFs, specifically the Bisector Inverse Span (BIS) and CCF full width at half maximum (FWHM) measurements, were used for the activity correlation analyses. Archival pre-fibre and DMPP post-fibre upgrade spectra were reduced respectively with DRS versions 3.5 and 3.8¹. We used the recently developed *s-BART*, which re-casts a template matching approach into a Bayesian framework to provide a more robust estimate of the RVs (Silva et al. 2022). *s-BART* creates a high S/N stellar template and removes activity-sensitive lines. It also includes an involved treatment of telluric features and removes areas near telluric lines where transmittance drops below 99% of the continuum. Uncertainties (from flux measurement) in the template are propagated for use in estimating the error in the final RV value. Deriving independent RVs for each échelle order and combining them is common practice. However, this approach can be subject to chromatic effects due to stellar activity or instrument and observing practicalities. Instead, to mitigate these factors, Silva et al. (2022) assume a single RV shift, appropriate for a dynamically induced Doppler shift, between each spectrum and the master template. The Bayesian statistical framework allows characterisation of

¹ <https://www.eso.org/sci/software/pipelines/harps/harps-pipe-recipes.html>

the RV posterior probability for any observation, and includes the possibility of marginalisation with respect to parameters of polynomials used to adjust continuum levels between spectrum and template. This ensures that the only difference is a radial velocity shift. [Silva et al. \(2022\)](#) demonstrate improvements in RV scatter over the standard DRS, HARPS-TERRA ([Anglada-Escudé & Butler 2012](#)) and SERVAL ([Zechmeister et al. 2018](#)) pipelines. [Stevenson et al. \(2025a\)](#) evaluated the use of s-BART for the multiplanet system HD 28471, finding an improvement in RV precision of over 19% compared with the DRS. We therefore use s-BART RVs for all targets in this work, including our ESPRESSO dataset, with the exception of the SOPHIE and HARPS-N observations on DMPP-4, which are detailed in [Barnes et al. \(2023\)](#).

2.3 Choice of targets & observation summary

The 39 FGK stars on the DMPP target list (see Section 1) were divided into objects observable from La Silla and objects only observable from the north, and further divided into groups which could sensibly be observed in succession over a single night. We proposed to observe such groups and then, where necessary, modified our plans to accommodate variance between the requested and awarded observing time. We typically observed a target three or four times a night during the earlier runs, but analysis began to suggest that there was much more variability on timescales of a day or longer. Consequently, we observed targets only once or occasionally twice a night in the later runs. Our empirical findings, and the lower cadence we subsequently adopted are consistent with more recent results showing RVs are affected by super-granulation noise which is correlated on a timescale of 1-2 d (e.g. [Klein et al. 2024](#)). We consider herein only DMPP targets with 10 or more RV epochs; there are 24 targets satisfying this, they are listed in Table A1-A4. Observation metrics such as number of observation on each target, SNR, observation period can be found in Table A5.

3 METHODS

Here we describe how we calculate detection limits for the DMPP survey. We analyse our RV timeseries with *kima* ([Faria et al. 2018](#)), a diffusive nested sampling algorithm which fits a sum of N_p Keplerian signals to the data. *kima* treats the number of planetary signals N_p as a free parameter, which enables Bayesian model comparison to determine the number of planetary signals present ([Standing et al. 2022](#)). During fitting, we use a Student's T distribution for the likelihood as in [Agol et al. \(2021\)](#) & [Standing et al. \(2023\)](#) which allows for any large RV outliers without strongly influencing the fit.

3.1 Prior distributions

We set up our model with priors similar to those used in [Standing et al. \(2022\)](#) with minor changes detailed below.

The β -prior distribution described in [Kipping \(2013\)](#) favours lower eccentricities but allows exploration of more eccentric orbits where the data requires ([Standing et al. 2022](#)). In *kima*, we use the more flexible Kumaraswamy distribution ([Kumaraswamy 1980](#)) as a prior, with $\alpha = 0.881$ and $\beta = 2.878$ ([Stevenson et al. 2025b](#)) as a proxy for the [Kipping \(2013\)](#) β -distribution.

We limit the upper range of our K prior following an initial run on the data. An initial run with loose priors provides us with information on the signals which could explain the data and motivates pragmatic upper limits for the K prior without leaving the parameter space too

Table 1. Prior distributions used in RV model planetary signals in *kima*. Initial (wider) priors are used for a first-fit of the data. The narrower priors are used once an initial fit has been established.

Parameter	Unit	Prior distribution	
		Initial	Narrower
N_p		$\mathcal{U}(0, 4)$	$\mathcal{U}(0, 3)$
P	days	$\mathcal{LU}(1, 100)$	$\mathcal{LU}(1, 20)$
K	m s^{-1}	$\mathcal{MLU}(0.1, 100)$	$\mathcal{MLU}(0.1, \leq 15)$
e		$\mathcal{K}(0.881, 2.878)$	
ϕ		$\mathcal{U}(0, 2\pi)$	
ω		$\mathcal{U}(0, 2\pi)$	
σ_{jit}	m s^{-1}	$\mathcal{LU}(0.001, 100)$	$\mathcal{LU}(0.001, 10 \times \text{rms})$
γ	m s^{-1}	$\mathcal{U}(\text{RV}_{\text{min}}, \text{RV}_{\text{max}})$	$\mathcal{U}(V_{\text{sys}} \pm 50)$

Notes: N_p - Number of Keplerian signals. \mathcal{U} - Uniform prior with upper and lower limit. \mathcal{LU} - Log-uniform (Jeffreys) prior with upper and lower limit. \mathcal{MLU} - Modified log-uniform prior with knee and upper limit. \mathcal{K} - Kumaraswamy prior ([Kumaraswamy 1980](#)) with two shape parameters.

large. We still allow room for variation and use a median upper limit of 15 m s^{-1} for our targets.

The lower period limit is chosen as 1-day to avoid the 1-day period alias and because shorter intervals are affected by correlated super-granulation noise; the upper period limit was chosen depending on the individual time-span of each dataset. For well sampled datasets we set the upper limit to double the timespan of the data. Whereas, for poorly sampled datasets with long times between observations we define an “effective timespan” based on the time periods covered by the sampling, e.g. if two observing runs each with a duration of 1 week are spaced 1 year apart, we take an effective timespan of 14 days, rather than 1 year. The majority of our least-sampled datasets have time-spans < 14 days, in this case we set the upper period limit to 20 days.

For each system, we use Angular Momentum Deficit (AMD) enforcement within *kima*. This option computes the AMD ([Laskar 1997, 2000](#)) for each posterior sample obtained and ensures that the solution proposed is stable, and thus a realistic solution. Samples which fail the AMD stability test are discarded, which increases the efficiency of the sampling. We used the priors in Table 1, but implemented minor changes to the limits where required, always using the same distributions. DMPP-3 is an eccentric binary; consequently, the AMD stability criterion could not be effectively applied to this system. For HD 181433, achieving an adequate fit with the AMD stability criterion also proved challenging, likely due to the presence of eccentric, Jovian-mass planets with long orbital periods. We therefore deactivated the criterion for this system as well.

kima fits for additive offsets between different instruments using a uniform prior, $\mathcal{U}(\text{min}(\text{all data}), \text{max}(\text{all data}))$. When our observations span epochs in which an instrument is known to have undergone a zero-point change (e.g. due to a fibre upgrade), we treat the pre- and post-change data as originating from separate instruments and fit independent offsets; examples include the HARPS fibre upgrade in May 2015 ([Lo Curto et al. 2015](#); [Trifonov et al. 2020](#)) and the COVID shutdown (see e.g. [Faria et al. 2022](#); [Standing et al. 2023](#); [Stevenson et al. 2023](#); [Liebing et al. 2024](#); [Stevenson et al. 2025a](#)).

We do not incorporate Gaussian Processes (GPs) in our fits because our targets all have low activity and the observation sampling is generally unsuitable for effective GP modeling.

3.2 Detection limit method

We follow the method laid out in [Standing et al. \(2022\)](#) and tested with injection recovery tests. This method is used in e.g. [Grieves et al. \(2022\)](#); [Standing et al. \(2023\)](#); [John et al. \(2023\)](#); [Balsalobre-Ruza et al. \(2025\)](#) & [Figueira et al. \(2025\)](#):

(i) For each system, we begin by running `kima` using wide-uninformative priors similar to those used in [Standing et al. \(2022\)](#) to establish the presence and parameters of any signals.

(ii) Priors for each target are then adjusted individually to sample the parameter space as efficiently as possible. For example, should there be no evidence supporting $> 2 N_p$ signals then N_p would only be sampled uniformly from $0 - 2$; should there be no evidence of signals with semi-amplitudes $> 15 \text{ m s}^{-1}$ then the upper limit on our semi-amplitude prior was lowered to $< 15 \text{ m s}^{-1}$, and so on. A second longer run would then be carried out on each dataset ensuring the most appropriate solution is obtained.

(iii) If the system has no signals which pass a Bayes Factor (BF) threshold of 150 to claim a detection ([Jeffreys 1961](#); [Standing et al. 2022](#)), then we proceed to the next step. However, if ≥ 1 planetary signal is detected, then the posterior sample with the highest likelihood is subtracted from the data, and `kima` is run on the subtracted dataset to ensure no signals remain.

(iv) `kima` is then run on the data set (or the signal-subtracted data set) with N_p fixed to a value of 1. This step yields the posterior samples which can be used to calculate our detection limits as detailed in [Standing et al. \(2022\)](#). We run `kima` until a minimum of 200,000 posterior samples have been obtained on each system to ensure robust detection limits can be calculated².

(v) Once the posterior samples are obtained, we calculate the detection limits by binning the samples in log-period space, P_p , and obtaining the (upper) 99% confidence levels of the semi-amplitudes, K_p , as in [Standing et al. \(2022\)](#). The uncertainty (E) on the detection limits are calculated as in [Standing et al. \(2023\)](#) using the equation $E = \frac{1.97}{\sqrt{N}}$.³

An example detection limit calculated following the above steps can be seen in [Figure 1](#) for HD 118006 / DMPP-7. We perform the above steps for our sample of 24 DMPP targets (see [Table A1](#)). Detection limit uncertainties, calculated as described above, are plotted for each detection limit shown here and in [Appendix B](#). In some cases, the uncertainties are too small to be visible. For DMPP-1 and the previously unreported system HD 67200 / DMPP-6, which have more extensive datasets, we investigate the solutions further, including the application of GPs in [Barnes et al. \(2025\)](#). For the purposes of this study, we assume all RV signals are of dynamically induced origin, resulting from orbiting exoplanet candidates.

3.3 Survey completeness

With detection limits calculated for each of the systems in the DMPP sample, it then becomes possible to calculate the survey's completeness. We follow the approach of [Martin et al. \(2019\)](#), [Cumming et al. \(2008\)](#), and [Mayor et al. \(2011\)](#), combining the 99% detection limits across all individual targets and averaging them within mass-period

² On average we have $\approx 400,000$ samples for each of our systems.

³ We note that the incorrect scaling value was stated in [Standing et al. \(2023\)](#) and should be $a = 1.97 \pm 0.12$. This does not affect the results of [Standing et al. \(2023\)](#), only the uncertainty plotted in the detection limit in [Figure 4](#) of the paper.

bins. This completeness is defined as $C(P_b, m_b \sin i_b)$, i.e., the minimum mass our survey is sensitive to at a given period. It is illustrated by the red shaded regions in [Figure 2](#), where white indicates 0% completeness (no sensitivity in any system), and dark red indicates 100% completeness—regions of parameter space to which we are sensitive in all 24 systems. The 100% completeness region does not extend past 20 days in orbital period as some of our datasets have timespans < 14 days as discussed in [Section 3.1](#).

3.4 Occurrence rates

In regions of the mass-period space where no planetary signals are formally detected we are only able to place upper limits on planet occurrence rates. We follow [He et al. \(2017\)](#); the upper limits on planet abundance is calculated ([Martin et al. 2019](#)) using:

$$\mathcal{N}_p = \frac{1 - (1 - \kappa)^{1/n_{\text{stars}}}}{C(P_b, m_b \sin i_b)} \quad (1)$$

Here, \mathcal{N}_p is the upper limit on the number of planets, κ is the confidence interval (i.e. for 2σ , 95% interval $\kappa = 0.95$); $n_{\text{stars}} = 24$ herein and $C(P_b, m_b \sin i_b)$ is the mean completeness within the region of parameter space in question.

In regions where there are planetary signals detected the planetary abundance is calculated as in [Mayor et al. \(2011\)](#) using ([Martin et al. 2019](#); [Bennett et al. 2021](#)):

$$\mathcal{N}_p = \frac{1}{n_{\text{stars}}} \sum_{i=1}^{n_{\text{det}}} \frac{1}{C(P_b, m_b \sin i_b)} \quad (2)$$

where n_{det} is the number of planet detections in the region.

The uncertainties on the occurrence rates are computed using the Clopper-Pearson confidence interval ([Clopper & Pearson 1934](#)). This method allows retrieval of conservative and realistic uncertainties even for a low number of observed successes, solving the issues arising in the standard Poisson error $\sigma = 2\mathcal{N}_p/\sqrt{n_{\text{det}}}$ (e.g. [Martin et al. 2019](#)). In practice, we compute the Clopper-Pearson 1σ confidence interval for the observed occurrence rate in each $\{P_b, m_b \sin i_b\}$ bin, and then correct for completeness by dividing both the upper and lower values by the corresponding $C(P_b, m_b \sin i_b)$.

4 RESULTS AND DISCUSSION

4.1 Detection limit results

Individual detection limits for each target in our sample can be found in [Appendix B](#). Detection limits for the survey reveal that our most sensitively probed systems are DMPP-1, DMPP-3, DMPP-4, HD 39194, HD 67200, and HD 181433. We are sensitive to Earth mass planets orbiting DMPP-3, HD39194, HD67200, and HD181433 at periods < 5 days (see [Figures B3, B7, B9, and B19](#)). In all six of the systems listed above, our data allow us to detect planets with masses smaller than $2 M_{\oplus}$ on orbital periods ranging from less than 5 days (DMPP-1 and DMPP-4) to less than 50 days (HD 181433). This is attributable to a combination of sufficient well-sampled observations (between 71 and 288 data points, including 20 ESPRESSO spectra for DMPP-3) and the targets' brightnesses (V magnitudes as high as 5.7).

In contrast, in our least-sensitive system, HD 58489 (with 40 data points and a V magnitude of 9.74), we are still sensitive to sub-Neptune mass planets out to ≈ 5 days, and sub-Saturn mass planets out to ≈ 1000 days ([Figure B8](#)).

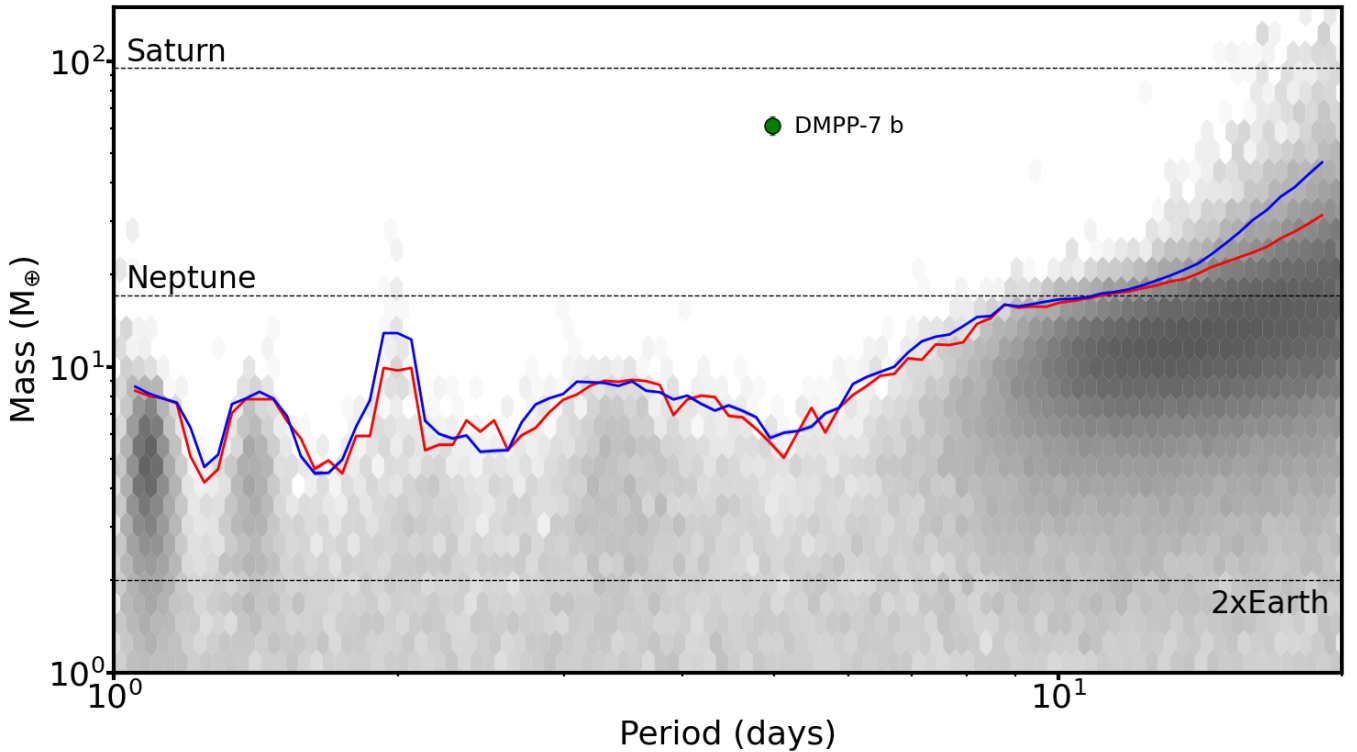


Figure 1. Detection limit plot for HD118006 / DMPP-7. The grey hexbin plot denotes the density of posterior samples obtained from *kima* runs on our HD118006 / DMPP-7 dataset, the darker the region the more samples are present. The blue line is the 99% upper detection limit, with uncertainties denoted by the blue shaded region. The red line is the 99% upper limit calculated on posterior samples with $e < 0.1$, with associated uncertainty denoted by the red shaded region. Shaded uncertainties for the detection limits are present but small. The green point represents the detected planetary signal of HD118006 / DMPP-7 b.

4.2 Detection limits in the presence of planetary signals

As stated in Section 3.2, if a system hosts a candidate signal that passes our detection threshold, a Bayes Factor (BF) of 150, this signal is subtracted prior to calculating the detection limit. The subtracted signals, corresponding to the posterior samples with the highest likelihood, are listed in Table C1.

If, on the other hand, a candidate signal does not exceed the detection threshold, it is not removed before computing the detection limit. In such cases, if there remains significant evidence for the signal, the majority of posterior samples obtained during the detection limit run (with $N_p = 1$) tend to cluster around the orbital period of the candidate.

For these systems, we investigated the effect of forcing $N_p = 2$ (to account for both the candidate and additional signals), rather than relying solely on a single-planet model. The results of this test are shown for the target BD+03580 in Figure 3. The green detection limit is derived from posterior samples obtained with $N_p = 2$, while the blue curve corresponds to the detection limit from a higher number of posterior samples with $N_p = 1$. We find that forcing $N_p = 2$ results in a lower detection limit than simply increasing the number of samples under the single-planet assumption.

From this analysis, we conclude that when calculating detection limits in the presence of strong candidate signals that are not subtracted (as in step (iii) of Section 3.2), best practice is to obtain more than 200,000 posterior samples to adequately explore the parameter space. If this is not feasible, and the returned samples still cluster at the orbital period of the candidate, this provides strong evidence in favour of the signal. In such cases, it becomes reasonable to force $N_p = 2$ to account for both the candidate and any additional signals.

This situation applies to only one target in our sample: HD 67200 / DMPP-6 (see Section 4.5).

4.3 Targets with previously published solutions

In this section we present the orbital parameters obtained from our fits to the data, updating planetary parameters that have been previously published in our target systems. We obtain parameters from our posterior samples as in Standing et al. (2022, 2023), by clustering the samples in period, semi-amplitude and eccentricity using *fast_HDBSCAN*⁴. The clusters are then plotted using the *corner* package (Foreman-Mackey 2016), the 50th percentile provides the orbital parameters, and the cluster’s 14th and 84th percentile provide the 1σ uncertainty. Orbital parameters for these systems can be found in Table 2, phase plots for each of the signals mentioned here in Appendix D, and corner plots for the same signals here can be found in Appendix E.

DMPP-1: DMPP-1 was previously proposed to host a system of four planets (Staab et al. 2020). However, simultaneous fitting of multiple signals with *kima* yields results that differ from the periodogram-based recursive search employed by Staab et al. (2020). The new solution with the additional observations taken in 2023 has a less constrained eccentricity prior (i.e. beta distribution compared vs the previously adopted half-Gaussian width of 0.05) and uses the

⁴ *fast_HDBSCAN* is an updated version of the original algorithm by McInnes et al. (2017) to allow running on multiple cores https://github.com/TutteInstitute/fast_hdbscan

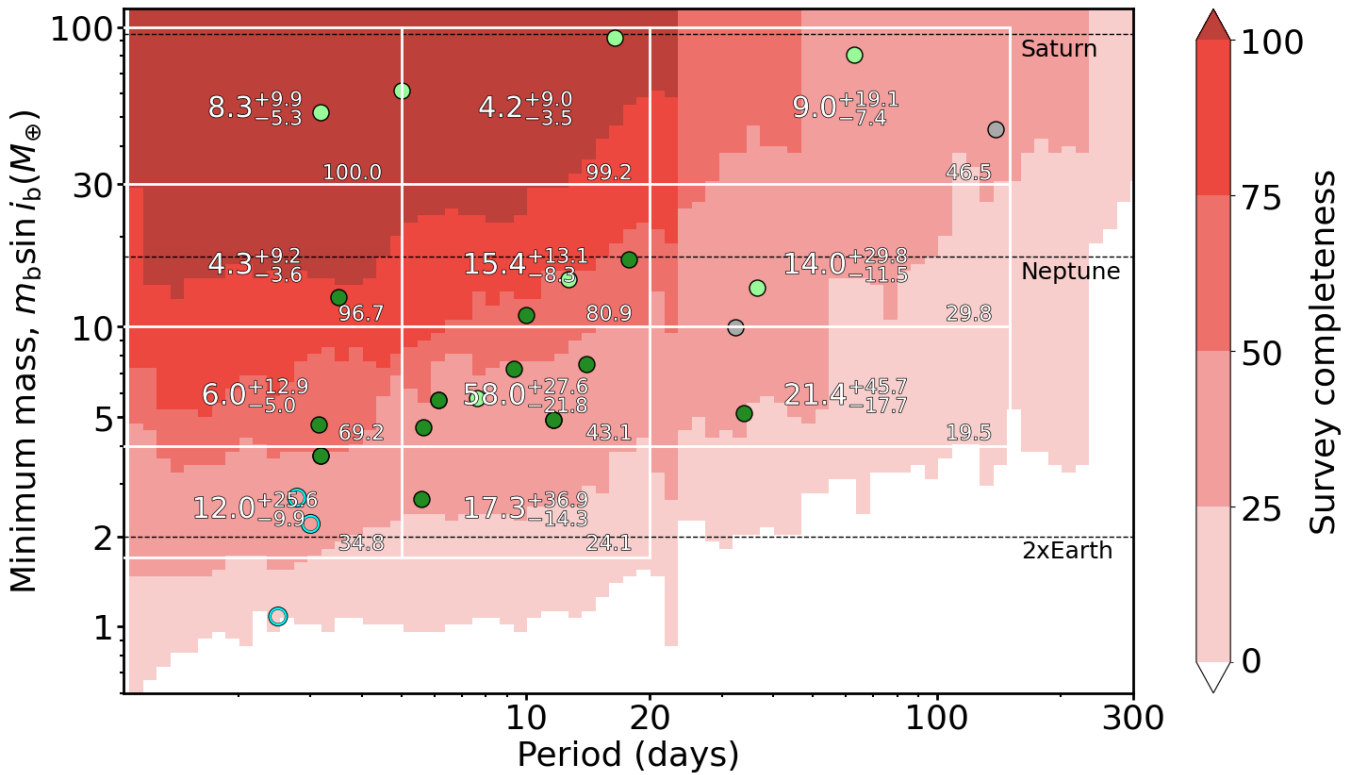


Figure 2. Completeness and planet abundance plot for the DMPP radial velocity survey of 24 targets with sub-basal activity, as a function of minimum mass and orbital period. The red contours indicate the completeness of the survey from 0% (white) to 100% (dark red) as in Figure 10 in [Martin et al. \(2019\)](#). The dark green circles show previously published planet signals present in our data, while the light green show signals found to pass our detection threshold in this work. Cyan open circles are the three candidate signals we identified with moderate statistical evidence, while the grey circles represent signals which we suspect arise from activity. The white lines delineate 11 boxes enclosing regions of parameter space within which we are able to constrain our planetary abundance. Box limits were chosen to be roughly equal in log space for short periods within our completeness, with mass limits on integer masses. The number in the centre of each box is a percentage indicating the planet abundance with its 1σ uncertainty, or the 2σ (95%) upper limit on abundance where no planet detection was made. The white values in the lower right of each box is its mean completeness as a percentage.

AMD constraint to reject non-stable orbits. This combination of factors leads to a less prior-driven posterior distribution of eccentricities. The Bayesian interpretation thus favours a three-planet solution with slightly more eccentric, but stable, orbits. The BF exceeds 15,000. Our new maximum posterior solution includes three significant signals with orbital periods of 3.14, 9.79, and 17.83 days. These findings are consistent with the default and alternative periodicities reported in [Staab et al. \(2020\)](#) and are investigated further in a forthcoming publication.

DMPP-2: DMPP-2 was previously analysed by [Haswell et al. \(2020\)](#), who identified a single planet with an orbital period of 5.203 days. Using *kima*, our analysis favors the presence of three planetary signals, with BF of 390 supporting this model over simpler alternatives. The posterior sample with the highest likelihood reveals orbital periods of 3.168, 5.203, and 16.491 days. The second of these is the period reported by [Haswell et al. \(2020\)](#). Figure 4 shows the three signals detected in our analysis. We present two additional planets: DMPP-2 c is a $51.8 M_{\oplus}$ planet on a 3.168 day orbit, and DMPP-2 d is a $91.8 M_{\oplus}$ planet on a 16.5 d orbit. This solution yields an increase in mass for the previously detected planet DMPP-2 b at $171.5 M_{\oplus}$ compared to the $138.9 M_{\oplus}$ originally reported in [Haswell et al. \(2020\)](#). Figure 4 shows the three signals corresponding to DMPP-2 b, c, and d from the posterior sample with the highest likelihood for our DMPP-2 analysis. A full activity analysis on this target was carried out in [Haswell et al. \(2020\)](#) and no correlations or

significant periodogram power were identified at the above periods. DMPP-2 was observed in TESS Sector 30, but is too close to the edge of the field to enable photometric extraction from the full frame images. This system is discussed in greater detail in [Barnes et al. \(2025\)](#).

DMPP-3: DMPP-3AB is an eccentric ($e \sim 0.6$) binary system with an orbital period of 507 days and a semi-major axis of 1.2 au ([Stevenson et al. 2023](#)). A circumpriary (S-type) planet, DMPP-3Ab, was previously reported in the system with an orbital period of 6.67 days ([Barnes et al. 2020](#); [Stevenson et al. 2023](#)).

Since then, new radial velocity data from ESPRESSO ([Pepe et al. 2021](#)) have become available. Including this new data, and modelling without constraining the planet’s eccentricity, we find revised orbital parameters for DMPP-3Ab which differ from those reported by [Stevenson et al. \(2023\)](#). Specifically, we now find an orbital period of approximately 5.6 days and an eccentricity of $e \approx 0.42$, although the planet’s minimum mass remains consistent at $2.67 M_{\oplus}$. The updated parameters are summarised in Table 2.

We note that the 5.6 day signal is not well-supported by the ESPRESSO data alone (see the top plot in Figure D2), the signal’s power appears to originate primarily from our HARPS observations of the system. When allowing for an additional planetary signal in the model, we continue to observe power near a period of ~ 2.26 days with a mass of $\sim 1.08 M_{\oplus}$, as previously discussed in [Stevenson et al.](#)

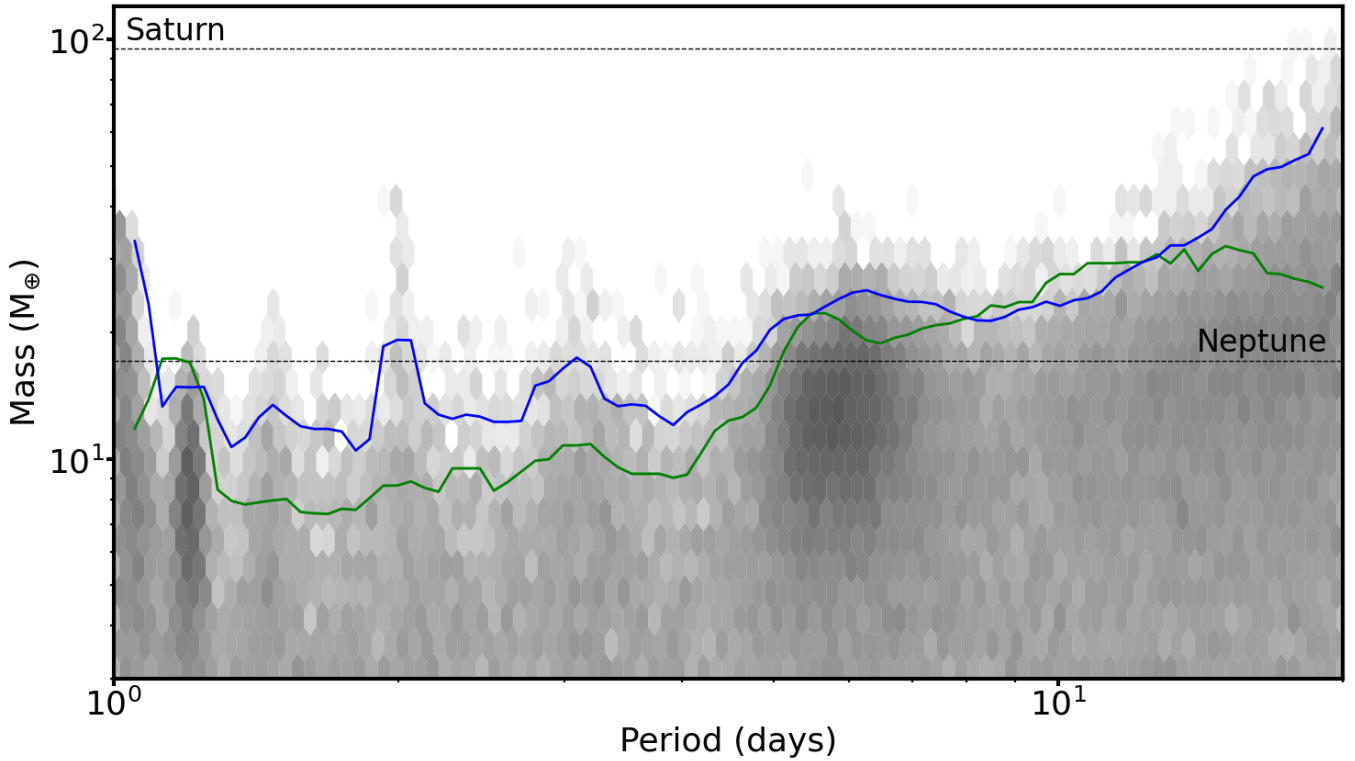


Figure 3. Detection limit plot for BD+03580. The grey hexbin plot denotes the density of 222,000 posterior samples obtained from *kima* runs. The blue line is the 99% upper detection limit, with uncertainties denoted by the blue shaded region. The green line is the same 99% upper limit calculated on posterior samples obtained from separate runs where $N_p = 2$, with associated uncertainty denoted by the green shaded region. Shaded uncertainties for the detection limits are present but small

(2023). However, additional observations are required to confirm the presence of this potential second planet.

DMPP-4: Barnes et al. (2023) identified stellar activity signals which they modelled using a Gaussian Process (GP), along with a candidate Neptune-mass planet, DMPP-4b. Here, for the purposes of calculating the detection limits, we subtracted the preferred solution from Barnes et al. (2023), consisting of the 3.498 day planetary signal and the GP model fit to both the radial velocity and bisector span time series. Consequently, in the absence of additional data, we do not update the planetary parameters for this system.

HD 28471 (DMPP-5): Stevenson et al. (2025a) identified three planetary signals in this system, HD 28471 (DMPP-5) b, c and d. Here, for the purposes of calculating the detection limits, we subtracted a preferred solution corresponding to the 3.16, 6.12, and 11.68 day planetary signals from Stevenson et al. (2025a). Consequently, in the absence of additional data, we also do not update the planetary parameters for this system.

HD 181433: The planetary system HD 181433 was initially reported by Bouchy et al. (2009) to host three planets with orbital periods of 9.37, 962, and 2172 days. These orbital solutions were subsequently refined by Campanella et al. (2013) using dynamical simulations, yielding revised periods of 9.37, 975, and 2468 days. With the inclusion of additional data, Horner et al. (2019) further updated the system architecture, increasing the orbital separation of planet d and deriving best-fit periods of 9.37, 1014.5, and 7012 days.

For HD 181433, we have obtained ten additional HARPS spectra over a timespan of ten days, with the aim of detecting any planets interior to HD 181433 b. However, incorporating this new dataset into our analysis reveals no evidence for additional planets in the system.

We include the Horner et al. (2019) solution as known objects⁵ in our *kima* model, and recover parameters consistent with their reported uncertainties.

HD 39194: The HD 39194 multiplanet system was reported by Unger et al. (2021) to host three super-Earth planets. We obtained 12 additional HARPS spectra over a 9-day timespan in an effort to search for planets interior to the 5.6 day period HD 39194 b. Our analysis reveals no evidence for additional planets beyond those identified by Unger et al. (2021), although we do detect the 1-day alias of the 14 and 5.6-day signals previously reported. Excluding these aliases, our preferred *kima* solution is consistent with that of Unger et al. (2021) (see Table 2). However, we note that the stellar mass used in Unger et al. (2021) of $0.67 M_{\odot}$ is very low for a K0V type star, and instead we use the mass derived from *Gaia* FLAME of 0.86 ± 0.04 (Gaia Collaboration 2020).

HD 89839: is known to host a giant planet with an orbital period of 3440 d, as reported by Xiao et al. (2023). We include this known signal in our *kima* analysis by treating it as a known object, using the parameters provided in their study. However, since the orbital period lies well beyond the range of interest in our current search, we do not subtract the signal from the data. To probe for additional short-period companions, we contribute 22 new HARPS spectra spanning ten days. Unfortunately, with the current dataset, we find no evidence for additional short-period planets in the system. Our recovered parameters for HD 89839 b can be found in Table 2.

⁵ Setting a known object in *kima* allows tight individual priors to be set on a specific signal, and allows the samples to explore the known signal along with any additional signals that may be present in the data.

Table 2. Orbital parameter comparison table for previously published planetary signals. Upper rows for each planet are previously published solutions, lower rows are from this work. For eccentricities with posterior distributions consistent with zero we provide the 1-sigma upper limit of the distribution.

System name	Period [days]	K [m s ⁻¹]	<i>e</i>	ω [rad]	$m_p \sin i$ [M _⊕]	T ₀ [BJD-2400000]	a [AU]
DMPP-1 b ¹	18.57 ^{+0.01} _{-0.01}	5.162 ^{+0.19} _{-0.31}	< 0.083	-	24.27 ^{+1.16} _{-1.59}	57375.58981035	0.1462 ^{+0.0012} _{-0.0012}
	17.812 ^{+0.025} _{-0.019}	3.63 ^{+0.60} _{-0.54}	< 0.2	3.21 ^{+2.42} _{-2.31}	16.80 ^{+2.5} _{-2.5}	58679.85 ^{+7.38} _{-5.23}	0.1423 ^{+0.0013} _{-0.0013}
DMPP-1 c	6.584 ^{+0.003} _{-0.002} [10.57]	2.884 ^{+0.16} _{-0.47}	< 0.057	-	9.6 ^{+0.53} _{-1.58}	-	0.0733 ^{+0.0006} _{-0.0007}
	10.03 ^{+0.53} _{-0.24}	2.89 ^{+0.16} _{-0.15}	< 0.22	2.11 ^{+1.53} _{-1.52}	10.94 ^{+0.61} _{-0.59}	58684.72 ^{+3.87} _{-3.29}	0.0973 ^{+0.0031} _{-0.0016}
DMPP-1 d	2.882 ^{+0.001} _{-0.001} [3.146]	1.326 ^{+0.149} _{-0.130}	< 0.07	-	3.35 ^{+0.38} _{-0.34}	-	0.0422 ^{+0.0004} _{-0.0003}
	3.1417 ^{+0.0020} _{-0.0248}	1.88 ^{+0.33} _{-0.30}	< 0.36	4.06 ^{+0.60} _{-0.65}	4.72 ^{+0.81} _{-0.73}	58688.54 ^{+0.84} _{-1.12}	0.04467 ^{+0.00045} _{-0.00040}
DMPP-1 e [*]	5.516 ^{+0.002} _{-0.004}	1.316 ^{+0.358} _{-0.206}	< 0.07	-	4.13 ^{+0.66} _{-1.14}	-	0.0651 ^{+0.0005} _{-0.0005}
	N/A	N/A	N/A	N/A	N/A	N/A	N/A
DMPP-2 b ²	5.2072 ^{+0.0002} _{-0.0055}	40.26 ^{+2.69} _{-5.40}	< 0.082	-	138.89 ^{+9.53} _{-18.75}	53254.84461	0.0664 ^{+0.0005} _{-0.0005}
	5.2030 ^{+0.0012} _{-0.0012}	49.60 ^{+3.12} _{-2.19}	< 0.06	2.41 ^{+1.68} _{-1.23}	171.48 ^{+10.99} _{-8.34}	57521.43 ^{+1.47} _{-0.10}	0.06638 ± 0.0004
DMPP-2 c [†]	N/A	N/A	N/A	N/A	N/A	N/A	N/A
	3.168 ^{+0.355} _{-0.002}	17.99 ^{+1.76} _{-2.02}	< 0.28	2.00 ^{+0.62} _{-0.48}	51.79 ^{+5.43} _{-5.49}	57524.30 ^{+0.22} _{-0.75}	0.04789 ^{+0.00327} _{-0.00049}
DMPP-2 d	N/A	N/A	N/A	N/A	N/A	N/A	N/A
	16.491 ^{+0.067} _{-0.053}	18.21 ^{+1.32} _{-1.38}	< 0.1	4.66 ^{+1.01} _{-3.61}	91.79 ^{+6.11} _{-7.32}	57516.66 ^{+3.69} _{-4.02}	0.1432 ^{+0.0012} _{-0.0013}
DMPP-3A b ³	6.67 ^{+0.03} _{-0.01}	0.82 ^{+0.20} _{-0.07}	0.174 ^{+0.032} _{-0.084}	0.9189 ^{+0.0017} _{-0.0080}	2.22 ^{+0.5} _{-0.28}	-	0.0670 ^{+0.0003} _{-0.0002}
	5.590 ^{+0.169} _{-0.002}	1.17 ± 0.27	0.42 ± 0.17	1.96 ^{+0.48} _{-0.52}	2.67 ^{+0.50} _{-0.56}	57432.1 ^{+2.8} _{-2.1}	0.05958 ^{+0.00119} _{-0.00043}
DMPP-3B	506.89 ± 0.01	2657.31 ^{+0.33} _{-0.02}	2.773 ± 0.001	0.596 ± 0.001	82.52 ± 0.53M _J	-	1.139 ± 0.004
	506.93 ^{+0.01} _{-0.05}	2671.1 ^{+3.5} _{-9.8}	0.59811 ^{+0.00036} _{-0.00078}	2.77356 ^{+0.00113} _{-0.00041}	78.25 ± 0.56M _J	56936.288 ^{+0.254} _{-0.027}	1.2336 ^{+0.0039} _{-0.0040}
DMPP-3+	809.38 ^{+0.20} _{-0.34}	3.52 ^{+0.20} _{-0.34}	0.0(Fixed)	5.0027 ^{+0.0049} _{-0.0019}	0.156 ± 0.007M _J	-	1.641 ^{+0.006} _{-0.005}
	809.29 ^{+0.93} _{-1.01}	2.8 ^{+0.60} _{-0.28}	0.0(Fixed)	3.36 ^{+0.80} _{-2.46}	0.124 ^{+0.024} _{-0.013} M _J	57090.0 ^{+212.3} _{-247.8}	1.6409 ^{+0.0056} _{-0.0055}
DMPP-4 b ⁴	3.4982 ^{+0.0015} _{-0.0027}	4.58 ^{+0.59} _{-0.67}	< 0.063	3.6 ^{+1.8} _{-2.5}	12.6 ^{+1.6} _{-1.8}	57139.8 ^{+1.3} _{-1.3}	0.04854 ^{+0.00033} _{-0.00054}
HD 28471 / DMPP-5 b ⁵	3.1649 ^{+0.0002} _{-0.0003}	1.679 ^{+0.180} _{-0.197}	0.195 ^{+0.061} _{-0.073}	2.66 ^{+0.40} _{-0.45}	3.72 ^{+0.40} _{-0.43}	52945.806	0.042 ^{+0.001} _{-0.001}
HD 28471 / DMPP-5 c	6.1245 ^{+0.0856} _{-0.0009}	2.045 ^{+0.190} _{-0.257}	0.088 ^{+0.058} _{-0.054}	1.32 ^{+3.88} _{-0.78}	5.72 ^{+0.57} _{-0.72}	-	0.065 ^{+0.001} _{-0.001}
HD 28471 / DMPP-5 d	11.6810 ^{+0.0042} _{-0.0055}	1.411 ^{+0.233} _{-0.218}	0.093 ^{+0.064} _{-0.058}	1.67 ^{+3.56} _{-1.08}	4.91 ^{+0.82} _{-0.77}	-	0.100 ^{+0.002} _{-0.002}
HD 181433 b ⁶	9.3745 ± 0.0002	2.7 ± 0.1	0.336 ± 0.014	3.672 ± 0.044	7.09 ± 0.10	52939.16 ± 0.06	0.0801 ± 0.0001
	9.37450 ^{+0.00025} _{-0.00038}	2.646 ^{+0.089} _{-0.124}	0.396 ^{+0.015} _{-0.024}	3.523 ^{+0.073} _{-0.138}	7.22 ^{+0.44} _{-0.45}	56470.15 ^{+0.10} _{-0.19}	0.0828 ^{+0.0019} _{-0.0020}
HD 181433 c	1014.5 ± 0.6	16.55 ± 0.07	0.235 ± 0.003	0.150 ± 0.012	214.29 ± 0.95	52184.3 ± 1.9	1.819 ± 0.001
	1018.50 ^{+1.47} _{-0.78}	17.05 ^{+0.19} _{-0.18}	0.2402 ^{+0.0093} _{-0.0080}	0.177 ^{+0.013} _{-0.026}	235.50 ^{+10.80} _{-11.13}	55711.3 ^{+3.4} _{-7.1}	1.885 ^{+0.042} _{-0.044}
HD 181433 d	7012 ± 276	8.7 ± 0.1	0.469 ± 0.013	4.212 ± 0.042	194.63 ± 1.27	46915 ± 239	6.60 ± 0.22
	6896.1 ^{+102.7} _{123.7}	8.58 ^{+0.15} _{-0.13}	0.444 ^{+0.020} _{-0.018}	4.365 ^{+0.059} _{-0.030}	206.91 ^{+10.49} _{-10.49}	50647.2 ^{+155.4} _{-87.9}	6.74 ^{+0.18} _{-0.18}
HD 39194 b ⁷	5.6368 ± 0.0004	1.86 ± 0.13	< 0.105; < 0.207	-	4.0 ± 0.3	55503.8 ± 1.4	0.056 ± 0.001
	5.63692 ± 0.00032	1.84 ± 0.11	< 0.101	3.1 ± 1.7	4.62 ± 0.32	52942.3 ± 2.5	0.05895 ± 0.00092
HD 39194 c	14.030 ± 0.003	2.19 ± 0.14	< 0.078; < 0.154	-	6.3 ± 0.5	55499 ± 3	0.103 ± 0.002
	14.0309 ± 0.0022	2.19 ± 0.13	< 0.078	2.2 ^{+2.8} _{-1.4}	7.49 ± 0.50	52937.9 ± 5.8	0.1083 ± 0.0017
HD 39194 d	33.91 ± 0.03	1.04 ± 0.14	< 0.174; < 0.333	-	4.0 ± 0.6	55516 ± 7	0.185 ± 0.0033
	33.874 ± 0.024	1.13 ± 0.13	< 0.159	4.2 ^{+1.4} _{-3.3}	5.16 ± 0.59	52932.3 ^{+8.8} _{-16.8}	0.1949 ± 0.0031
HD 89839 b ⁸	3441 ± 18	-	0.187 ± 0.013	2.818 ± 0.061	1211.3 ± 24.5	56682.0 ± 35.0	4.761 ± 0.042
	3391.2 ^{+26.1} _{-24.6}	45.65 ^{+0.63} _{-0.60}	0.185 ± 0.014	2.757 ± 0.081	1196.9 ± 26.1	49842.2 ± 60.2	4.713 ± 0.045

Notes: 1 - [Staab et al. \(2020\)](#), 2 - [Haswell et al. \(2020\)](#), 3 - [Stevenson et al. \(2023\)](#), 4 - [Barnes et al. \(2023\)](#) (parameters not updated here),

5 - [Stevenson et al. \(2025a\)](#) (parameters not updated here), 6 - [Horner et al. \(2019\)](#), 7 - [Unger et al. \(2021\)](#), 8 - [Xiao et al. \(2023\)](#)

* We only find evidence of three signals present in our DMPP-1 data.

† In [Haswell et al. \(2020\)](#) only a single planetary signal was detected in the DMPP-2 data.

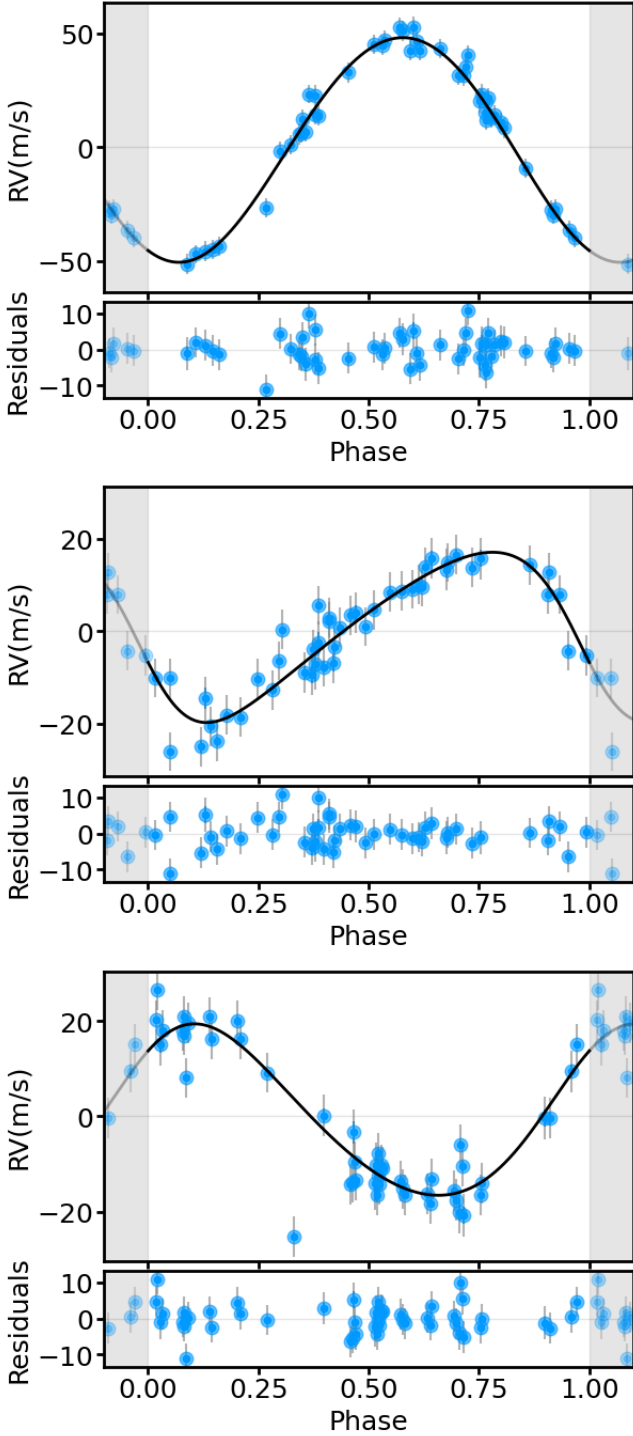


Figure 4. Phased Keplerian RV models of DMPP-2 b (top), DMPP-2 c (middle), and DMPP-2 d (bottom) with HARPS data post-fibre upgrade (blue) and its residuals after removing the planetary signals. The additional RV jitter term has been added to the plotted uncertainties and is shown by the grey error bars. No random samples are shown for these signals as their eccentricity is unconstrained and consistent with 0. The shaded regions display the repeating signal.

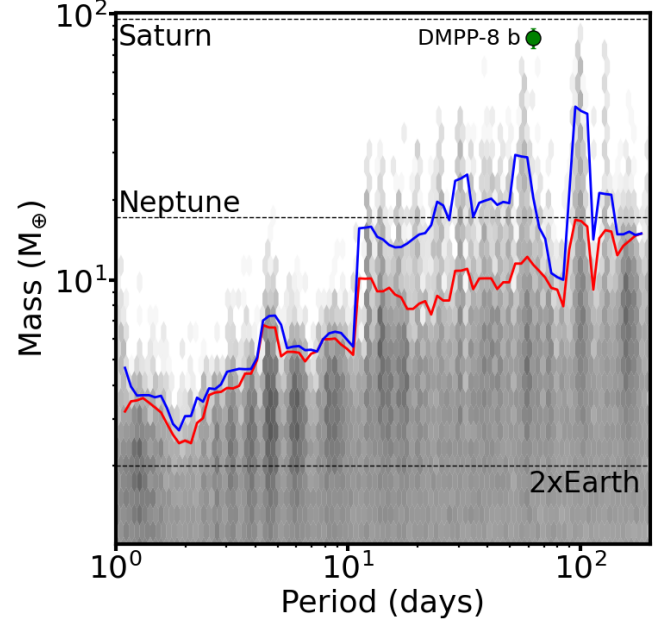


Figure 5. Detection limit plot as in Figure 1 for target HD191122 / DMPP-8 demonstrating the difference between the circular (red) detection limit and the standard (blue) detection limit.

4.4 The Dangers of Assuming Circular Orbits

As shown in [Standing et al. \(2022\)](#), fixing $e_p = 0$ when calculating detection limits can lead to overly optimistic results, by as much as 40%. In this study, we extend their analysis by calculating detection limits for 24 target systems, an eightfold increase in sample size. For each system, we plot the standard 3σ detection limit in blue and the corresponding 3σ limit calculated using only posterior samples with $e_p < 0.1$ in red. These plots are available in Appendix B.

Across all targets, the circular (red) detection limits are consistently lower than the standard (blue) limits, with a median reduction of 7.99% and a maximum difference of 38.7%, equivalent to $5.1 M_{\oplus}$ for HD191122 (Figure 5).

Our findings reinforce the conclusion of [Standing et al. \(2022\)](#) that using a diffusive nested sampler where no simplifying assumptions are necessary yields more robust detection limits. Moreover, enforcing circular orbits can lead to an apparent oversensitivity of up to 8%, potentially biasing both detection limits and the resulting occurrence rates.

4.5 Planet discoveries

We now present new planetary signals discovered in our analysis with $\text{BF} > 150$. The new planetary parameters are listed in Table 3, while Table C1 lists the maximum likelihood parameters of all signals used to derive detection limits, i.e. it also includes signals discussed in Section 4.3.

Although the DMPP sample comprises low activity targets, we cannot rule out the presence of intrinsic stellar activity above the $\log R'_{\text{HK}} = -5.1$ basal cutoff. Thus, while we have modeled all signals as Keplerians, we also examined common stellar activity metrics for targets with sufficient RV measurements or with candidate planet signals. For each target spectrum, the Ca II H&K indices along with the bisector inverse span (BIS) and full width at half maximum (FWHM), derived from the HARPS DRS cross-correlation functions

(CCFs), were tested for periodicities and correlations with the derived s-BART RVs. The mean BIS and FWHM variation for each target can be found in Table A5. In addition, we tested the third line moment, M_3 of the CCFs (Barnes et al. 2024), which also returns a similar, but potentially more sensitive measure than the BIS of photospheric activity components. We also examined the *TESS* photometry for targets with planet signals. The *TESS* SPOC Simple Aperture Photometry (SAP) fluxes contain very large systematics with discontinuities and large amplitude sector-length trends, meaning they are not suitable for stellar periodicity searches for low activity stars. By contrast, the Pre-Search Data Conditioned Simple Aperture Photometry (PDC-SAP) fluxes only show low level variability for low activity stars, since they are optimised for transit searches⁶. The PDCSAP fluxes often show peak period power at around $\lesssim 10$ d, using single and multiple *TESS* sectors; however, the corresponding signal amplitudes of 10 – 100 ppm are very low and likely arise from remaining systematics after pre-conditioning for transit searches. For comparison, we note that Clayton et al. (2024) have employed *TESS* full frame images (FFIs) and machine learning to obtain rotation periods for over 70000 stars in the *TESS* southern continuous viewing zone. They are sensitive to periods up to 35 d for GK stars and 80 d for M stars and generally recover periodicities for targets with $300 \lesssim S_{\text{ph}} \lesssim 10000$ ppm (where S_{ph} is a measure of variability amplitude from a mean of standard deviations of lightcurve segments of length $5 \times P_{\text{rot}}$). We used UNPOPULAR (Hattori et al. 2022) to detrend FFIs for individual sectors and check for stellar periodicities. Below, we give a brief summary for those targets where we find new candidate planets.

HD 2134: Our data for HD 2134 provides strong evidence, $\text{BF} > 25,000$, for a single signal with a period of 32.3 d and a minimum mass of $9.93 M_{\oplus}$.

Two sets of observations were acquired for this target. However, the most recent set was affected by significant issues, leaving only two usable data points. Accounting for an additional RV offset and white-noise jitter parameter renders these two points uninformative, as they contribute negligible statistical weight to the model fit. We therefore exclude these most recent observations from our final analysis. We note, however, that their inclusion does not significantly alter the recovered 32-day signal.

The system also shows moderate evidence for a second planetary signal, with BF of 73.5 in favour of a two-planet model. The highest-likelihood two-planet solution includes a 2.78 d, $2.69 M_{\oplus}$ planet on a near-circular orbit ($e = 0.15$), and a more eccentric ($e = 0.66$), 21.18 d, $6.8 M_{\oplus}$ signal. However, given that our current dataset robustly supports only a single-signal interpretation, we subtract this single-planet model from the data when computing detection limits.

With the exception of FWHM, the activity indices show only weak indications of a correlation, with Pearson’s $|r| \lesssim 0.24$. Although the FWHM correlation is weak, $r = 0.31 \pm 0.10$, the probability of no correlation is excluded via the p-statistic, $p = 0.004$. With $v \sin i = 2.61 \pm 0.55 \text{ km s}^{-1}$ and $R_* = 1.16 \pm 0.01 R_{\odot}$ (values from SPECIES; Soto & Jenkins 2018), and assuming randomly distributed stellar axial inclinations, i , (i.e. observed probability density $P(i) \propto \sin i$) we predict a most probable $P_{\text{rot}} = 18.6$ d. By fixing the inclinations to the observed mean of $\int_0^{\frac{\pi}{2}} i \sin(i) di = 1 \text{ rad} = 57.3^\circ$ and $i = 90^\circ$, we find respectively $P_{\text{rot}} = 17.5$ d and 20.8 d. A periodogram of FWHM shows marginal evidence for periodicities at 24.5, 21.1 and 31.6 d ($\Delta \log L = 15.5, 13.5$ and 13.4), which are distinct from window function peaks. HD 2134 was observed in three sets of consecutive

TESS sectors: Sectors 27 and 28, Sectors 67 and 68 and Sectors 94 and 95. We performed periodogram analysis of the photometry using likelihood periodogram analysis (Anglada-Escudé et al. 2013, 2016), which allows for offsets between sectors. We assumed a model with a simple sinusoidal variability. The photometric data were obtained with UNPOPULAR (Hattori et al. 2022), which implements casual pixel model detrending to retain stellar variability.

Using all six sectors, a period peak of 26.4 is found at $\Delta \log L = 26.6$ with a sinusoidal flux (half) amplitude of 0.0105% (105 ppm). Treating all normalised sectors without offsets in the periodogram search again yields 26.4 d but with reduced significance ($\Delta \log L = 14.6$) and slightly reduced amplitude 0.009% (89 ppm) variability, suggesting the modulation is present across the Sector timescale, and not a windowing effect due to allowing for offsets. Further investigation of only Sectors 67 and 68, which show the highest photometric amplitude among the six sectors, returns a peak period of 27.2 d and sinusoidal amplitude of 0.115% (115 ppm). Sectors 27 and 28 return peak period of 13.4 d (99 ppm), but with a second peak at 27.5 d (84 ppm), whereas Sectors 94 and 95 return peaks at 6.2 d (110 ppm), 18.0 d (113 ppm) and an indistinct broad peak / inflection at 25.7 d (114 ppm). The shorter period maximum peaks in Sectors 27 and 28 and Sectors 94 and 95 appear to be harmonics of the ~ 27 d rotation period, implying changing activity. Importantly, while 27 d is close to the FWHM periodicities, we also note that it essentially matches the *TESS* sector length, with the harmonics matching *TESS* momentum dumps and the spacecraft orbital period of ~ 13.5 d.

The Keplerian solution for HD 2134 with *kima* is multi-modal, with samples also predominantly appearing at 26.3 and 21.5 d in addition to the 32-day signal. Thus, while the candidate planet signal is coincident with the 32-day FWHM signal and close to some *TESS* photometric periodicities, it is distinct from the predicted rotation periods. Taking this into account, we refrain from announcing that this signal is planetary in nature here, and refer to it only as a planet candidate signal. As such the signal is not considered in the occurrence rate calculations, and is shown as a grey point in Figure 2. Further data are required to determine the significance of the other RV and FWHM periodicities, since they are also closer to the predicted stellar rotation period. A more detailed analysis of this system will be presented in Barnes et al. (2025) (in prep).

HD 67200 (DMPP-6): Our RVs for HD 67200 provide strong evidence ($\text{BF} > 31,000$) in favour of two Keplerians with orbital periods of 7.6 and 36.4 d, corresponding to minimum masses of 5.8 and $13.5 M_{\oplus}$, respectively. We designate these planets as DMPP-6 b and DMPP-6 c (Figure 6), and subtract their signals from the dataset to compute detection limits.

There is also moderate evidence ($\text{BF} = 36$) for a third periodic signal in the RV data, with a period of ~ 3 d and minimum mass of $2.2 M_{\oplus}$ (indication of this signal can be seen in Figure B9. This signal appears alongside the 7.6 and 36.4 d periods in the highest-likelihood three-planet solution.

We find $v \sin i = 2.4 \pm 0.9 \text{ km s}^{-1}$ and $R_* = 1.27 \pm 0.01 R_{\odot}$ using SPECIES. A most probable $P_{\text{rot}} = 19.2$ d is found, while for fixed mean and maximum inclinations (see HD 2134 above) of $i = 57.3^\circ$ and $i = 90^\circ$, the respective $P_{\text{rot}} = 18.9$ and 22.7 d. The pre-COVID data set shows an activity-RV Pearson’s linear correlation of $|r| < 0.28$. The M_3 , BIS, FWHM and S-index post-COVID correlations are weak to moderate with, respectively, $r = -0.19, 0.26, -0.43$ and 0.32, but large uncertainties in r are a reflection of the small (20 observations) data set. Only S-index shows a significant periodicity at 15.99 d, with other peaks at longer periods, including 29.8 d. While this may be related to the expected rotation period, it is not coincident with any of the candidate Keplerian periodicities. With a

⁶ see <https://archive.stsci.edu/missions-and-data/tess> and *TESS* archive manual at <https://outerspace.stsci.edu/display/TESS/TESS+Archive+Manual>

declination of -70.0° , HD 67200 has been observed fairly continuously by *TESS* in 42 sectors during Years 1, 3, 5 and 7. We split the data into odd and even sectors for Years 1 and 3 since they contain respectively 12 and 13 sectors with usable full frame images (sectors 7 and 95, were rejected due to extraction issues with the full frame images). The semi-amplitudes of the sinusoidal fits arising from periodogram analysis are between 30 ppm and 49 ppm. However, we do not find consistent periods for the data sets considered. For Year 1 (odd), Year 1 (even), Year 3 (odd), Year 3 (even), Year 5 and Year 7, we find respectively $P = 10.4, 6.23, 13.7, 10.7, 4.52$ and 3.65 d with semi-amplitudes of 48, 30, 47, 46, 38, 49 ppm and $\Delta \log L = 24.3, 10.2, 28.8, 26.1, 17.9, 36.4$ d. We note that the Year 1 (even) data set does not recover any significant periods, while the Year 1 (odd) data set finds significant periodicity. Additional peaks at around 10–15 d are common, even when the peak power lies at lower period, but these often appear with $\Delta \log L < 15$. The sinusoidal amplitudes for HD 67200, one of our brightest targets ($V = 7.7$) are relatively low. It is likely that systematics related to the *TESS* orbit and photometric extraction remain at these amplitudes and thus preclude reliable identification of periodicities at constant amplitude with periodogram analyses.

Despite this, we note that the periodicities for HD 67200 are not inconsistent with the S-index periodicities derived from our spectra. A more detailed examination of HD 67200 will be presented in Barnes et al. (2025).

When calculating the detection limits for HD 67200/DMPP-6, we initially forced *kima* to fit $N_p = 1$ signal to the residual (subtracted) dataset. However, the resulting posterior samples predominantly clustered around the 3.2 d signal. This is expected, as the 3.2 d candidate was not subtracted from the data. Notably, when following the detection-limit recovery methodology described in Section 4.2, we found that the sampler did not explore other regions of the period space. In this case, it was necessary to set $N_p = 2$ to enable adequate exploration of the entire period range. This was the only system in our sample for which this adjustment was required, and supports the reality of the 3.2-day signal, despite the merely moderate statistical evidence in the initial model comparison.

HD 118006 (DMPP-7): We find strong evidence for a planetary signal in the radial velocity (RV) data of HD 118006, with BF $> 20,700$ in favour of a single-planet model. The planet, henceforth designated DMPP-7b, has an orbital period of 4.98 d and an RV semi-amplitude of 21.8 m s^{-1} , corresponding to a minimum mass of $61.4 M_\oplus$. Although there is weak evidence for a second signal (BF = 9.2), the current data set of 19 observations is insufficient to confirm the presence of additional planets.

HD 118006 was classified as a G1V star by (Houk & Swift 1999). Our SPECIES age estimate of $3.87^{+0.28}_{-0.31}$ Gyr and $\log g = 4.17 \pm 0.09$ confirm main sequence status, but are at tension with the corresponding radius estimate of $R_* = 1.49 \pm 0.02 R_\odot$, which implies evolved status. Further, an independent radius estimate using parameters derived from the Gaia mission also returns $R_* = 1.64 \pm 0.04 R_\odot$. We find $v \sin i = 3.04 \pm 0.74 \text{ km s}^{-1}$ from SPECIES, yielding a most probable $P_{\text{rot}} = 19.8$ d. The method for obtaining rotational velocities described by Murphy et al. (2016) simultaneously fits for the macroturbulent velocity, giving $v \sin i = 2.6^{+2.3}_{-2.6} \text{ km s}^{-1}$. This shifts the most probable $P_{\text{rot}} = 12.6$ d, indicating sensitivity of the Monte Carlo estimate to the $v \sin i$ value and its uncertainty. Nevertheless, neither estimate is coincident with the large RV signal. RV-activity correlations for M_3 , BIS, FWHM and S-index are respectively $r = -0.04, 0.02, -0.13$ and 0.32 ($p = 0.88, 0.94, 0.59$ and 0.19) indicating weak or no correlations. There are no significant periodicities evident in the activity indicators. Likelihood periodogram

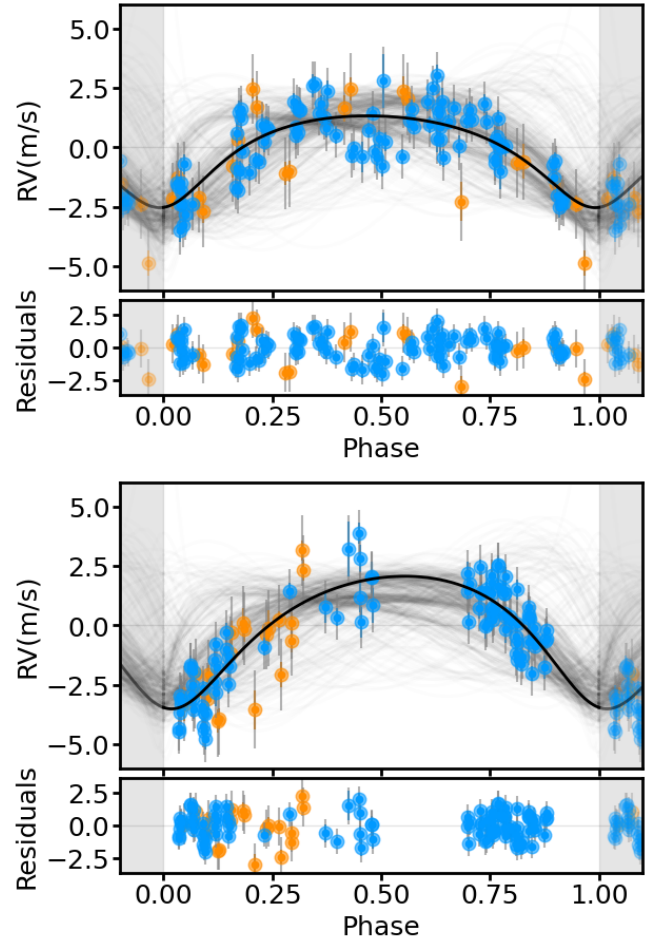


Figure 6. Phased Keplerian RV models of HD 67200 / DMPP-6 b (top) HD 67200 / DMPP-6 c (bottom) with HARPS data post-fibre upgrade (blue) and HARPS data post-COVID warm-up (orange) and their respective residuals. The additional RV jitter term has been added to the plotted uncertainties and is shown by the grey error bars. Faded Keplerian models are based on 500 randomly drawn posterior samples from a *kima* run. The shaded regions display the repeating signal.

analysis of *TESS* Sectors 23, 46, 50 and 91 indicates significant periodicity, with peak power of $\Delta \log L = 15.0$ at 21.5 d and with a sinusoidal semi-amplitude of 111 ppm. A low significance peak cluster at 9.6 d ($\Delta \log L = 10.4$ is also present) and may be a harmonic of the 21.5 d peak. There is no significant power at the 4.98 d period seen in the RVs.

Figure 7 shows the Keplerian fit for HD 118006/DMPP-7b. The observational cadence results in clustered data points, as the planet’s orbital period is near an integer number of days, causing periodic observational gaps from the Earth’s diurnal cycle. Figure 1 presents the detection limits for the system, after subtracting the most likely posterior sample, with parameters as stated in Table C1.

HD 122640: For this system we find a BF $> 14,000$ in favour of a single planet solution with a period of 138.5 d on an eccentric orbit with $e \sim 0.3$. However, for this target we have two datasets, one pre HARPS fibre upgrade and another post HARPS COVID warm-up with a large separation of > 1500 d between them. Our sampling within each of these datasets is limited to three tightly sampled periods of ~ 2 , ~ 4 , and ~ 10 d each, yielding an effective timespan of ~ 16 d. The offset between the two datasets introduces

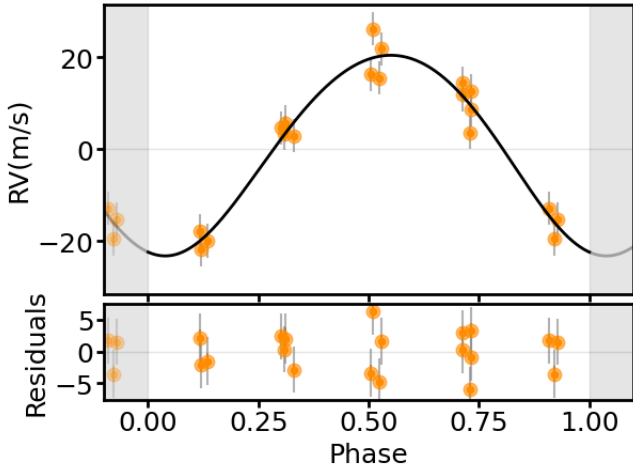


Figure 7. Phased Keplerian Radial-Velocity (RV) model of HD 118006 / DMPP-7 b with HARPS data post-COVID warm-up (orange) and associated residuals after removing the planetary signal. The additional RV jitter term has been added to the plotted uncertainties and is shown by the grey error bars. No random samples are shown for this signal as the eccentricity is unconstrained and consistent with 0. The shaded regions display the repeating signal.

uncertainty about the signal: we suspect this signal is not planetary in nature, arising instead from poor sampling. Therefore, the signal is not included in any of our occurrence rate calculations, and is represented by a grey circle in Figure 2.

We do not see any strong evidence for short-period signals. When limiting the period search to <20 d, highly eccentric solutions are found with a large number of posterior samples near the upper end of the period prior.

Therefore, we subtract the 138.5 d signal from the dataset for the detection limit analysis, but restrict our analysis to orbital periods <20 d.

HD 191122 (DMPP-8): hosts a very clear 62.92 d, $81.1 M_{\oplus}$ signal which we henceforth refer to as DMPP-8 b, with weak evidence for additional signals. See Figure 8 for a phase plot of the radial velocity signal of DMPP-8 b. Inspection of the detection limit plot for this target reveals a concentration of posterior samples near an orbital period of ≈ 4.8 days. This feature is suggestive of an additional planetary signal consistent with the DMPP hypothesis (Haswell et al. 2020); however, the Bayes factor in favour of a two-planet model is only 2.3. The penultimate post-COVID warmup RV data point is derived from a spectrum with low counts (S/N in order 50 = 31). Further observations are required to confirm the source of this additional signal.

With SPECIES, we find $v \sin i = 2.13 \pm 0.83 \text{ km s}^{-1}$ and $R_* = 1.24 \pm 0.01 R_{\odot}$, yielding a most probable $P_{\text{rot}} = 24.2$ d. There are too-few data in the post-COVID set for useful correlation statistics. The pre-fibre upgrade data RV-activity Pearson’s correlations for M_3 , BIS, FWHM and S-index are respectively $r = -0.39, -0.42, -0.13$ and 0.35 indicating moderate-weak correlations, with low confidence for rejecting the null hypothesis of no correlation ($p = 0.11, 0.08, 0.60$ and 0.15). Periodicities close to the most probable $P_{\text{rot}} = 23.8$ d are notable in M_3 at $P = 23.1$ d and BIS at $P = 27.7$ d and S-index at $P = 21.5$ d and 25.4 d, but the respective significances of these periods of $\Delta \log L = 9.3, 7.2, 7.4$ and 6.0 are low. There is no evidence that the ~ 63 d signal we identify as DMPP-8 b is due to stellar activity. More data are needed to assess these periodicities further in conjunction with the tentative 4.8 d signal. Periodogram

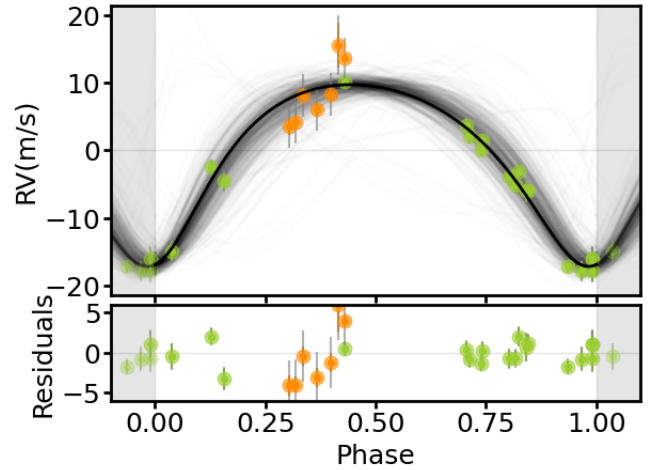


Figure 8. Phased Keplerian Radial-Velocity (RV) models of HD 191122 / DMPP-8 b with HARPS data pre-fibre upgrade (green) and HARPS data post-COVID warm-up (orange) along with associated residuals after removing the planetary signal. The additional RV jitter term has been added to the plotted uncertainties and is shown by the grey error bars. Faded Keplerian models are based on 500 randomly drawn posterior samples from a kima run. The shaded regions display the repeating signal.

analysis of photometry from seven TESS sectors yield a low significance peak ($\Delta \log L = 11.6$) at 9.7 d with corresponding 55 ppm sinusoidal flux semi-amplitude. There are no significant periodicities at >10 d.

The posterior sample with the highest likelihood subtracted from our data to calculate the detection limit for the system can be found in Table C1.

HD 200133 (DMPP-9): For this target, a single planet solution is preferred with $\text{BF} > 26,140$. The signal (Figure 9) has an orbital period of 12.73 d, and a RV semi-amplitude of 3.8 m s^{-1} corresponding to a $14.4 M_{\oplus}$ planet (see Figure E21). SPECIES yields $v \sin i = 3.22 \pm 0.68 \text{ km s}^{-1}$ and $R_* = 1.26 \pm 0.01 R_{\odot}$, from which we find a most probable $P_{\text{rot}} = 16.2$ d. HD 200133 was observed in the post-fibre upgrade interval only. There are no indications of significant periodicity in M_3 , BIS or S-index, with Pearson’s correlations of $0.07 < |r| < 0.14$. The FWHM periodogram peak at 13.8 d is close to the Markov Chain (MC) derived most probable period and recovered Keplerian periodicity, but shows low significance of $\Delta \log L = 9.5$ or 5% FAP.

HD 200133 was observed in TESS sectors 13, 27, 67 and 94. The dominant period peak is found at 10.9 d with $\Delta \log L = 26.3$ with 89 ppm semi-amplitude. Weaker peaks at 4.1 d and 24.2 d are seen with marginal or low significances of $\Delta \log L = 15.4$ and 8.9 . With four sectors from different cycles, there are likely not sufficient data on the timescales of the longer low-significance candidate rotation period.

As there is no significant evidence for activity periodicities at the RV period, and we did not obtain any posterior samples at this period, we accept the RV signal planet candidate and henceforth refer to this signal as DMPP-9 b. For the HD 200133/DMPP-9 detection limit calculation, the posterior sample with the highest likelihood with eccentricity < 0.2 was subtracted as the posterior samples corresponding to the signal are consistent with a circular orbit. The subtracted signal parameters can be found in Table C1.

Table 3. Orbital parameters for planetary signals identified in this work. For eccentricities with posterior distributions consistent with zero we provide the 1-sigma upper limit of the distribution.

Planet name	Period [days]	K [m s ⁻¹]	e	ω [rad]	$m_p \sin i$ [M_\oplus]	T_0 [BJD-2400000]	a [AU]
DMPP-2 c	3.168 ^{+0.355} _{-0.002}	17.99 ^{+1.76} _{-2.02}	< 0.28	2.00 ^{+0.62} _{-0.48}	51.79 ^{+5.43} _{-5.49}	57524.30 ^{+0.22} _{-0.75}	0.04789 ^{+0.00327} _{-0.00049}
DMPP-2 d	16.491 ^{+0.067} _{-0.053}	18.21 ^{+1.32} _{-1.38}	< 0.1	4.66 ^{+1.01} _{-3.61}	91.79 ^{+6.11} _{-7.32}	57516.66 ^{+3.69} _{-4.02}	0.1432 ^{+0.0012} _{-0.0013}
HD 67200 / DMPP-6 b	7.6027 ^{+0.0261} _{-0.0016}	1.93 ^{0.30} _{-0.27}	0.34 ^{+0.11} _{-0.14}	3.06 ^{+0.39} _{-0.80}	5.80 ^{+0.94} _{-0.80}	58862.32 ^{+0.42} _{-3.71}	0.0779 ^{+0.0016} _{-0.0012}
HD 67200 / DMPP-6 c	36.441 ^{+0.077} _{-0.070}	2.54 ^{+0.26} _{-0.30}	< 0.31	3.11 ^{+0.66} _{-0.49}	13.47 ^{+1.60} _{-1.97}	58842.50 ^{+19.79} _{-13.59}	0.2206 ^{+0.0033} _{-0.0039}
HD 118006 / DMPP-7 b	4.984 ^{+0.069} _{-0.061}	21.82 ^{+1.40} _{-1.41}	< 0.1	2.97 ^{+1.22} _{-1.27}	61.39 ^{+4.33} _{-4.06}	59996.46 ^{+1.45} _{-0.81}	0.05873 ^{+0.00086} _{-0.00089}
HD 191122 / DMPP-8 b	62.915 ^{+0.041} _{-0.033}	13.58 ^{+0.64} _{-0.69}	0.275 ^{+0.049} _{-0.049}	3.26 ^{+0.21} _{-0.22}	81.09 ^{+7.09} _{-7.10}	54205.20 ^{+2.34} _{-2.12}	0.3098 ^{+0.0098} _{-0.0108}
HD 200133 / DMPP-9 b	12.733 ^{+0.584} _{-0.524}	3.80 ^{+0.66} _{-0.59}	< 0.25	2.665 ^{+1.367} _{-1.373}	14.43 ^{+2.57} _{-2.36}	57586.981 ^{+2.458} _{-2.279}	0.1097 ^{+0.0041} _{-0.0037}

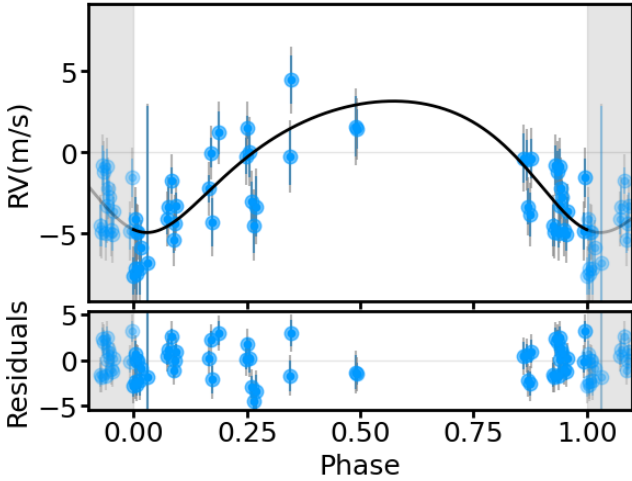


Figure 9. Phased Keplerian Radial-Velocity (RV) models of HD 200133 / DMPP-9 b with HARPS data post-fibre upgrade (blue) along with associated residuals after removing the planetary signal. The additional RV jitter term has been added to the plotted uncertainties and is shown by the grey error bars. No random samples are shown for this signal as the eccentricity is unconstrained and consistent with 0. The shaded regions display the repeating signal.

4.6 Planet abundance for the DMPP survey

Figure 2 presents the completeness of the DMPP survey alongside the corresponding planet occurrence rates. Our survey achieves near-complete sensitivity ($\sim 100\%$) to planets with masses greater than $30 M_\oplus$ and orbital periods up to 20 d. We also reach $\sim 95\%$ completeness for planets with masses above $10 M_\oplus$ and periods shorter than 5 d.

In our most sensitively searched systems, HD 39194 and HD 181433, we are capable of detecting Earth-mass planets with orbital periods ≤ 5 d, based on 288 and 208 spectra, respectively (see Figures B7 & B19). Survey completeness declines rapidly for periods exceeding 20 days, consistent with our focus on short-period planet detection.

The occurrence rates plotted in Figure 2 suggest a high abundance of terrestrial-mass planets ($< 10 M_\oplus$) within orbital periods of 20 d. Our survey sensitivity declines with decreasing mass as expected. The observational strategy means we are formally most sensitive at the shortest periods, however the methodology does not take into account the correlated astrophysical systematic effects which arise due to plasma flows in the stellar photospheres. The effects on measured RVs of super-granulation are correlated on 1-2 d timescales, and reduce the effectiveness of our sub-day sampling to resolve RVs due

to low mass planets in short period orbits. We have clearly detected a $2.67 M_\oplus$ planet in a 5.6 d orbit (DMPP-3A b) but due to super-granulation we only have a single planet signal detection $< 4 M_\oplus$ for $P < 5$ d (HD 28471 / DMPP-5 b; Stevenson et al. 2025a). Despite this we do have some moderate evidence for planets in/below this bin: the ~ 2.5 d $1.08 M_\oplus$ signal in DMPP-3, the 2.78 d, $2.69 M_\oplus$ signal in HD 2134, and the ~ 3 d $2.2 M_\oplus$ signal in HD 67200 / DMPP-6. Further observations are urgently required to confirm these detections.

As demonstrated for HD 39194 and HD 181433, additional observations would allow us to detect terrestrial-mass planet signals in our sample, thereby increasing survey completeness and improving the accuracy of our occurrence rates.

4.6.1 Comparison with other RV planet occurrence rates

The DMPP project aimed to pre-select stars hosting hot, mass-losing planets using the signatures of circumstellar absorption in their spectra before embarking on RV observations to search for them. If the hypothesis underlying DMPP is correct, we should expect significantly higher occurrence rates of short period planets for the DMPP targets than for the targets of other RV planet searches. To examine this, in Table 4 we compare our results with occurrence rates reported by other RV surveys involving FGK-type stars in Howard et al. (2010), Mayor et al. (2011), and Bashi et al. (2020). We see the DMPP sample exhibits significantly higher planetary occurrence rates, supporting the DMPP hypothesis laid out in Haswell et al. (2020).

The prior works enumerated in Table 4 assumed circular planetary orbits when calculating occurrence rates, citing Endl et al. (2002) as a justification. In contrast, our analysis demonstrates that this assumption is no longer best practice for deriving detection limits and, consequently, occurrence rates. For a more detailed critique of the continued use of Endl et al. (2002) to justify circular orbit assumptions, we refer the reader to Standing et al. (2022).

To allow a more direct comparison of our results with those of Howard et al. (2010), Mayor et al. (2011), and Bashi et al. (2020), we apply a correction to account for their circular orbit assumption. Specifically, we apply a uniform correction of 8% to our survey completeness (see Section 4.4) and recalculate our occurrence rates. The corrected values are presented in Table 4. Even after this correction, the DMPP survey demonstrates a far higher planetary occurrence rate compared to large samples of FGK stars. We note that increasing the completeness within a given parameter space region results in a decrease in the inferred occurrence rates, as described by Equation 2. This occurs because the number of detected planets remains constant, whereas the total number of systems capable of detecting such planets, yet showing no detection, increases.

Table 4. Comparison of occurrence rates from the DMPP survey with other RV works for periods shorter than 50 days. Also included are the DMPP rates corrected to assume circular orbits.

	3 – 10 M_{\oplus}	10 – 30 M_{\oplus}	30 – 100 M_{\oplus}
Howard et al. (2010)	11.8 ± 4.3%	6.5 ± 3%	1.6 ± 1.2%
Mayor et al. (2011)	16.6 ± 4.4%	11.1 ± 2.4%	1.2 ± 0.5%
Bashi et al. (2020)	10.0 ± 2.0%	6.0 ± 1.0%	–
This work	83.0 ^{+27.1} _{-24.4} %	27.0 ^{+15.0} _{-11.2} %	13.9 ^{+11.8} _{-7.5} % ¹
This work (circular)	70.5 ^{+23.0} _{-20.7} %	24.5 ^{+13.6} _{-10.2} %	12.8 ^{+10.9} _{-6.9} %

¹ HD 118006/DMPP-7 could be an evolved star (see section 4.5). When removing this planet from the calculations we obtain 9.3^{+11.0}_{-6.0}% and 8.5^{+10.1}_{-5.5}% respectively.

Additional comparisons with *Kepler* occurrence rates are not feasible without making strong and uncertain assumptions about the planet mass–radius relation in this specific population.

Based on these occurrence rates, we estimate the number of sub-basal stars expected in a representative local stellar population. Following Staab (2018), approximately 1.4% of main-sequence (MS) stars exhibit sub-basal activity. From *Gaia* DR3 (Gaia Collaboration et al. 2023), we selected all MS stars with $V < 12$ within 500 pc, yielding 16,776 stars and implying ~ 241 sub-basal objects. This calculation is intended as a population-level estimate only; the DMPP survey targets a substantially smaller and brighter subset of stars ($V < 10$, $d < 100$ pc), and therefore a much lower absolute number of sub-basal stars is expected in that sample.

Using our occurrence rate statistics for planets with orbital periods $P < 50$ d from Table 4, we estimate the potential number of planets as follows:

- Planets with masses 3–10 M_{\oplus} : 200⁺⁶⁵₋₅₉
- Planets with masses 10–30 M_{\oplus} : 65⁺³⁶₋₂₇
- Planets with masses 30–100 M_{\oplus} : 22.4⁺²⁷₋₁₄

These values provide a first-order expectation for the number of planets detectable in the selected sample of nearby, bright MS stars with sub-basal activity.

We also estimate the observational efficiency of the DMPP survey purely in terms of the number of observations (OBs) per planet detection. The DMPP program obtained a total of 1,336 OBs on the 29 targets contributing to 16 detected planets (excluding previously known systems such as HD 181433, HD 39194, and HD 89839), corresponding to approximately 93 OBs per planet. For comparison, the Eta Earth survey (Howard et al. 2010) had 5,259 OBs for 34 detections (~ 155 OBs per planet), while Bashi et al. (2020) reported $> 8,316$ OBs for 55 planets (> 151 OBs per planet). Thus, the DMPP survey is roughly 55% more efficient in terms of OBs per detection relative to these previous programs. However, we note (i) that this is calculated assuming a standard integration time for each of the observations in the aforementioned surveys and (ii) the effectiveness of the DMPP observations was hampered by correlated noise due to stellar super-granulation, so the current DMPP observing protocols have an even more pronounced efficiency gain.

4.7 Demographics of the DMPP sample

Fig 10 shows our planets compared to the population of other known planets. In mass-period space, the DMPP planets are broadly distributed in a similar way to the known population, with some clear differences. It is immediately clear that we have not detected any plan-

ets with orbital periods ~ 1 d. The reasons for this may be twofold: (i) correlated RV noise due to stellar supergranulation makes such periods difficult to detect via RVs, even if the data sampling is designed to do so. (ii) Such close-in planets experience profound irradiation, leading to equilibrium temperatures $\gtrsim 2000$ K. They may have lost a lot of mass, and hence be below our RV detection threshold. There are also no discoveries of DMPP planets with masses exceeding 0.6 M_J . There are two possible reasons for this: (i) many of the known hot Jupiters are fairly distant, and were discovered because their transits are relatively deep and thus easy to detect. We limited our sample to main sequence FGK stars within ~ 100 pc, so it is unsurprising we do not find examples of an intrinsically rare population. Lower mass planets are much more plentiful, and thus well represented within our volume-limited sample. (ii) Our targets were selected based on the signature of planetary mass loss, and mass loss is inhibited by the strong gravity of a massive planet. Four of the planet discoveries lie along the upper boundary of the Neptune Savannah.

We searched the TESS light curves for transiting planets orbiting our targets, but the shallow (~ 100 ppm) transits of terrestrial planets across FGK stars are challenging to reach with TESS. As more sectors of TESS data accumulate and the detrending techniques for TESS light curves improve, such transits may be found. Furthermore, the forthcoming PLATO mission may reveal transits of the short period, edge-on planets originally anticipated by DMPP (Haswell et al. 2020).

In mass-radius space, the DMPP planets below the Neptune Savannah appear to straddle the radius valley, but we note that we have only model-derived radii from Müller et al. (2024), so this is merely indicative. Nonetheless, it is clear that among the sub-Neptune and lower mass DMPP discoveries that the shorter period planets are more likely to be below the radius valley, while those with longer periods lie above it. This is consistent with the hypothesis that the DMPP systems have recent or ongoing planetary mass loss: instellation and mass loss are more likely for the closer-in planets. However, it is also true to say that the broader population of known exoplanets also exhibit this property, which could also be attributed to the simple fact that the stronger instellation at shorter periods leads the locus of the radius valley to be inclined to larger radii at shorter periods.

5 CONCLUSIONS

We conducted a blind search of 24 systems in the DMPP radial-velocity survey, designed to test the hypothesis of Haswell et al. (2020) that stars exhibiting sub-basal chromospheric activity are preferentially orbited by short-period, mass-losing planets. Our analysis yields the following main results:

(i) We detect a total of 24 planetary signals in the sample, including 7 newly discovered planets: DMPP-2 c & d, DMPP-6 b & c, DMPP-7 b, DMPP-8 b, and DMPP-9 b along with updated solutions in previously published systems.

(ii) For six systems with previously published planets — DMPP-1, DMPP-2, DMPP-3, HD 181433, HD 39194, and HD 89839 — we update the orbital parameters of 16 planetary signals using homogeneous kima fits, with expanded datasets.

(iii) We compute robust 99% confidence detection limits for each of our systems, taking into account eccentric orbits and using the methodology of Standing et al. (2022). From these, we derive survey completeness as a function of planet mass and orbital period.

(iv) Using the completeness maps, we calculate planet occurrence rates for the DMPP sample in well-sampled regions of parameter space (Figure 2). For periods < 50 d, the occurrence rates

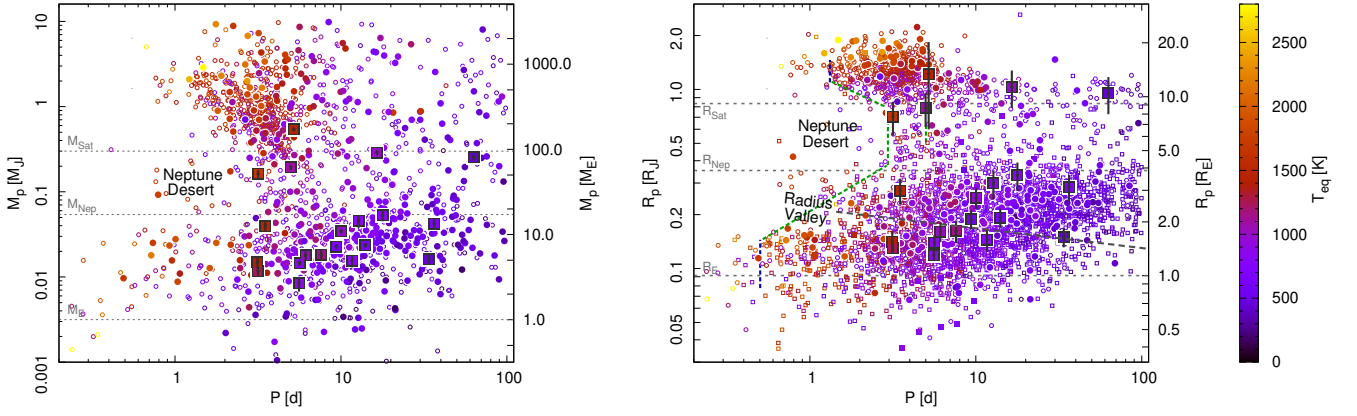


Figure 10. Mass-Period and Radius-Period diagrams for the detected DMPP planets (large filled squares) and other known planets from the NASA Exoplanet Archive (<https://exoplanetarchive.ipac.caltech.edu> on 2025/11/14). The DMPP radii and ranges (vertical bars) are predicted from their minimum masses using the relationships from (Müller et al. 2024). The archival planets with mass or minimum mass determinations are plotted with circles in both panels, while planets with only radius measurements are plotted with squares in the Radius-Period panel. Archival planets are divided into those with $V < 10$ (larger filled symbols) and those with $V \geq 10$ (smaller open symbols). The Neptune Desert boundaries (green and blue dashed) are taken from Castro-González et al. (2024). The Radius Valley (grey dashed curve) is taken from the hydrodynamic model prediction of Affolter et al. (2023), and is here defined as $R_p(P) = (1.88/11.2)(P/10)^{-0.11} M_J$.

are $83.0^{+27.1}_{-24.4}\%$ for $3\text{--}10 M_\oplus$ planets, $27.0^{+15.0}_{-11.2}\%$ for $10\text{--}30 M_\oplus$, and $13.9^{+11.8}_{-7.5}\%$ for $30\text{--}100 M_\oplus$.

(v) Comparing with other radial-velocity surveys (Table 4), we find the DMPP sample exhibits significantly higher planet occurrence rates than a random sample of FGK-type stars, strongly supporting the DMPP hypothesis.

(vi) Based on ~ 241 nearby main-sequence stars with sub-basal activity and our measured occurrence rates, we estimate that roughly 200, 65, and 22 planets with masses $3\text{--}10$, $10\text{--}30$, and $30\text{--}100 M_\oplus$, respectively, and short orbital periods ($P < 50$ days) could be waiting to be discovered in such systems.

(vii) The DMPP survey made ~ 93 observations per discovered planet, compared to ~ 155 for Eta Earth (Howard et al. 2010) and > 151 for Bashi et al. (2020). DMPP is approximately 40% more efficient purely in terms of observations per planet detection. However, we note that this is calculated assuming a standard integration time for each of the observations in the aforementioned surveys.

(viii) Further systematic observations, e.g. 1 epoch per night over an extended period, would ameliorate the affect of 1-2 d correlations in RVs due to stellar photospheric flows (super-granulation) and should yield additional low mass hot planet discoveries.

Angular momentum considerations imply the circumstellar material lost from hot planets will be concentrated in the orbital plane of the mass-losing planet. This means the DMPP planets are particularly likely to be in edge-on orientations. Despite this, no transits have been repeatedly detected. The hot planets are likely to be small as they will have lost their gaseous envelopes, and $\sim 1 M_\oplus$ planets orbiting FGK stars produce transit depths $\lesssim 100$ ppm.

The DMPP planets exhibit demographics rather similar to the overall population (Fig. 10). This may imply that planetary mass loss is ubiquitous for the known short period exoplanet systems. In this interpretation, the special property of the DMPP sample is most likely that their host stars are intrinsically particularly chromospherically quiet, so any circumstellar absorption depresses the apparent activity below the basal value. For a moderately active system, depressing the apparent activity simply makes the star appear less active. This has important implications for the selection of targets hosting short

period planets for intensive transit spectroscopy: their host stars may be more active than their $\log R'_{\text{HK}}$ values indicate.

ACKNOWLEDGEMENTS

M.R.S acknowledges support from the European Space Agency as an ESA Research Fellow, and was supported by grant ST/T000295/1 from the Science and Technology Facilities Council (STFC) for the early part of this work. JRB and CAH were supported by grants ST/T000295/1, and ST/X001164/1 from STFC. ATS and ZOBR were supported by STFC studentships.

We thank the anonymous referee for their comments to improve the quality and clarity of this manuscript. We thank Thomas Baycroft for comments which helped to improve the manuscript. Some data products used in this publication were taken on observing runs where funding was assisted by travel grants from the Royal Astronomical Society (RAS), allowing postgraduate students the opportunity to get in-person experience of observational astronomy that had previously been hindered by the COVID-19 pandemic.

This work used Astropy, numpy, pandas, scipy, corner, and matplotlib packages.

DATA AVAILABILITY

The data used in this work is available for download at the ESO public archive⁷.

Programme IDs for the HARPS data, for stars in Table A1-A3 072.C-0488(E), 077.C-0364(E), 079.C-0927(B,C), 081.C-0148(A), 085.C-0019(A), 087.C-0368(A,B), 087.C-0531(A), 088.C-0662(A,B), 089.C-0497(A,B), 089.C-0732(A), 090.C-0421(A), 091.C-0866(A,B,C), 091.C-0936(A), 092.C-0721(A), 093.C-0409(A), 095.C-0551(A), 095.C-0799(A), 096.C-0460(A), 096.C-0499(A), 096.C-0876(A), 097.C-0390(B), 098.C-0269(A,B), 098.C-0366(A), 098.C-0499(A), 099.C-0458(A), 099.C-0798(A),

⁷ http://archive.eso.org/eso/eso_archive_main.html

0100.C-0097(A) 0100.C-0836(A), 0102.C-0558(A), 0103.C-0432(A), 0106.C-1067(A), 0108.C-0879(A), 0110.C-4334(A), 183.C-0972(A), 192.C-0836(A), 192.0852(A,M), 196.C-1006(A), 2107.C-5066(A).

REFERENCES

- Affolter L., Mordasini C., Oza A. V., Kubyskhina D., Fossati L., 2023, *A&A*, **676**, A119
- Agol E., et al., 2021, *PSJ*, **2**, 1
- Anglada-Escudé G., Butler R. P., 2012, *ApJS*, **200**, 15
- Anglada-Escudé G., et al., 2013, *A&A*, **556**, A126
- Anglada-Escudé G., et al., 2016, *Nature*, **536**, 437
- Balsalobre-Ruza O., et al., 2025, *A&A*, **694**, A15
- Barnes J. R., et al., 2020, *Nature Astronomy*, **4**, 419
- Barnes J. R., et al., 2023, *MNRAS*, **524**, 5196
- Barnes J. R., Jeffers S. V., Haswell C. A., Damasso M., Del Sordo F., Liebing F., Perger M., Anglada-Escudé G., 2024, *MNRAS*, **534**, 1257
- Barnes J. R., Haswell C. A., Standing M. R., Ross Z. O. B., Staab D., submitted 2025, *MNRAS*
- Bashi D., Zucker S., Adibekyan V., Santos N. C., Tal-Or L., Trifonov T., Mazeh T., 2020, *A&A*, **643**, A106
- Bennett D. P., Ranc C., Fernandes R. B., 2021, *AJ*, **162**, 243
- Borucki W. J., et al., 2010, *Science*, **327**, 977
- Bouchy F., et al., 2009, *A&A*, **496**, 527
- Buchholz B., Ulmschneider P., Cuntz M., 1998, *ApJ*, **494**, 700
- Campanella G., Nelson R. P., Agnor C. B., 2013, *MNRAS*, **433**, 3190
- Castro-González A., Bourrier V., Lillo-Box J., Delisle J.-B., Armstrong D. J., Barrado D., Correia A. C. M., 2024, *A&A*, **689**, A250
- Clayton Z. R., van Saders J. L., Cao L., Pinsonneault M. H., Teske J., Beaton R. L., 2024, *ApJ*, **962**, 47
- Clopper C. J., Pearson E. S., 1934, *Biometrika*, **26**, 404
- Cochran W. D., Hatzes A. P., 1994, *Ap&SS*, **212**, 281
- Cosentino R., et al., 2012, in McLean I. S., Ramsay S. K., Takami H., eds, *Society of Photo-Optical Instrumentation Engineers (SPIE) Conference Series Vol. 8446, Ground-based and Airborne Instrumentation for Astronomy IV*. p. 84461V, doi:10.1117/12.925738
- Cumming A., Butler R. P., Marcy G. W., Vogt S. S., Wright J. T., Fischer D. A., 2008, *PASP*, **120**, 531
- Endl M., Kürster M., Els S., Hatzes A. P., Cochran W. D., Dennerl K., Döbereiner S., 2002, *A&A*, **392**, 671
- Faria J. P., Santos N. C., Figueira P., Brewer B. J., 2018, *The Journal of Open Source Software*, **3**, 487
- Faria J. P., et al., 2022, *A&A*, **658**, A115
- Figueira P., et al., 2025, *arXiv e-prints*, p. arXiv:2507.07514
- Foreman-Mackey D., 2016, *The Journal of Open Source Software*, **1**, 24
- Fossati L., et al., 2010, *ApJ*, **714**, L222
- Fossati L., Ayres T. R., Haswell C. A., Bohlender D., Kochukhov O., Flöer L., 2013, *ApJ*, **766**, L20
- Gaia Collaboration 2020, *VizieR Online Data Catalog: Gaia EDR3 (Gaia Collaboration, 2020)*, *VizieR On-line Data Catalog: I/350*. Originally published in: 2021A&A...649A...1G; doi:10.5270/esa-lug, doi:10.26093/cds/vizieR.1350
- Gaia Collaboration et al., 2023, *A&A*, **674**, A1
- Grieves N., et al., 2022, *A&A*, **668**, A29
- Haswell C. A., 2010, *Transiting Exoplanets*
- Haswell C. A., et al., 2012, *ApJ*, **760**, 79
- Haswell C. A., et al., 2020, *Nature Astronomy*, **4**, 408
- Hattori S., Foreman-Mackey D., Hogg D. W., Montet B. T., Angus R., Pritchard T. A., Curtis J. L., Schölkopf B., 2022, *AJ*, **163**, 284
- He M. Y., Triaud A. H. M. J., Gillon M., 2017, *MNRAS*, **464**, 2687
- Henry T. J., Soderblom D. R., Donahue R. A., Baliunas S. L., 1996, *AJ*, **111**, 439
- Høg E., et al., 2000, *A&A*, **355**, L27
- Horner J., et al., 2019, *AJ*, **158**, 100
- Houk N., Swift C., 1999, *Michigan Spectral Survey*, **5**, 0
- Howard A. W., et al., 2010, *Science*, **330**, 653
- Jeffreys H., 1961, *Theory of probability*. Oxford University Press
- John A. A., et al., 2023, *MNRAS*, **525**, 1687
- Kipping D. M., 2013, *MNRAS*, **434**, L51
- Klein B., et al., 2024, *MNRAS*, **531**, 4238
- Kumaraswamy P., 1980, *Journal of Hydrology*, **46**, 79
- Laskar J., 1997, *A&A*, **317**, L75
- Laskar J., 2000, *Phys. Rev. Lett.*, **84**, 3240
- Liebing F., et al., 2024, *A&A*, **690**, A234
- Lo Curto G., et al., 2015, *The Messenger*, **162**, 9
- Martin D. V., et al., 2019, *A&A*, **624**, A68
- Mayor M., Queloz D., 1995, *Nature*, **378**, 355
- Mayor M., et al., 2011, *arXiv e-prints*, p. arXiv:1109.2497
- McInnes L., Healy J., Astels S., 2017, *The Journal of Open Source Software*, **2**
- Müller S., Baron J., Helled R., Bouchy F., Parc L., 2024, *A&A*, **686**, A296
- Murphy S. J., Fossati L., Bedding T. R., Saio H., Kurtz D. W., Grassitelli L., Wang E. S., 2016, *MNRAS*, **459**, 1201
- Pace G., 2013, *A&A*, **551**, L8
- Paegert M., Stassun K. G., Collins K. A., Pepper J., Torres G., Jenkins J., Twicken J. D., Latham D. W., 2021, *arXiv e-prints*, p. arXiv:2108.04778
- Pepe F., et al., 2002, *The Messenger*, **110**, 9
- Pepe F., et al., 2021, *A&A*, **645**, A96
- Perruchot S., et al., 2008, in McLean I. S., Casali M. M., eds, *Society of Photo-Optical Instrumentation Engineers (SPIE) Conference Series Vol. 7014, Ground-based and Airborne Instrumentation for Astronomy II*. p. 70140J, doi:10.1117/12.787379
- Petigura E. A., Marcy G. W., Howard A. W., 2013, *ApJ*, **770**, 69
- Pollacco D. L., et al., 2006, *PASP*, **118**, 1407
- Rappaport S., et al., 2012, *ApJ*, **752**, 1
- Rutten R. G. M., Schrijver C. J., Lemmens A. F. P., Zwaan C., 1991, *A&A*, **252**, 203
- Schrijver C. J., 1987, *A&A*, **172**, 111
- Silva A. M., et al., 2022, *A&A*, **663**, A143
- Soto M. G., Jenkins J. S., 2018, *A&A*, **615**, A76
- Staab D., 2018, PhD thesis, Open University Milton Keynes, UK
- Staab D., et al., 2020, *Nature Astronomy*, **4**, 399
- Standing M. R., et al., 2022, *MNRAS*, **511**, 3571
- Standing M. R., et al., 2023, *Nature Astronomy*, **7**, 702
- Stevenson A. T., Haswell C. A., Barnes J. R., Barstow J. K., Ross Z. O. B., 2023, *MNRAS*, **523**, 189
- Stevenson A. T., Haswell C. A., Barnes J. R., Standing M. R., Barstow J. K., Ross Z. O. B., Freckelton A. V., Staab D., 2025a, *MNRAS*,
- Stevenson A. T., Haswell C. A., Faria J. P., Barnes J. R., Barstow J. K., Dickinson H., Standing M. R., 2025b, *MNRAS*, **539**, 727
- Trevisan M., Barbuy B., Eriksson K., Gustafsson B., Grenon M., Pompéia L., 2011, *A&A*, **535**, A42
- Trifonov T., Tal-Or L., Zechmeister M., Kaminski A., Zucker S., Mazeh T., 2020, *A&A*, **636**, A74
- Unger N., et al., 2021, *A&A*, **654**, A104
- Vidal-Madjar A., Lecavelier des Etangs A., Désert J. M., Ballester G. E., Ferlet R., Hébrard G., Mayor M., 2003, *Nature*, **422**, 143
- Wright J. T., 2004, *The Astronomical Journal*, **128**, 1273
- Xiao G.-Y., et al., 2023, *Research in Astronomy and Astrophysics*, **23**, 055022
- Zechmeister M., et al., 2018, *A&A*, **609**, A12

APPENDIX A: TARGET TABLES

Here we present the targets of the survey along with relevant properties and parameters.

Table A1. DMPP targets with ≥ 10 observations studied in this analysis. Uncertainties are given in the brackets, as the last two significant figures, except for σ_{jit} where uncertainties can be significantly asymmetric. Values taken from runs before signals were subtracted. Stellar masses are taken from Gaia FLAME (Final Luminosity Age Mass Estimator) (Gaia Collaboration 2020) except where previously published.

	BD+03580	DMPP-1	DMPP-2	DMPP-3	DMPP-4	HD28471 (DMPP-5)	HD103991
<i>System properties</i>							
TIC	-	66560666	32432767	141765836	26884478	38698692	428657196
Gaia DR2	3283466836680393472	3011005587574818432	5017319806652067072	5266148569447305600	2136027771930903808	4675222436007028608	3492834741329
α [deg] ¹	04:16:40.66	05:47:06.26	01:49:37.89	06:06:29.85	19:34:19.79	04:25:09.15	11:58:27.87
δ [deg] ¹	03:41:56.0	-10:37:48.8	-34:27:32.9	-72:30:45.6	+51:14:11.8	-64:04:48.25	-23:38:08.8
V mag ²	9.83(04)	7.98(01)	8.57(01)	9.09	5.703(30) ³	7.91	9.49
Distance [pc] ¹	134.28(32)	62.599(83)	135.93(34)	47.06(25)	25.431(18)	22.870(19)	40.988(33)
M [M_{\odot}] ¹	0.995(45)	1.21(03)	1.41(04)	0.900(09)	1.25(02) ³	0.980(44) ⁴	0.810(97) ⁵
<i>System parameters</i>							
γ [km s ⁻¹]	145401.4(1.9)	28660.6(2.6)	7544.2(2.9)	-667.3(2.6)	0.2(1.3) ³	54126.93(55) ⁴	75172.40(48)
σ_{jit} [m s ⁻¹]	4.3 ^{+1.7} _{-1.3}	0.96 ^{+0.11} _{-0.13} , 5.4 ^{+1.9} _{-1.6}	4.14 ^{+1.23} _{-1.15}	8.24 ^{+1.63} _{-3.28} , 0.59 ^{+0.21} _{-0.51} , 3.68 ^{+1.22} _{-0.67} , 0.54 ^{+0.22} _{-0.17}	0.82 ^{+0.79} _{-0.73}	2.25 ^{+0.65} _{-0.48} , 0.48 ^{+0.09} _{-0.09} , 1.37 ^{+0.54} _{-0.53}	1.36 ^{+0.62} _{-0.45}
RV Offsets [m s ⁻¹]	-	-5.88 ^{+2.42} _{-2.8}	-	-140.01 ^{+1.83} _{-2.62} , 12.35 ^{+1.97} _{-2.82} , 17.21 ^{+4.93} _{-14.79}	-	16.12 ^{+0.22} _{-0.65} , 21.11 ^{+1.32} _{-0.92}	-

Notes: 1 - Gaia Collaboration (2020), 2 - Høg et al. (2000), 3 - Barnes et al. (2023), 4 - Stevenson et al. (2025a), 5 - Paegert et al. (2021)

Table A2. Table A1 continued.

	HD118006 (DMPP-7)	HD122640	HD135204	HD143424	HD144840	HD149079	HD149189
<i>System properties</i>							
TIC	365158631	60737418	38838329	410724316	411083824	402834325	25428659
Gaia DR2	3663051957490779264	6273522428481412224	4418203587193988480	6262841463297004672	4341712281239980032	5815781787804787456	5940913632776578432
α [deg] ¹	13:34:06.87	14:03:37.18	15:13:50.89	16:00:42.77	16:08:24.49	16:36:51.41	16:35:25.33
δ [deg] ¹	00:29:56.6	-27:00:35.9	-01:21:05.0	-15:24:43.7	-13:08:07.8	-65:35:12.2	-48:41:54.0
V mag ²	8.80(02)	9.26(02)	6.60	9.11	9.15	7.68(01)	9.448(63)
Distance [pc] ¹	102.28(19)	63.148(69)	17.2650(89)	39.722(26)	28.264(17)	48.876(44)	93.58(15)
M [M_{\odot}] ¹	1.09(04)	0.90(11) ³	0.94(12) ³	0.84(10) ³	0.762(04)	1.07(04)	1.08(04)
<i>System parameters</i>							
γ [km s ⁻¹]	-36650.21(96)	-44533.3(5.2)	-74159.98(45)	-13208.73(55)	-37916.3(1.4)	28400.53(87)	-17763.78(74)
σ_{jit} [m s ⁻¹]	3.51 ^{+0.89} _{-0.71}	0.25 ^{+0.49} _{-0.22} , 1.95 ^{+0.59} _{-0.48}	1.27 ^{+0.55} _{-0.39}	1.66 ^{+0.52} _{-0.48}	1.76 ^{+1.11} _{-0.95}	2.70 ^{+0.76} _{-0.59}	1.16 ^{+0.28} _{-0.28} , 3.7 ^{+1.9} _{-1.3} , 0.91 ^{+1.18} _{-0.78}
RV Offsets [m s ⁻¹]	-	1.38 ^{+4.65} _{-4.63}	-	-	-	-	14.73 ^{+2.46} _{-0.89} , 20.15 ^{+2.93} _{-3.26}

Notes: 1 - Gaia Collaboration (2020), 2 - Høg et al. (2000), 3 - Paegert et al. (2021)

DMPP - Occurrence rates

17

Table A3. Table A1 continued.

	HD181433	HD191122 (DMPP-8)	HD200133 (DMPP-9)	HD210975	HD2134	HD39194	HD58489
<i>System properties</i>							
TIC	410399074	318042295	376777782	60111044	290575588	389506883	173079045
<i>Gaia</i> DR2	6434153380720177664	6349054822860923008	6401028668786744960	6612306455196349056	4635564769579703936	4657193606465368704	558559466482065152
α [deg] ¹	19:25:09.57	20:21:13.24	21:05:13.30	22:14:34.80	00:24:26.62	05:44:31.92	07:24:04.61
δ [deg] ¹	-66:28:07.7	-81:36:57.3	-66:57:28.3	-32:18:29.8	-78:15:01.4	-70:08:36.9	-40:02:45.8
V mag ²	8.38	8.63(01)	9.20(01)	9.55	8.82(01)	8.075(12)	9.74
Distance [pc] ¹	26.990(15)	76.036(79)	110.09(18)	31.665(18)	71.443(61)	26.439(14)	43.101(19)
M [M_{\odot}] ¹	0.86(06) ^{3,4}	0.99(04)	1.10(04)	0.760(84) ⁵	0.92(04)	0.86(04)	0.770(94) ⁵
<i>System parameters</i>							
γ [km s ⁻¹]	39776.76(19)	12534.29(62)	11649.12(78)	23886.53(61)	4262.53(53)	7688.02(09)	-14901.9(1.3)
σ_{jit} [m s ⁻¹]	0.93 ^{+0.75} _{-0.44} , 1.61 ^{+0.93} _{-0.63} , 0.84 ^{+0.11} _{-0.11}	2.9 ^{+1.7} _{-1.3} , 0.60 ^{+0.84} _{-0.56}	1.41 ^{+0.32} _{-0.31}	2.7 ^{+0.51} _{-0.43}	1.18 ^{+0.16} _{-0.14}	1.58 ^{+0.59} _{-0.41} , 3.4 ^{+0.99} _{-0.69} , 1.17 ^{+0.09} _{-0.10}	0.34 ^{+3.20} _{-0.31} , 12.6 ^{+3.0} _{-2.4} , 3.7 ^{+1.1} _{-1.8}
RV Offsets [m s ⁻¹]	4.21 ^{+0.64} _{-0.65} , 21.28 ^{+1.16} _{-1.04}	-10.18 ^{+2.33} _{-2.01}	-	-	-	10.14 ^{+0.61} _{-0.62} , 15.82 ^{+1.19} _{-1.19}	1.75 ^{+3.61} _{-3.59} , 7.74 ^{+3.90} _{-3.62}

Notes: 1 - [Gaia Collaboration \(2020\)](#), 2 - [Høg et al. \(2000\)](#), 3 - [Trevisan et al. \(2011\)](#), 4 - [Horner et al. \(2019\)](#), 5 - [Paegert et al. \(2021\)](#)

Table A4. Table A1 continued.

	HD67200 (DMPP-6)	HD85249	HD89839
<i>System properties</i>			
TIC	306668068	445976787	294028147
<i>Gaia</i> DR2	5270480576538756352	5308568655781883264	5355799586503538176
α [deg] ¹	08:01:32.54	09:48:52.01	10:20:40.54
δ [deg] ¹	-53:39:50.7	-53:35:07.07	-70:01:26.0
V mag ²	7.70(01)	8.53	7.64(01)
Distance [pc] ¹	54.438(41)	92.85(15)	57.144(60)
M [M_{\odot}] ³	1.079(45)	1.207(040)	1.21(03)
<i>System parameters</i>			
γ [km s ⁻¹]	15044.3(1.1)	8784.2(165.2)	31755.60(58)
σ_{jit} [m s ⁻¹]	0.88 ^{+0.09} _{-0.08} , 1.42 ^{+0.38} _{-0.27}	2.79 ^{+1.13} _{-1.37} , 4.79 ^{+1.05} _{-0.92}	1.62 ^{+0.59} _{-0.51} , 2.31 ^{+0.57} _{-0.49} , 2.58 ^{+0.82} _{-0.99}
RV Offsets [m s ⁻¹]	-13.58 ^{+1.08} _{-1.09}	439.89 ^{+69.7} _{-557.88}	18.15 ^{+1.24} _{-1.18} , 32.24 ^{+2.13} _{-2.33}

Notes: 1 - [Gaia Collaboration \(2020\)](#), 2 - [Høg et al. \(2000\)](#), 3 - [Xiao et al. \(2023\)](#)

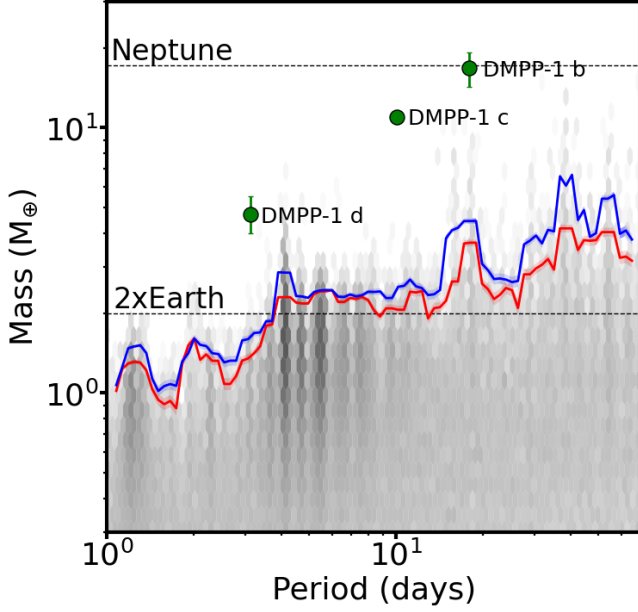


Figure B1. Detection limit plot for target DMPP-1. The standard 3σ (99%) detection limit is plotted in blue and the corresponding 3σ limit calculated using only posterior samples with $e_p < 0.1$ is plotted in red.

APPENDIX B: DETECTION LIMITS

Here we present the individual detection limits for each of our systems as in Figure 1. Green points on the plots are detected planetary signals with errorbars from the uncertainties in Table 2 or Table 3.

APPENDIX C: SUBTRACTED SIGNALS

In this section, we present the signals subtracted from our datasets in order to calculate individual detection limits, and overall occurrence rates.

APPENDIX D: PHASE PLOTS OF PREVIOUSLY PUBLISHED SIGNALS

Here we present the phase plots of the posterior samples with the highest likelihoods for each of the signals presented in Section 4.3.

APPENDIX E: SIGNAL CORNER PLOTS

Here we present the corner plots of posterior sample distributions for the orbital parameters of each of the signals presented in Tables 2 and 3.

This paper has been typeset from a \LaTeX file prepared by the author.

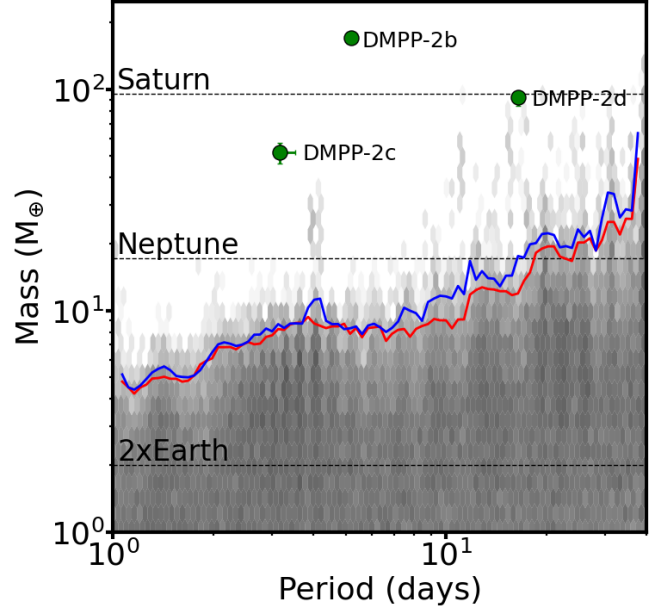


Figure B2. As for Fig B1, but for DMPP-2.

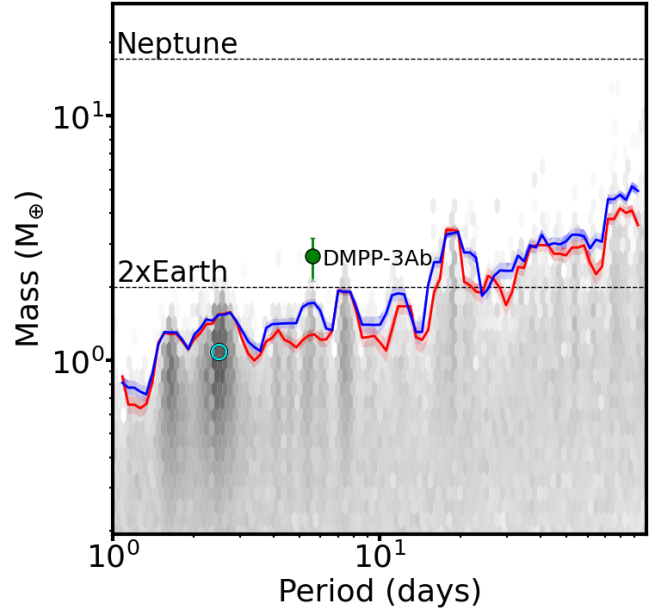


Figure B3. As for Fig B1, but for DMPP-3. Open cyan circle represents candidate planetary signal.

Table A5. Observation metrics for the targets analysed in this work. This table details the number of observations, mean SNR, standard deviation of the SNR, min/max SNR, date of first/last observation in BJD-2,450,000, and the standard deviation in the FWHM and BIS. All columns are combined values across all runs/instruments.

Star	N_{obs}	SNR	σ_{SNR}	minSNR	maxSNR	Start BJD	End BJD	σ_{FWHM} [m s^{-1}]	σ_{BIS} [m s^{-1}]
BD+03580	10	60.787	10.529	45.953	76.280	59995.546	60004.533	4.890	4.907
DMPP-1	158	154.715	27.795	63.740	220.522	57375.590	60004.519	3.831	2.308
DMPP-2	48	98.103	26.363	49.161	153.552	57286.789	57762.650	74.491	38.860
DMPP-3	135	89.614	17.621	43.095	119.012	54579.565	60290.595	5.970	5.855
DMPP-4	71	215.420	35.680	137.700	302.810	57141.602	58698.714	26.530	7.700
HD28471	122	153.739	31.047	75.559	217.029	52945.805	60004.641	5.734	1.515
HD103991	17	80.149	8.068	69.218	94.284	59994.787	60004.893	8.423	3.503
HD118006	19	81.948	9.718	61.741	98.909	59994.868	60004.840	8.619	5.499
HD122640	32	83.012	9.524	62.568	104.322	57893.611	60004.759	6.657	2.687
HD135204	15	230.594	27.648	181.027	269.509	59994.815	60004.825	5.973	1.427
HD143424	15	81.231	7.300	67.085	90.509	59994.825	60004.811	7.208	3.397
HD144840	14	92.008	12.501	57.086	105.698	59994.837	60004.875	5.770	4.687
HD149079	14	129.245	15.061	100.647	167.660	59994.799	60004.861	7.184	2.965
HD149189	55	98.767	20.148	52.793	147.166	54365.583	60004.783	4.928	2.639
HD181433	10	113.370	31.806	34.019	192.008	52942.567	60004.847	8.330	2.246
HD191122	25	65.524	17.570	29.677	99.046	54250.813	60004.902	7.982	4.728
HD200133	54	71.162	18.277	28.498	100.113	57286.741	57895.875	7.563	3.932
HD210975	26	74.725	14.569	51.037	107.556	52944.543	56604.553	9.061	3.360
HD2134	87	86.225	21.352	29.958	127.848	57286.763	57895.858	6.172	3.430
HD39194	12	133.034	28.030	50.371	200.140	52944.821	60004.631	10.245	2.029
HD58489	40	63.636	17.480	31.334	95.421	53016.705	60004.703	26.896	3.963
HD67200	114	170.410	32.068	61.829	230.789	57722.754	60004.686	4.868	1.582
HD85249	31	108.161	22.707	66.746	149.240	57722.846	60004.675	24.262	11.970
HD89839	22	88.764	51.271	30.198	223.655	53056.737	60004.732	10.979	7.650

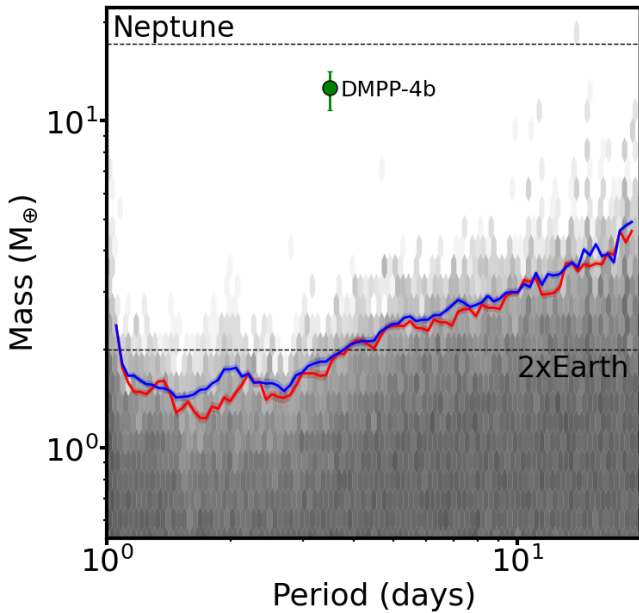
**Figure B4.** As for Fig B1, but for DMPP-4.

Table C1. Parameters from highest likelihood posterior samples, subtracted from the dataset in order to calculate detection limits and subsequently survey completeness and occurrence rates.

System name	Period [days]	Semi-amplitude [m s^{-1}]	Eccentricity	ω	Φ	T_0 [BJD-2400000]
DMPP-1 b	17.8274043	4.10470933	0.14730062	6.11995822	5.29753014	57360.55902469
DMPP-1 c	9.7862891	3.03337298	0.18263751	2.9558394	3.70120839	57369.82504398
DMPP-1 d	3.14234479	1.79225768	0.12322107	4.80563562	2.58193113	57374.29853571
DMPP-2 b	5.20333937	49.41240186	0.02721602	2.67882508	3.73374387	57283.69665724568
DMPP-2 c	3.16795946	18.48087325	0.24555166	1.86990002	0.75230228	57286.409401262965
DMPP-2 d	16.48508291	17.98622006	0.11366426	5.46727443	2.91853125	57279.1314102009
DMPP-3 b	5.58964908	1.34811473	0.46766518	1.74460343	0.31757298	57434.797185626136
DMPP-3 B	506.868256	2669.806406	0.59748	2.775321	6.178657	56936.64378758205
DMPP-3+	809.034509	2.498941	0.0	1.689299	3.115262	57033.952889478205
DMPP-4 b	3.49813174	5.01401372	0.0257469	4.64726898	6.13782424	57138.1843813
HD 28471 / DMPP-5 b	2.87573122	1.28665949	0.16181718	2.80163733	5.92074613	52943.095250861246
HD 28471 / DMPP-5 c	6.20937197	1.86215241	0.10760704	0.52039189	4.44622571	52945.0822669725
HD 28471 / DMPP-5 c	8.8655346	1.7087995	0.03719353	1.75942746	0.37183296	52945.28044449285
HD 181433 b	9.37467082	2.73659688	0.4107677	3.51456492	2.45042423	52938.91044288627
HD 181433 c	1018.37583726	17.27654281	0.24951593	0.16561441	0.73142406	52178.00334389883
HD 181433 d	6973.28325926	8.53881203	0.45943362	4.39295463	5.30304593	47057.07381393424
HD 39194 b	5.63687105	1.73455193	0.00822653	3.81388864	5.72521668	52939.6850636518
HD 39194 c	14.03121165	2.22851883	0.02362284	1.29771115	0.08663022	52944.627903897315
HD 39194 d	33.87735548	1.20269546	0.02740975	6.14602254	6.13660265	52911.734342374424
HD 118006 / DMPP-7 b	5.0162790	22.05399487	0.0573552	2.99923775	4.4909205	59991.28245223
HD 122640	138.49425273	5.89333551	0.2976916	4.16233507	1.70658196	57855.99452034
HD 191122 / DMPP-8 b	62.90705511	13.49436464	0.28556875	3.31680284	4.54104098	57082.39283831
HD 200133 / DMPP-9 b	12.73459852	4.24859186	0.1998315	2.526275345	1.53505777	57283.62956265
HD 2134	32.41548814	2.45926102	0.19273226	0.65488088	0.0808832	57286.34669756
HD 67200 / DMPP-6 b	7.60135752	1.89331578	0.38473448	3.29490636	0.16647627	57722.55283184016
HD 67200 / DMPP-6 c	36.40340479	2.69770204	0.21762472	3.07693338	4.44622571	57696.993772094065

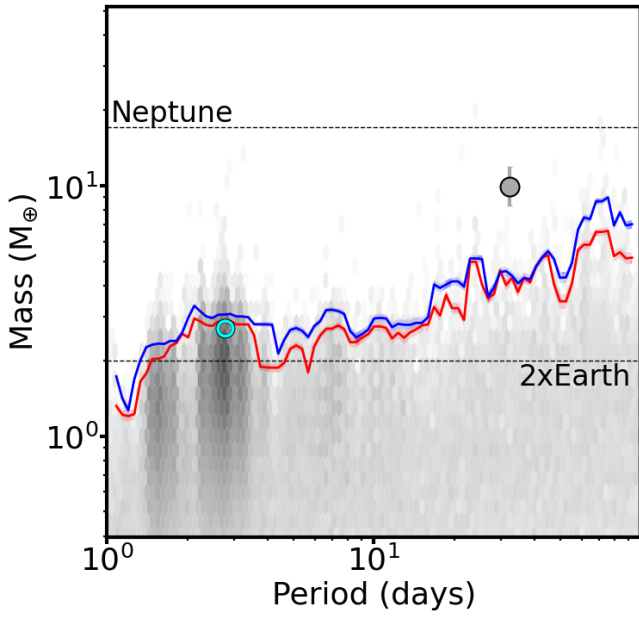


Figure B5. As for Fig B1, but for HD 2134. Grey circle represents the subtracted signal we attribute to activity. Open cyan circle represents candidate planetary signal.

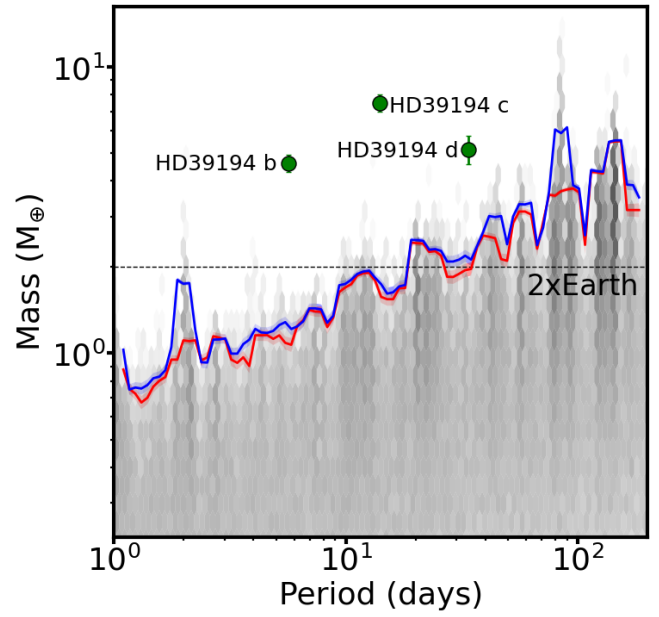


Figure B7. As for Fig B1, but for HD 39194.

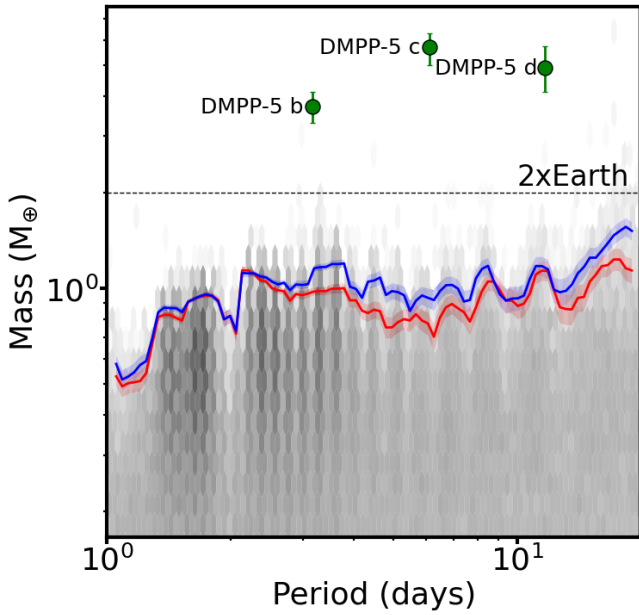


Figure B6. As for Fig B1, but for HD 28471 / DMPP-5.

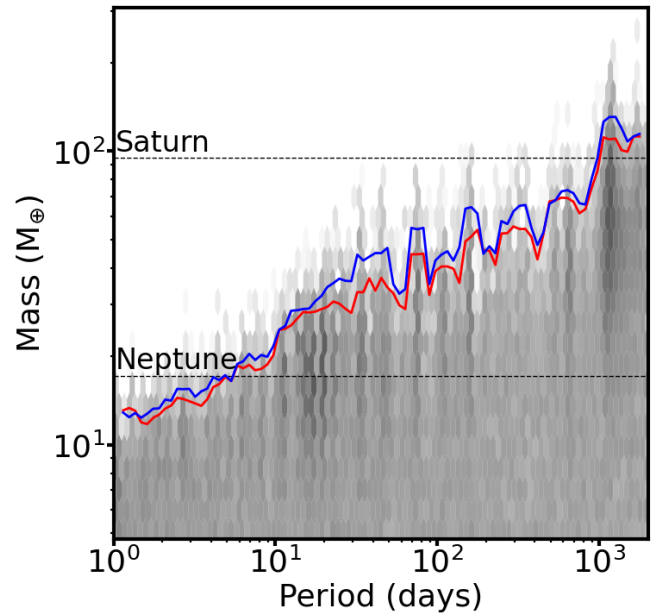


Figure B8. As for Fig B1, but for HD 58489.

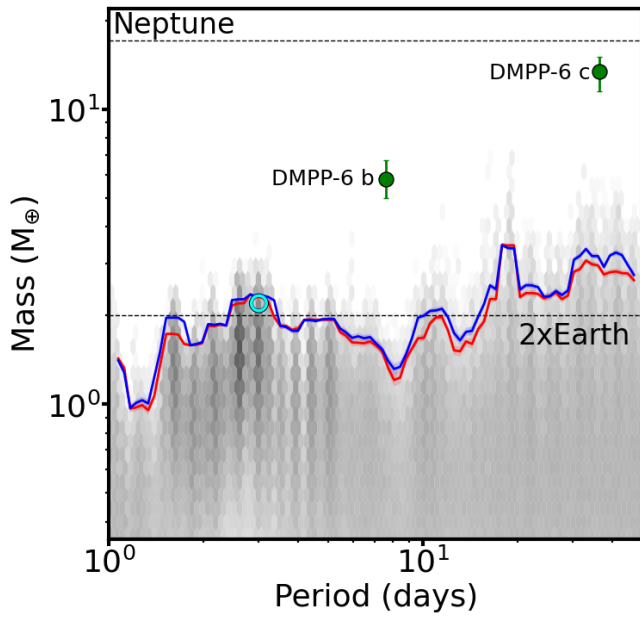


Figure B9. As for Fig B1, but for HD 67200 / DMPP-6. Open cyan circle represents candidate planetary signal.

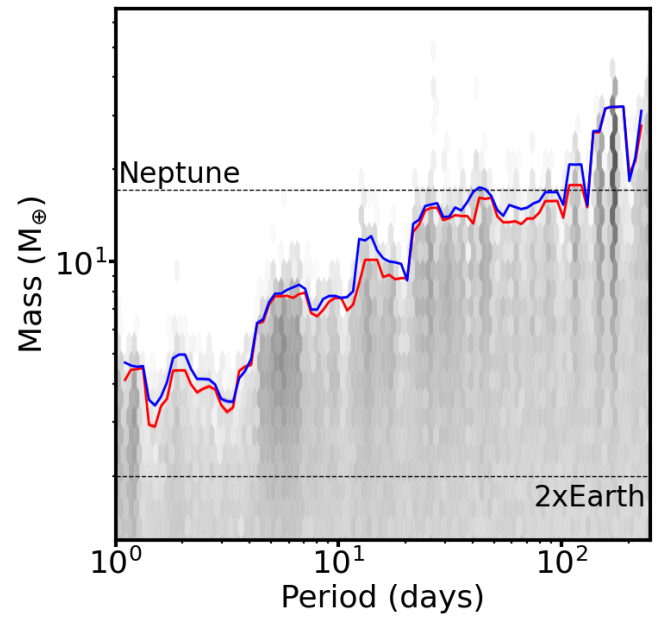


Figure B11. As for Fig B1, but for HD 89839.

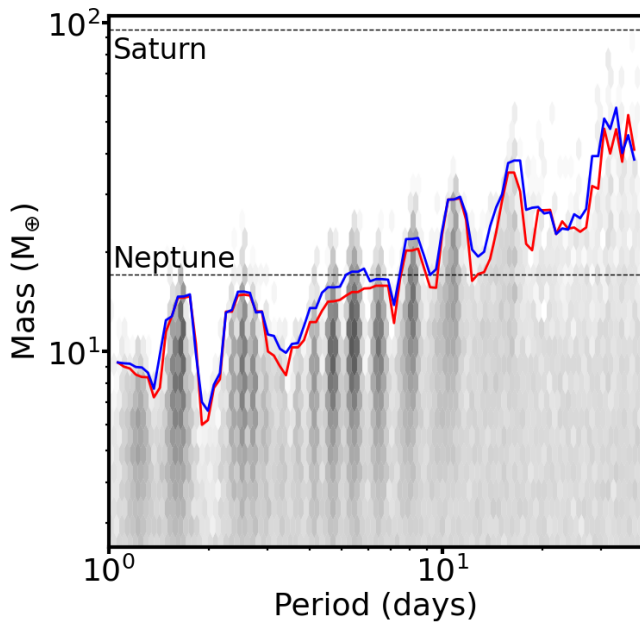


Figure B10. As for Fig B1, but for HD 85249.

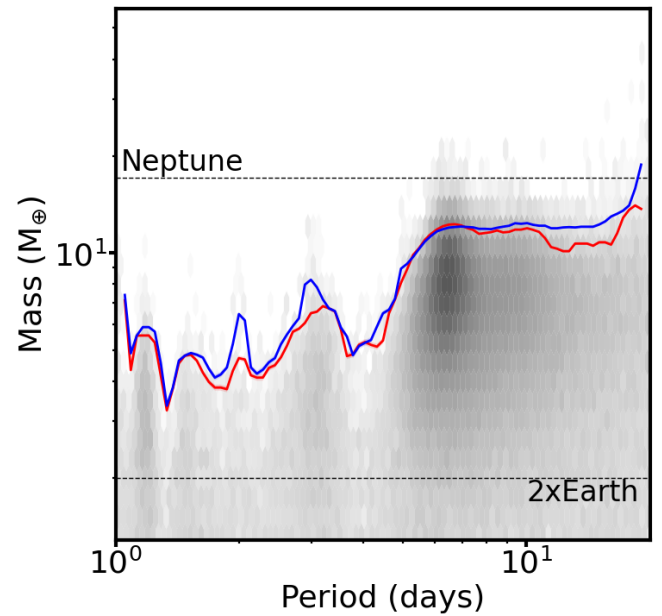


Figure B12. As for Fig B1, but for HD 103991.

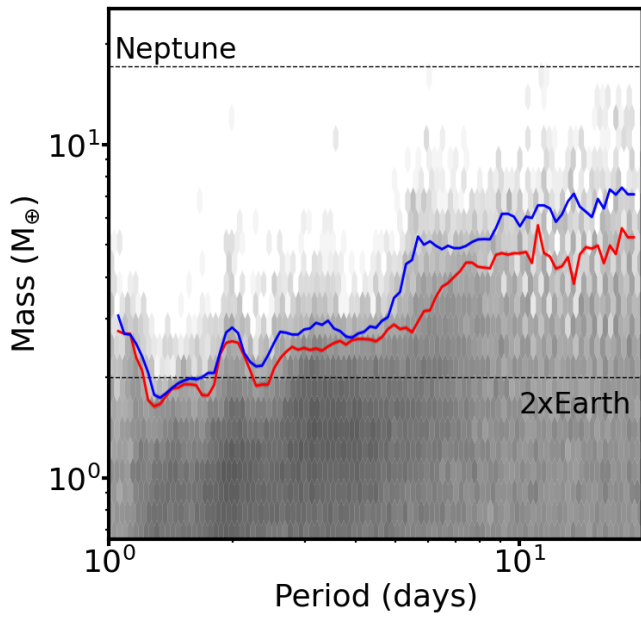


Figure B13. As for Fig B1, but for HD 122640. The removed signal from Table C1 has a mass of $\sim 44M_{\oplus}$ and is out of the scale of the plot.

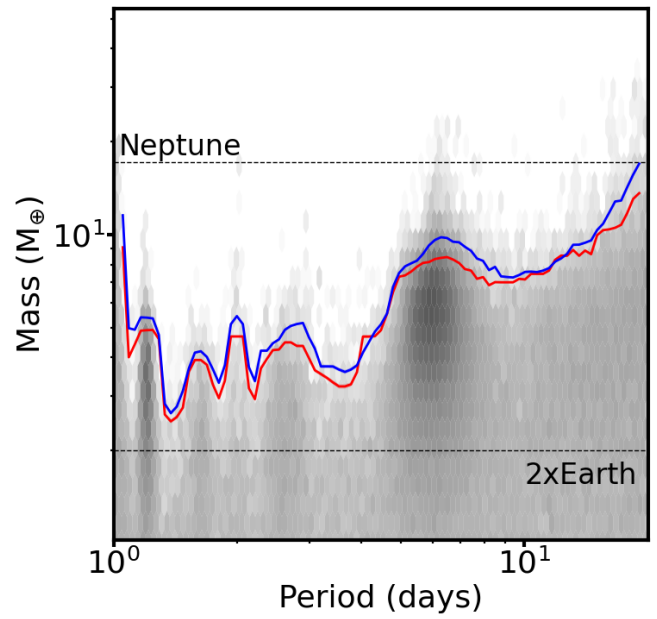


Figure B15. As for Fig B1, but for HD 143424.

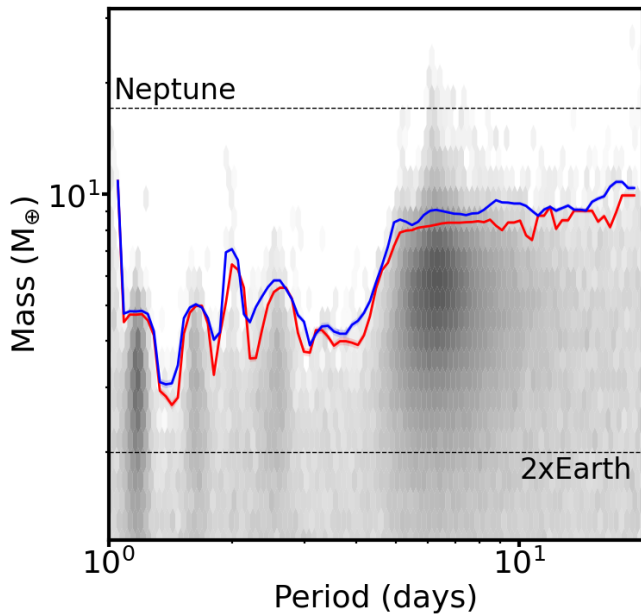


Figure B14. As for Fig B1, but for HD 135204.

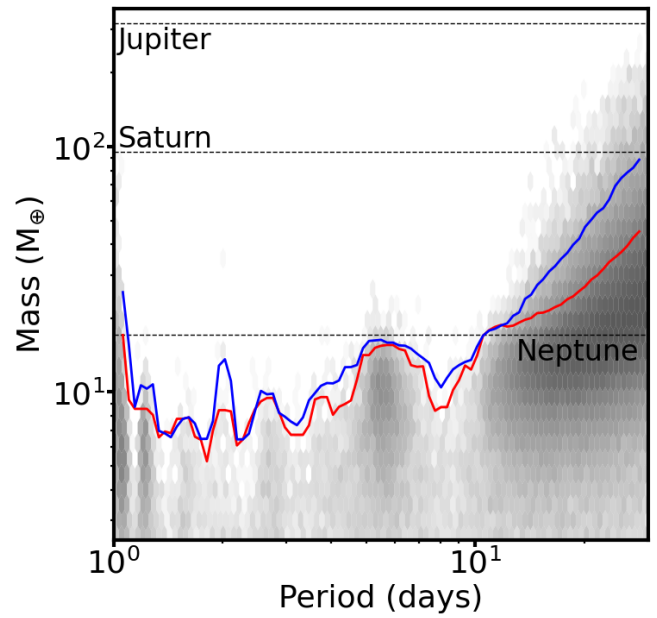


Figure B16. As for Fig B1, but for HD 144840.

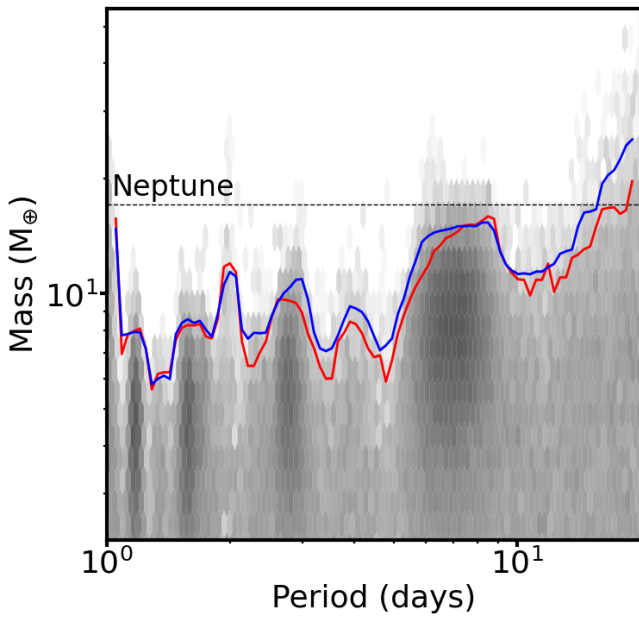


Figure B17. As for Fig B1, but for HD 149079.

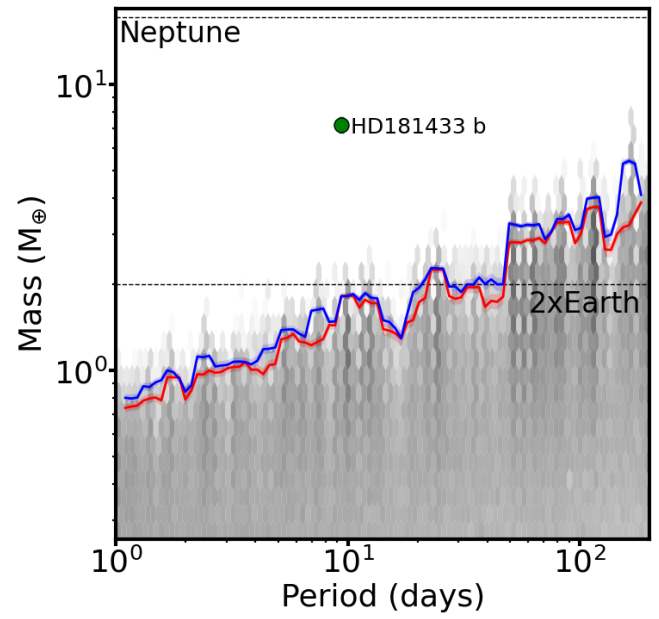


Figure B19. As for Fig B1, but for HD 181433.

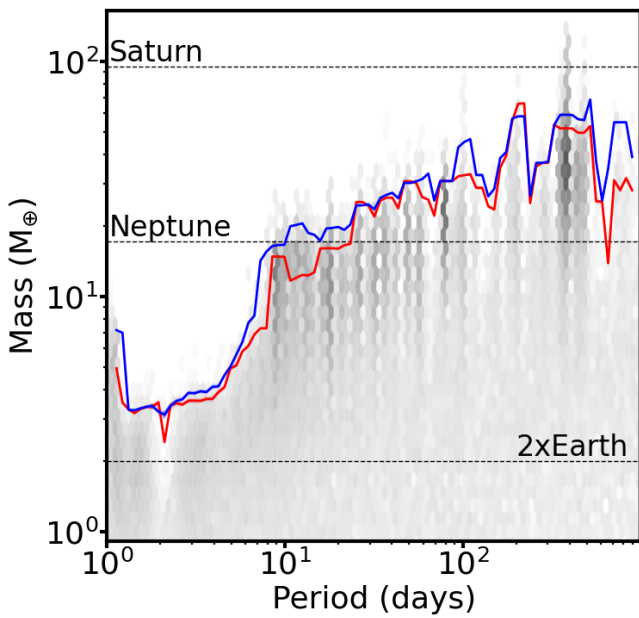


Figure B18. As for Fig B1, but for HD 149189.

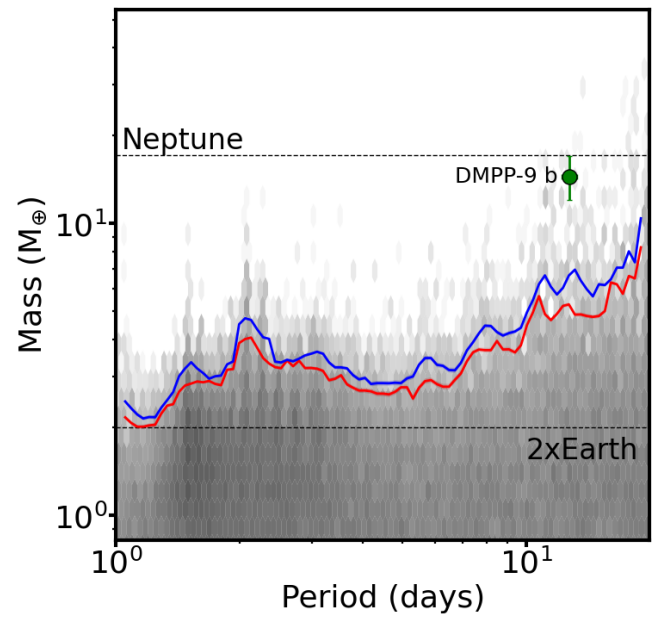


Figure B20. As for Fig B1, but for HD 200133 / DMPP-9.

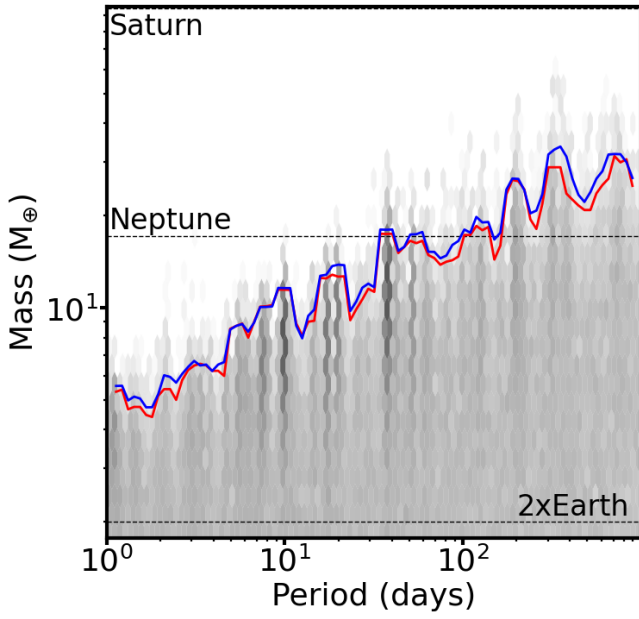


Figure B21. As for Fig B1, but for HD 210975.

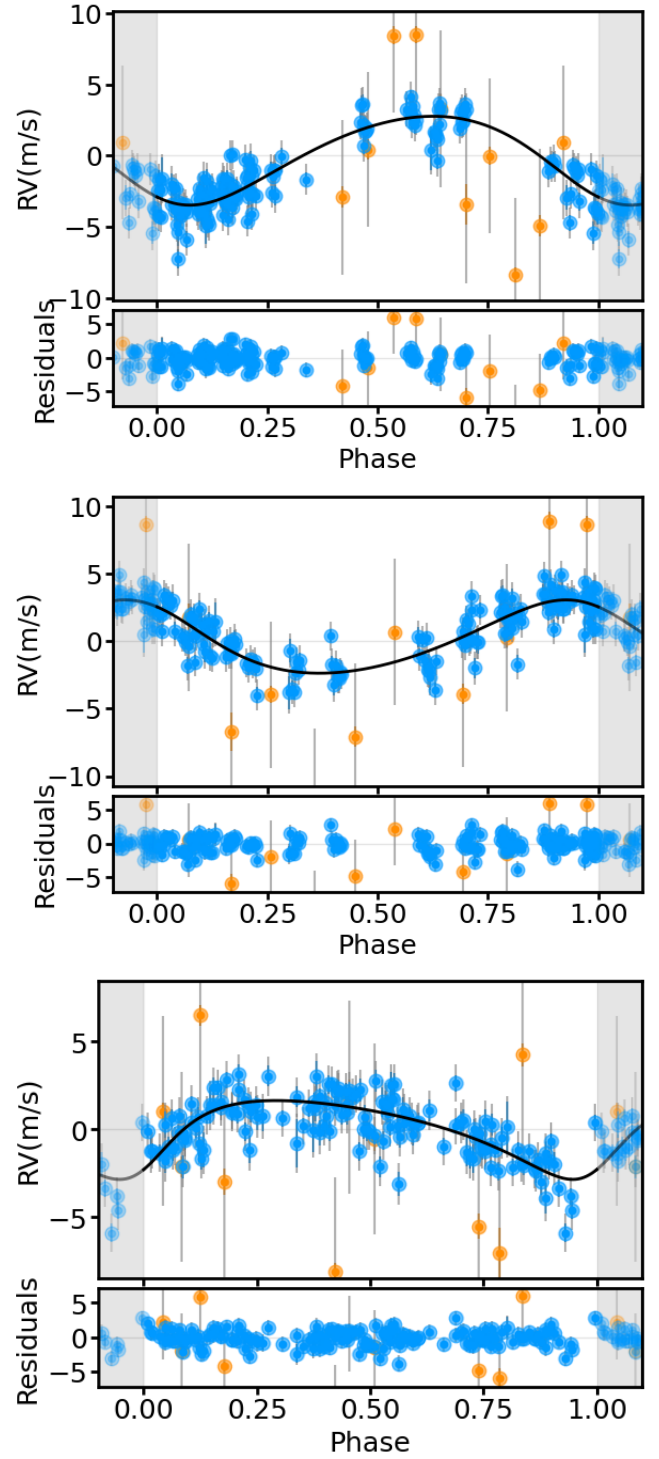


Figure D1. Phased Keplerian RV models of DMPP-1 b (top), DMPP-1 c (middle), and DMPP-1 d (bottom) with HARPS data post-fibre upgrade (blue) and post-COVID warm-up (orange) along with associated residuals after removing the planetary signals. The additional RV jitter term has been added to the plotted uncertainties and is shown by the grey error bars. No random samples are shown for this signal as the eccentricity is unconstrained and consistent with 0. The shaded regions display the repeating signal.

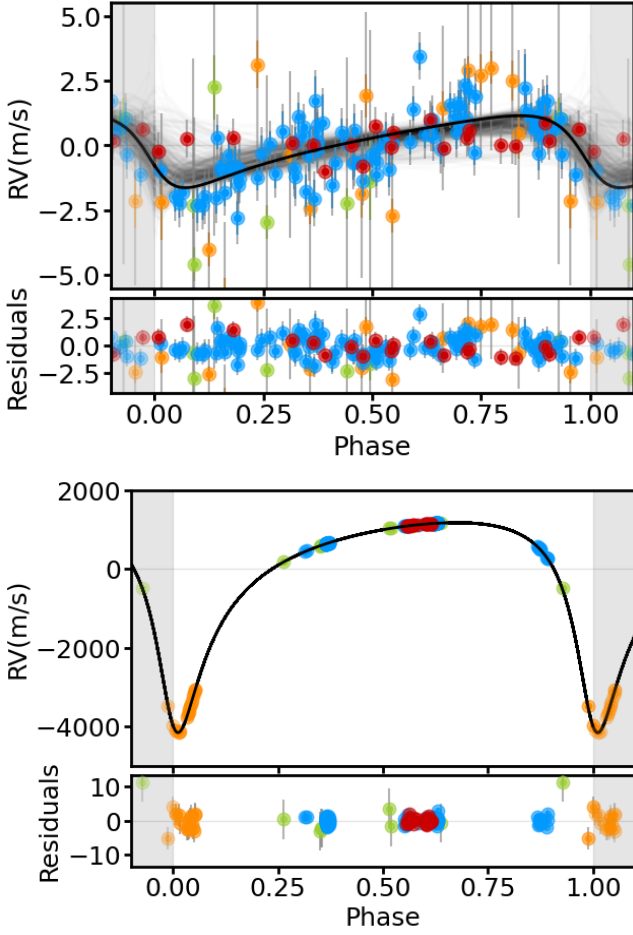


Figure D2. Phased Keplerian RV models of DMPP-3A b (top), DMPP-3B (bottom) with HARPS data pre-fibre upgrade (green), HARPS data post-fibre upgrade (blue), HARPS data post-COVID warm-up (orange) and ESPRESSO data (red) along with associated residuals after removing the planetary signal. The additional RV jitter term has been added to the plotted uncertainties and is shown by the grey error bars. No random samples are shown for this signal as the eccentricity is unconstrained and consistent with 0. The shaded regions display the repeating signal.

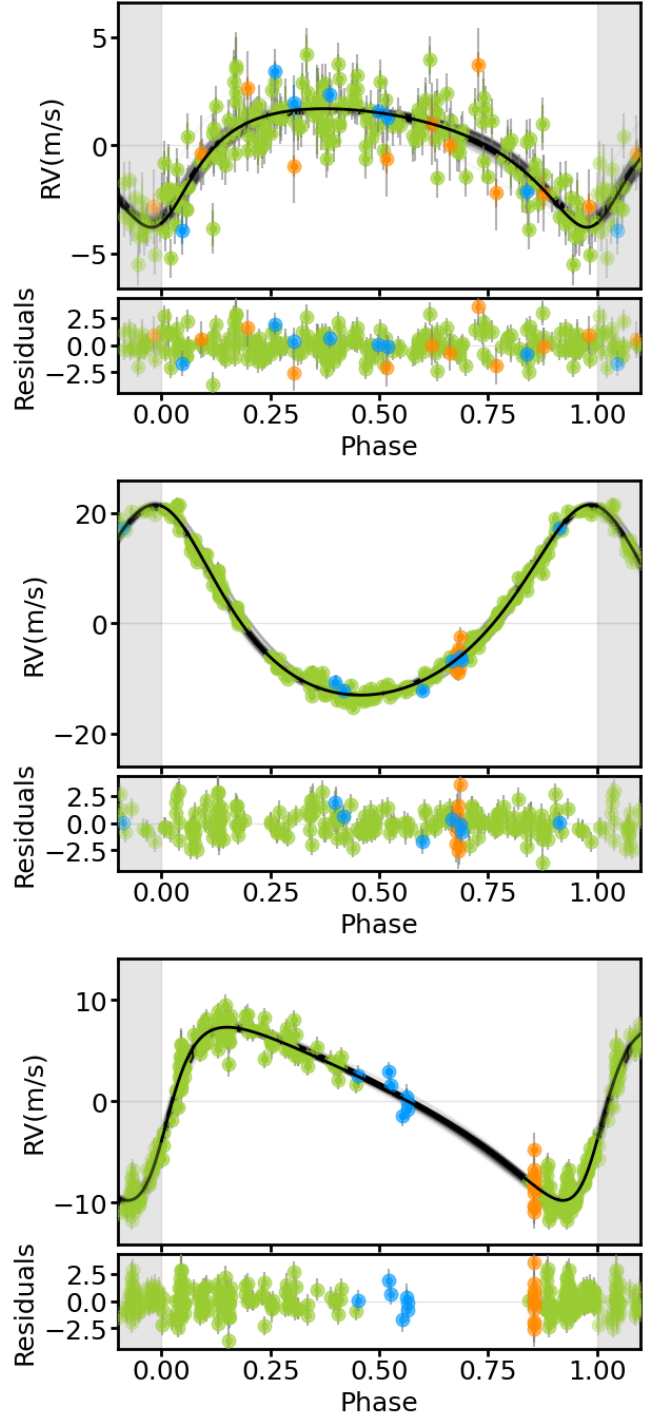


Figure D3. Phased Keplerian RV models of HD 181433 b (top), HD 181433 c (middle), and HD 181433 d (bottom) with HARPS data pre-fibre upgrade (green), HARPS data post-fibre upgrade (blue), HARPS data post-COVID warm-up (orange) and their respective residuals after removing the planetary signals. The additional RV jitter term has been added to the plotted uncertainties and is shown by the grey error bars. Faded Keplerian models are based on 500 randomly drawn posterior samples from a *kima* run. The shaded regions display the repeating signal.

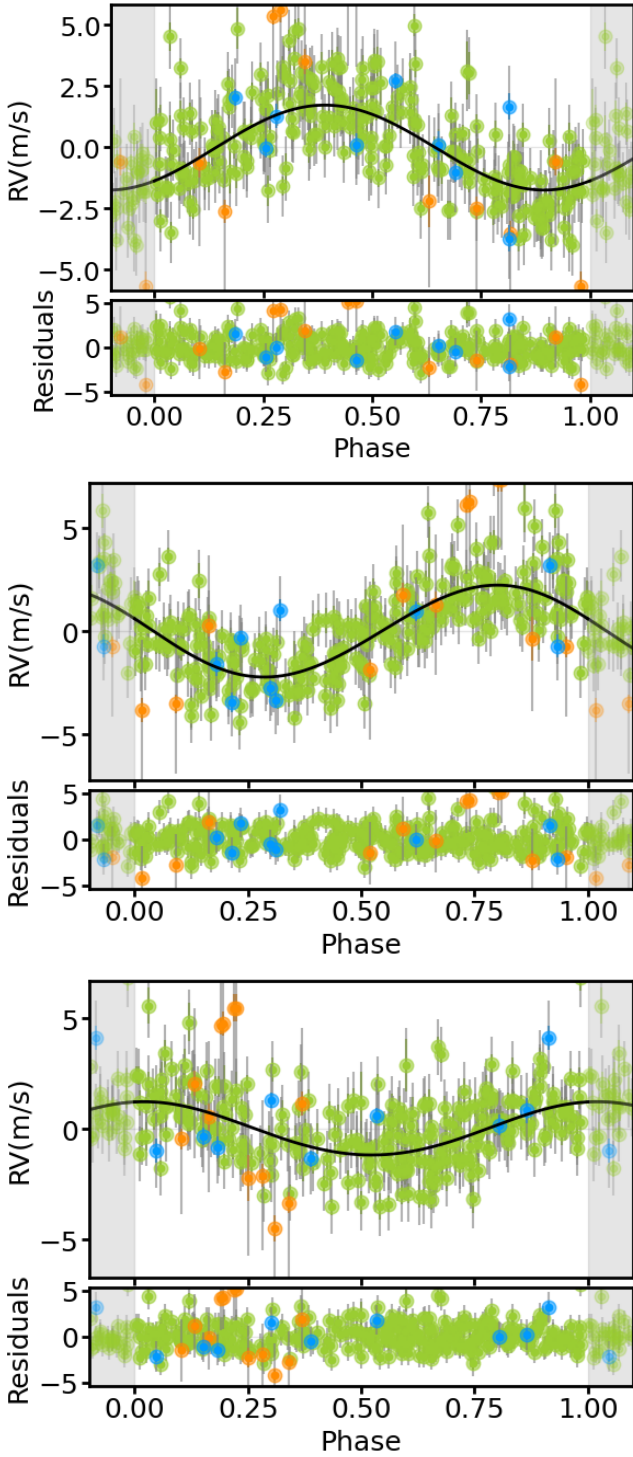


Figure D4. Phased Keplerian RV models of HD 39194 b (top), HD 39194 c (middle), and HD 39194 d (bottom) with HARPS data pre-fibre upgrade (green), HARPS data post-fibre upgrade (blue), and HARPS data post-COVID warm-up (orange) and their respective residuals after removing the planetary signals. The additional RV jitter term has been added to the plotted uncertainties and is shown by the grey error bars. No random samples are shown for this signal as the eccentricity is unconstrained and consistent with 0.. The shaded regions display the repeating signal.

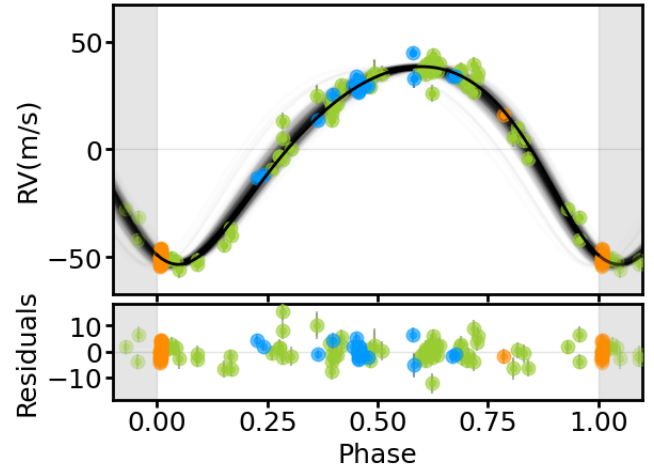


Figure D5. Phased Keplerian Radial-Velocity (RV) models of HD 89839 b with HARPS data pre-fibre upgrade (green), HARPS data post-fibre upgrade (blue), and HARPS data post-COVID warm-up (orange) and their respective residuals after removing the planetary signal. The additional RV jitter term has been added to the plotted uncertainties and is shown by the grey error bars. Faded Keplerian models are based on 500 randomly drawn posterior samples from a *kima* run. The shaded regions display the repeating signal.

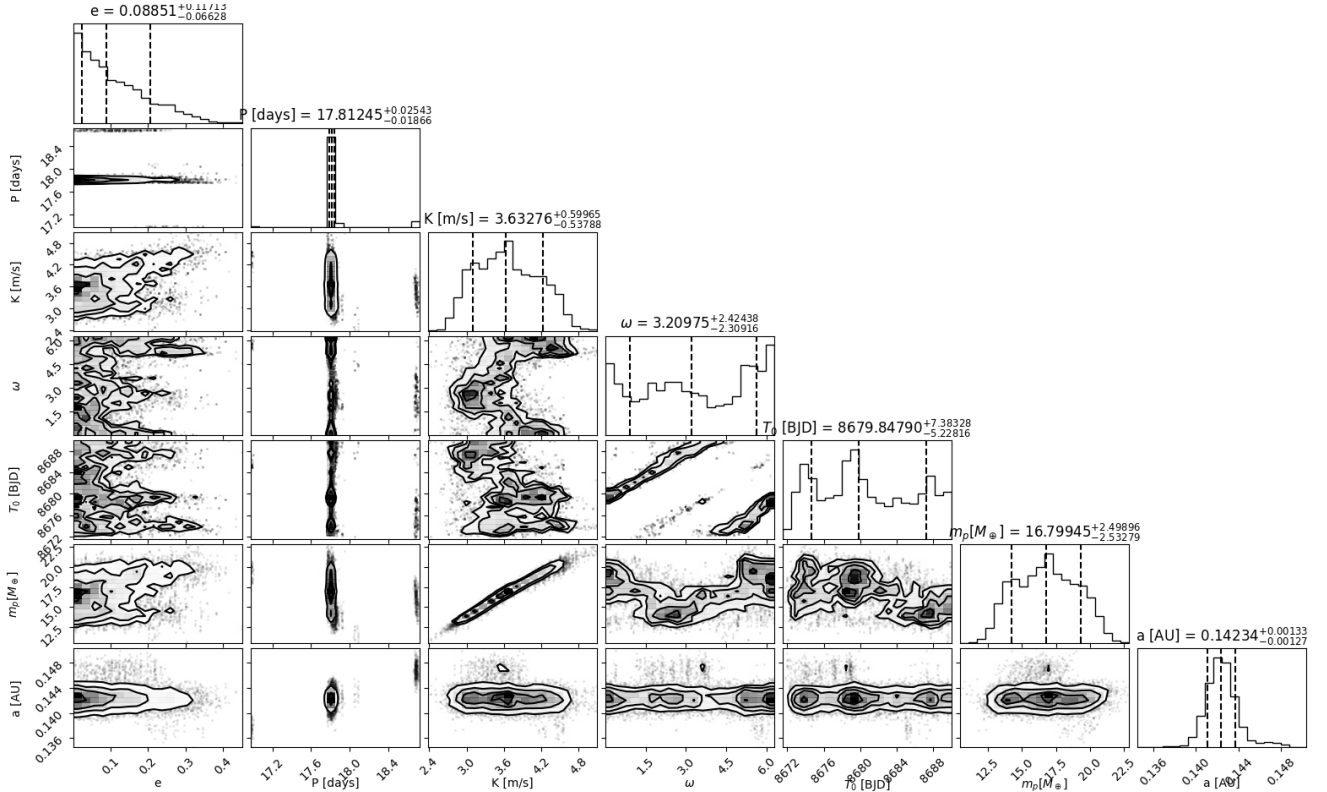


Figure E1. Corner plot for DMPP-1 b.

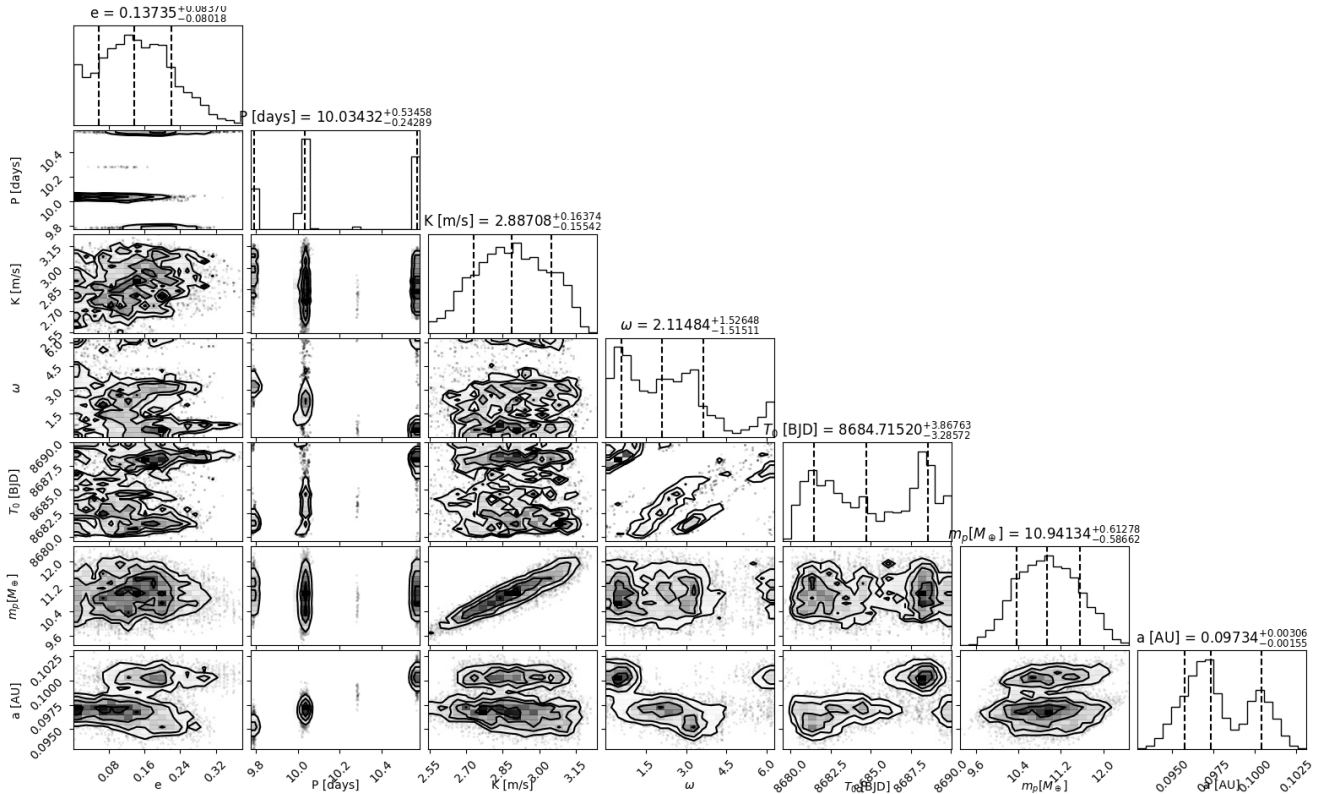


Figure E2. Corner plot for DMPP-1 c.

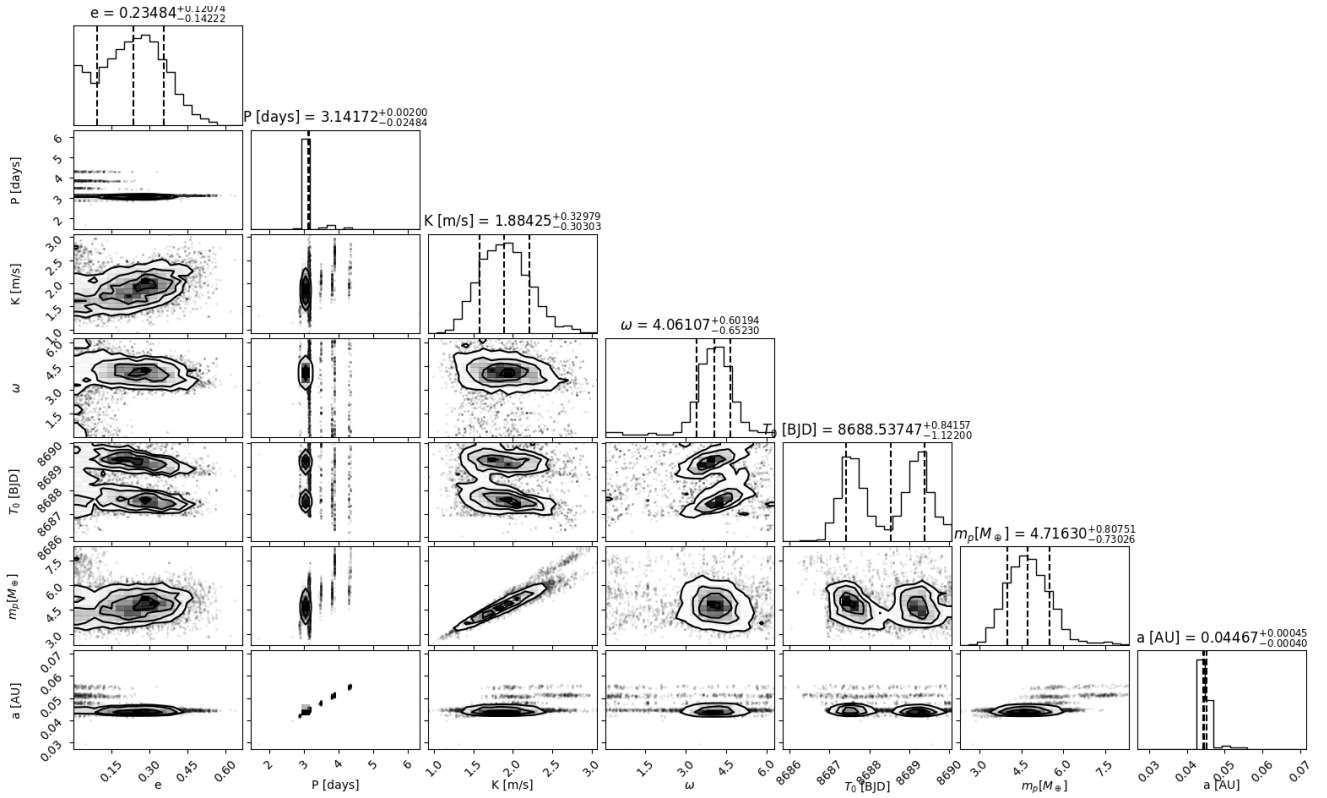


Figure E3. Corner plot for DMPP-1 d.

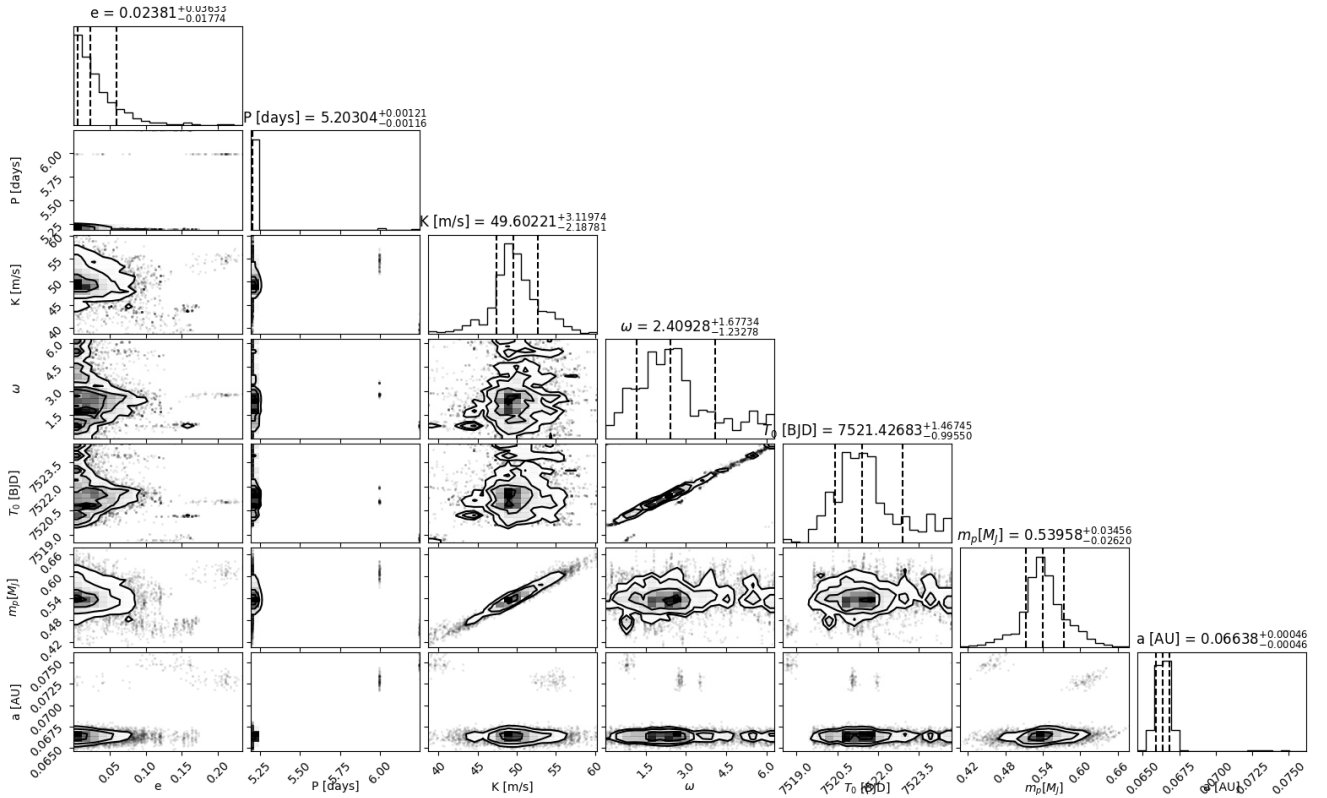


Figure E4. Corner plot for DMPP-2 b.

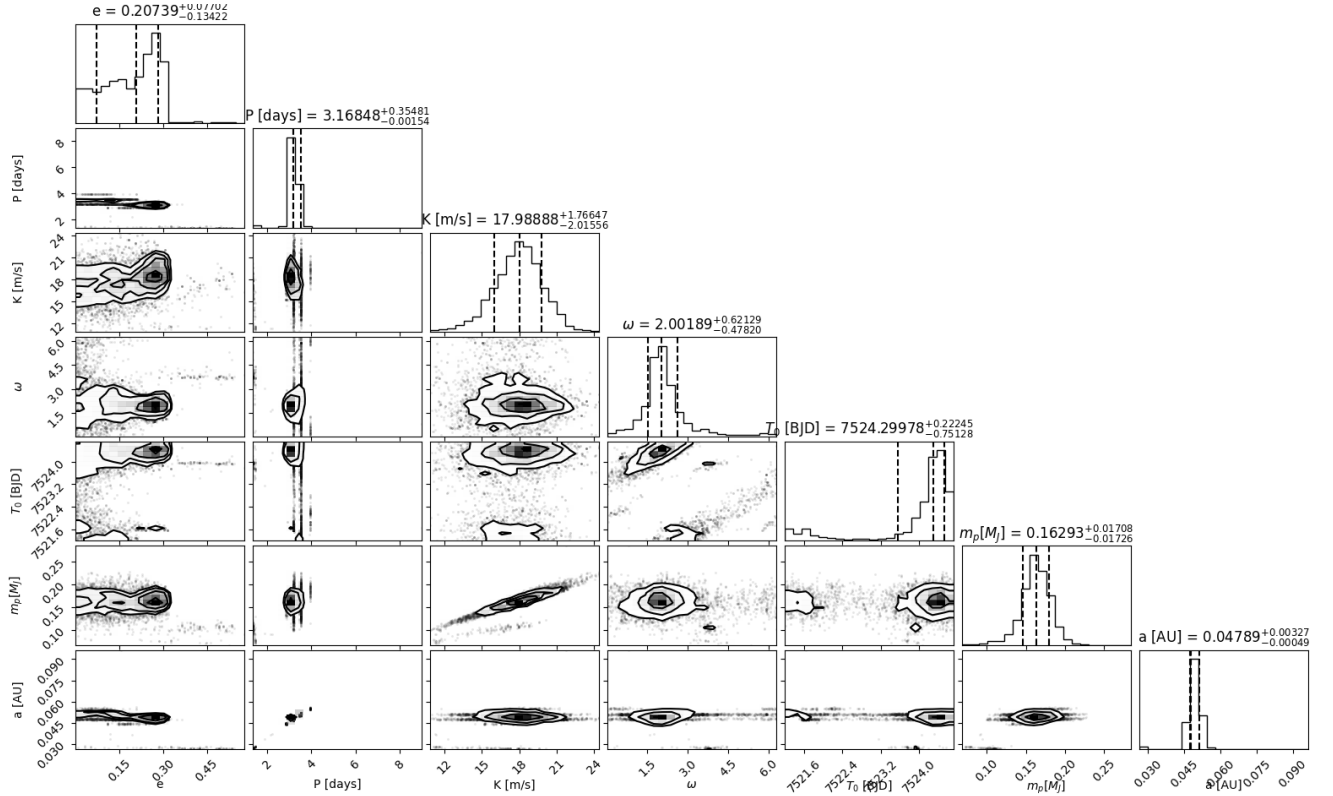


Figure E5. Corner plot for DMPP-2 c.

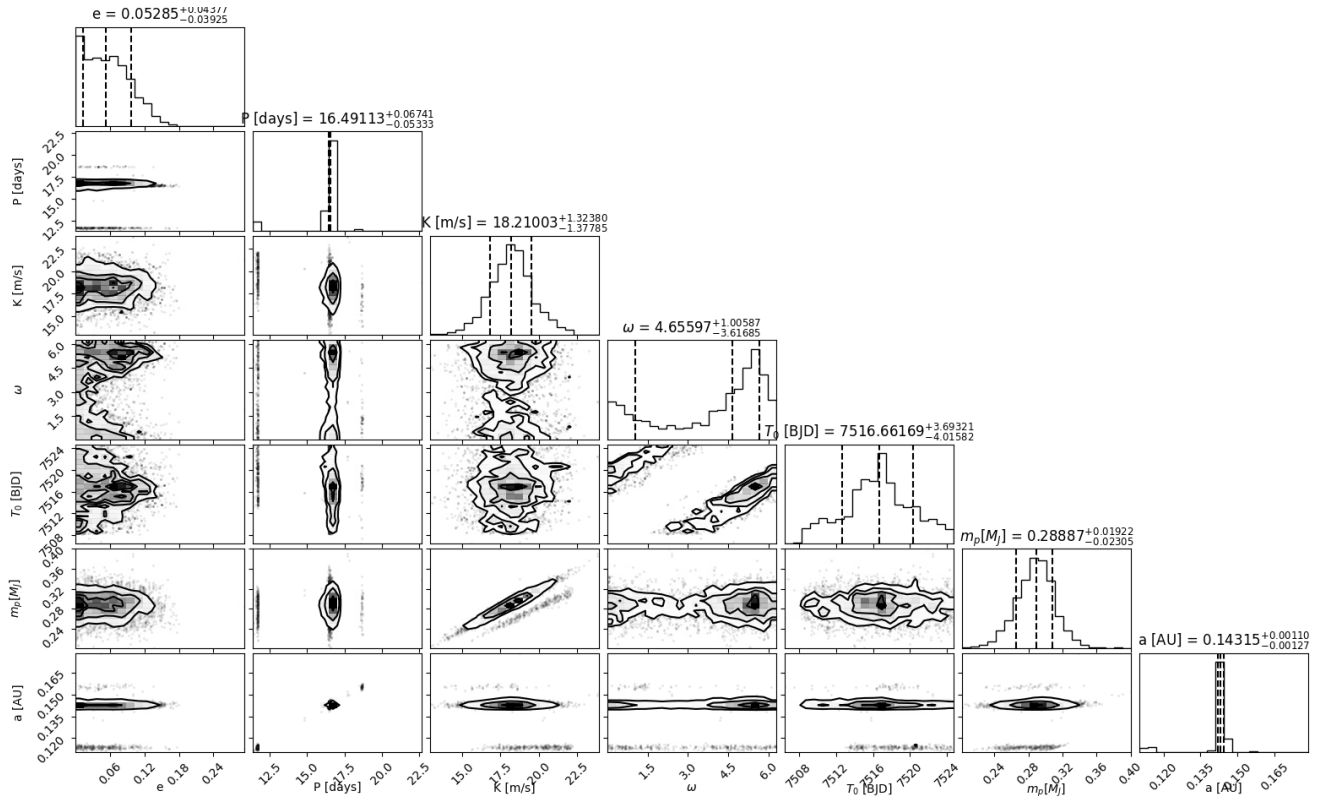


Figure E6. Corner plot for DMPP-2 d.

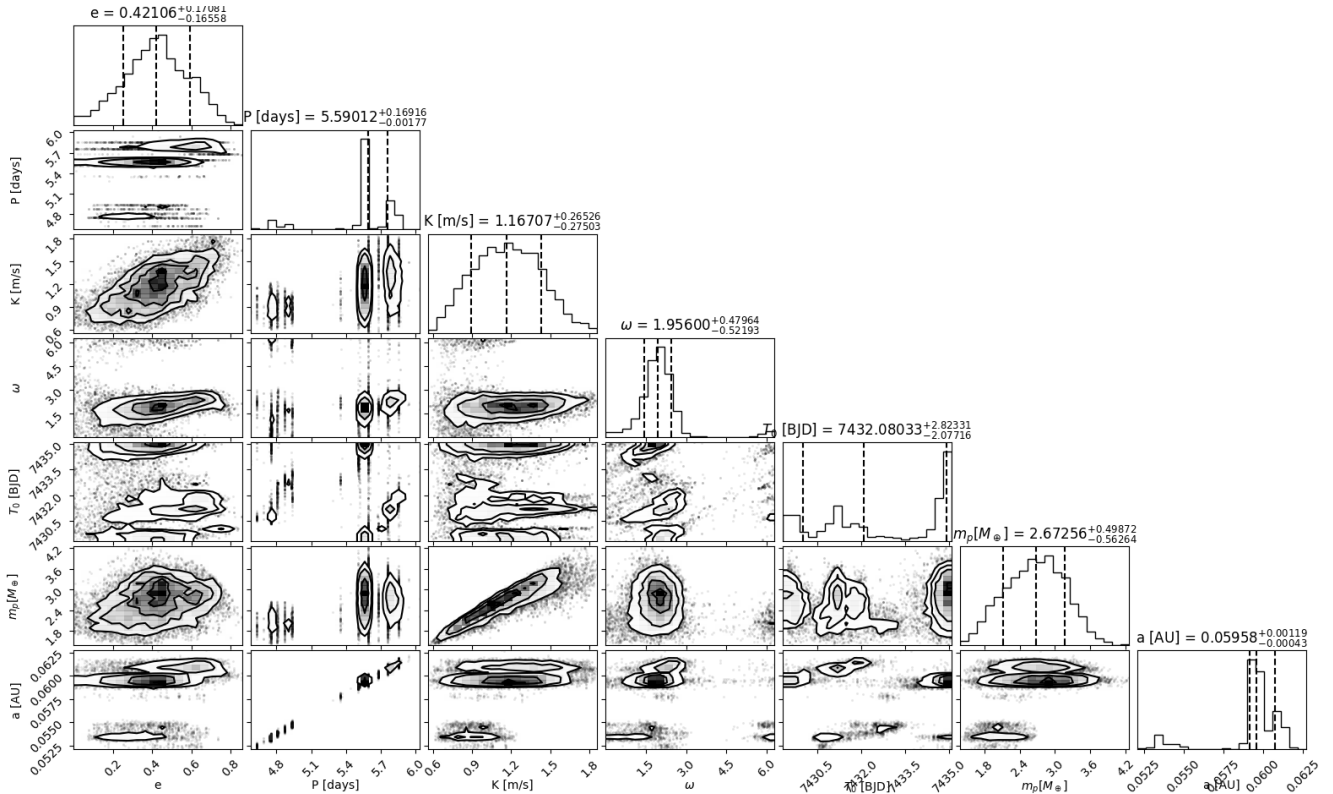


Figure E7. Corner plot for DMPP-3 b.

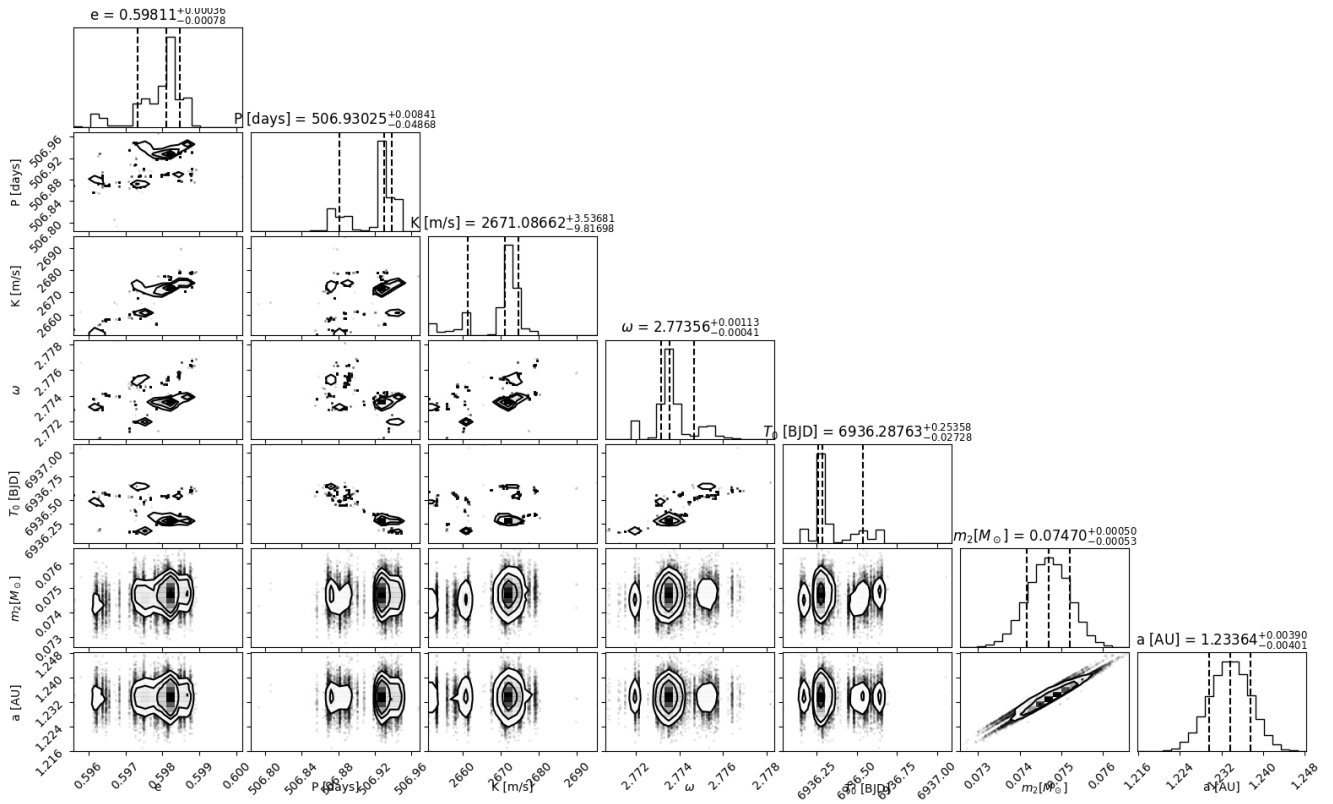


Figure E8. Corner plot for DMPP-3 AB.

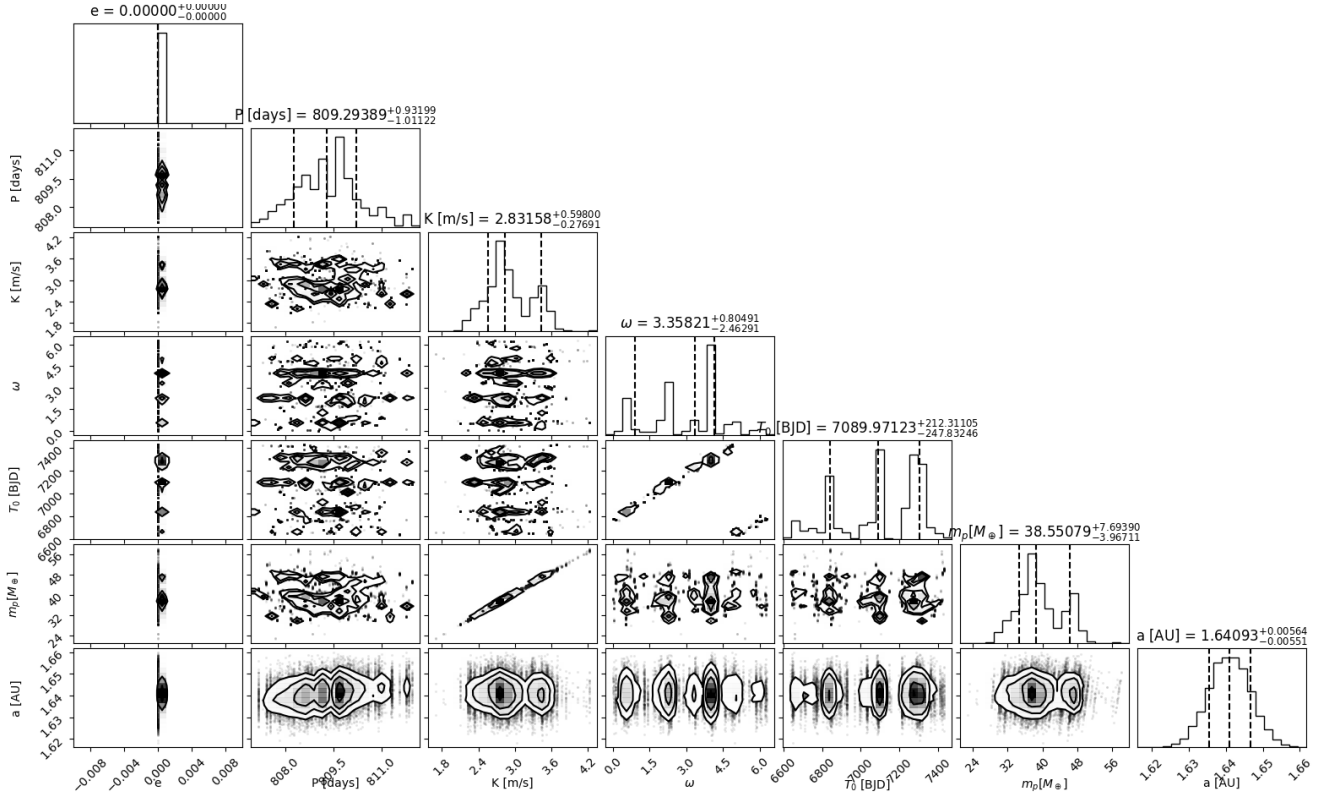


Figure E9. Corner plot for DMPP-3 800 d signal.

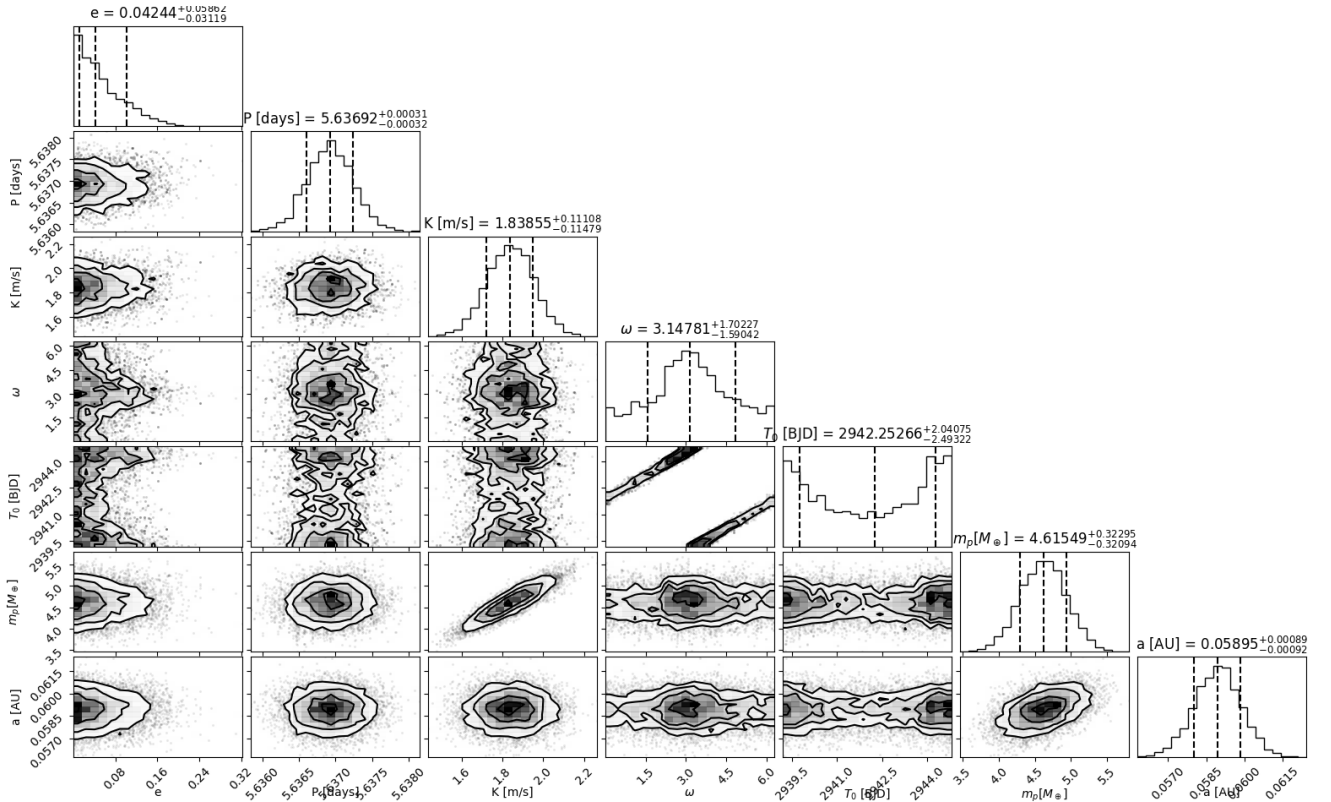


Figure E10. Corner plot for HD39194 b.

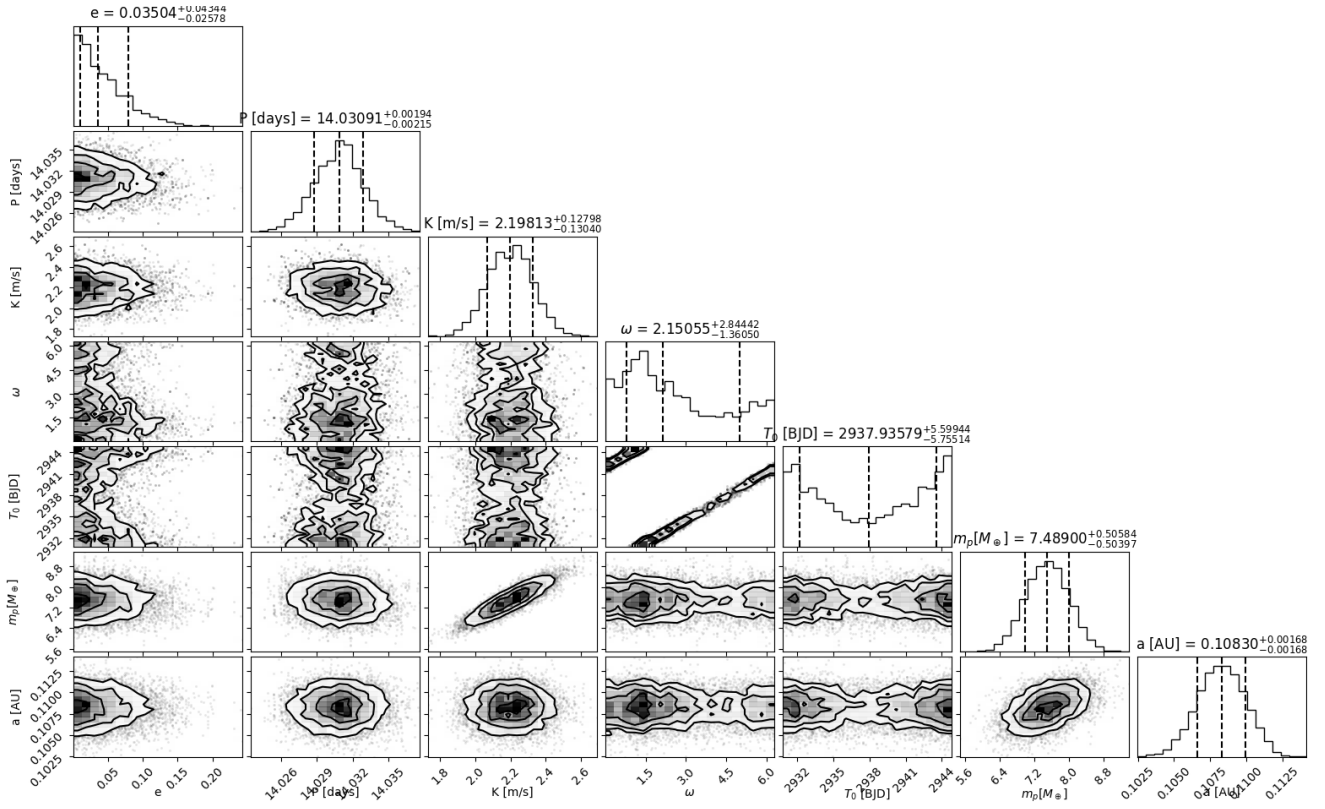


Figure E11. Corner plot for HD39194 c.

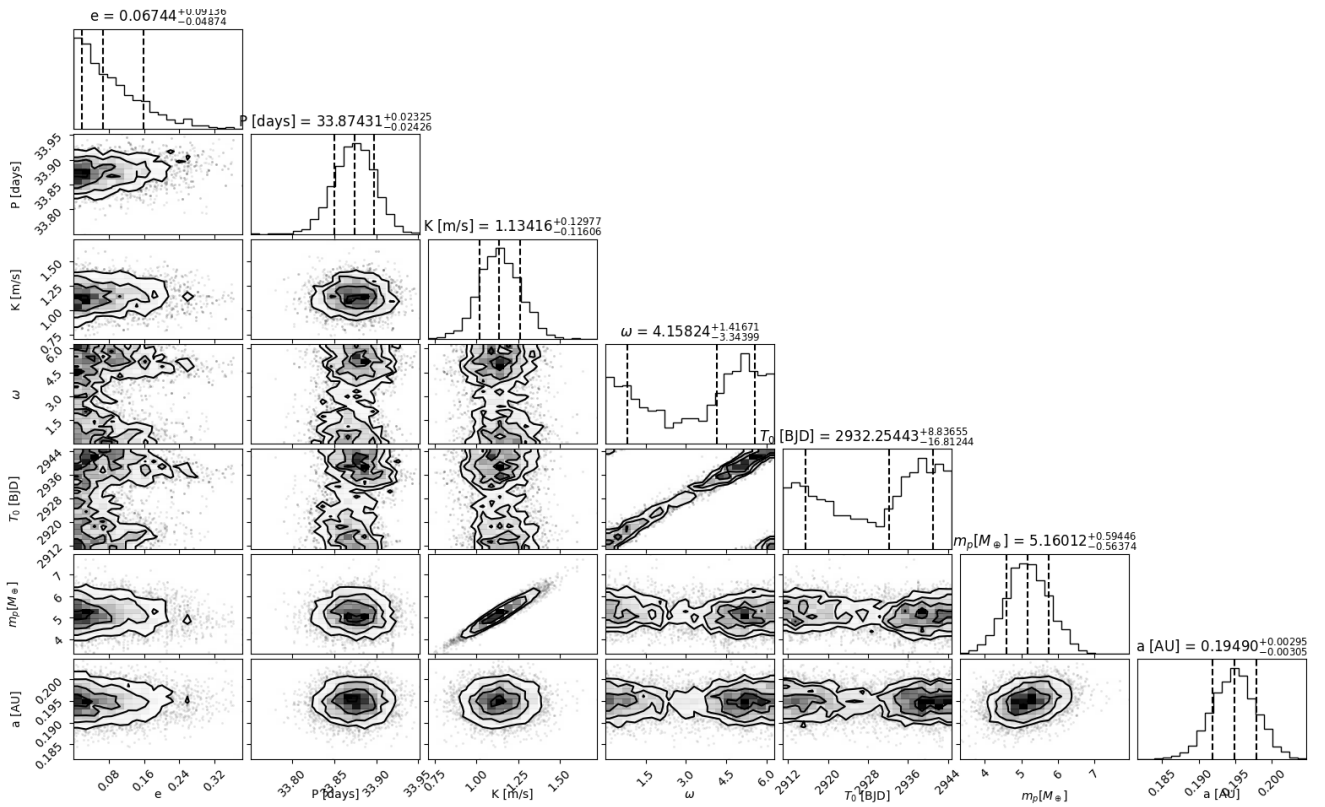


Figure E12. Corner plot for HD39194 d.

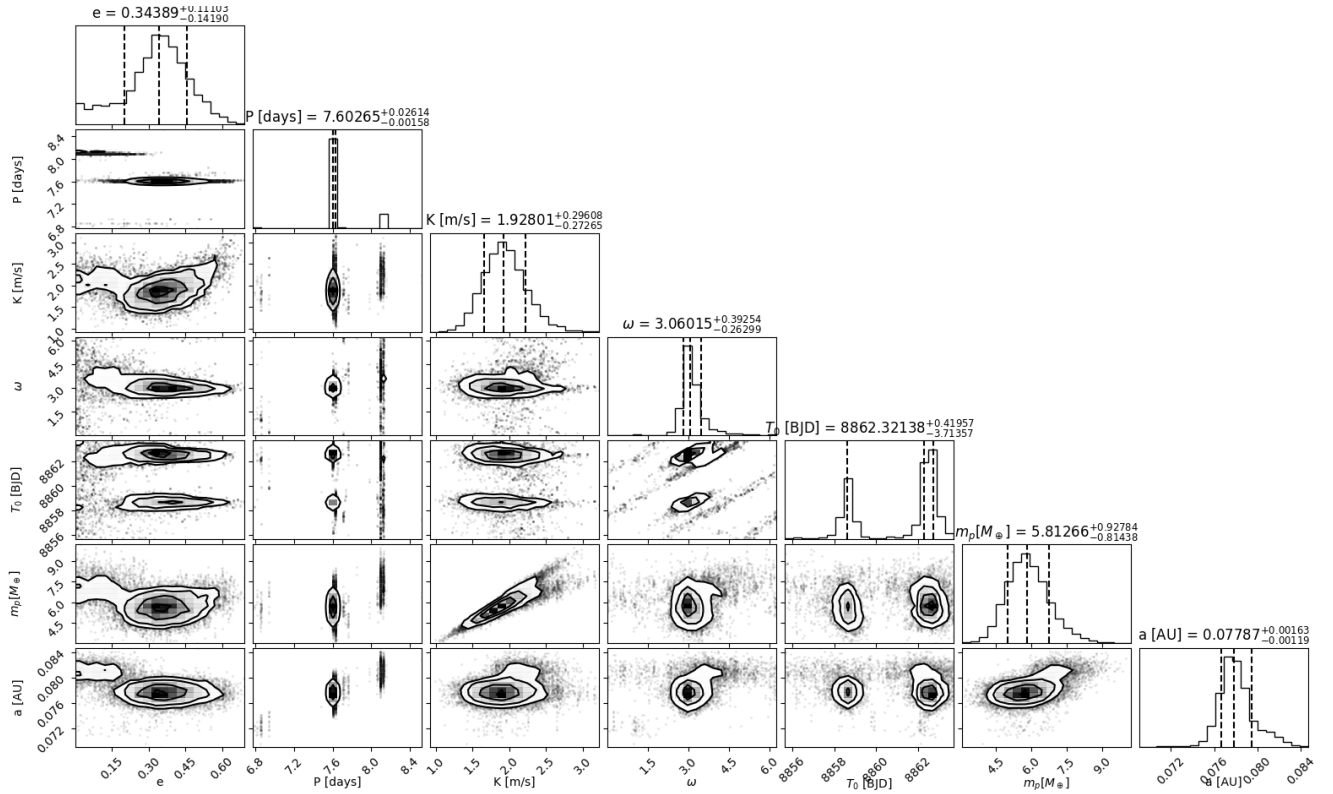


Figure E13. Corner plot for HD67200 / DMPP-6 b.

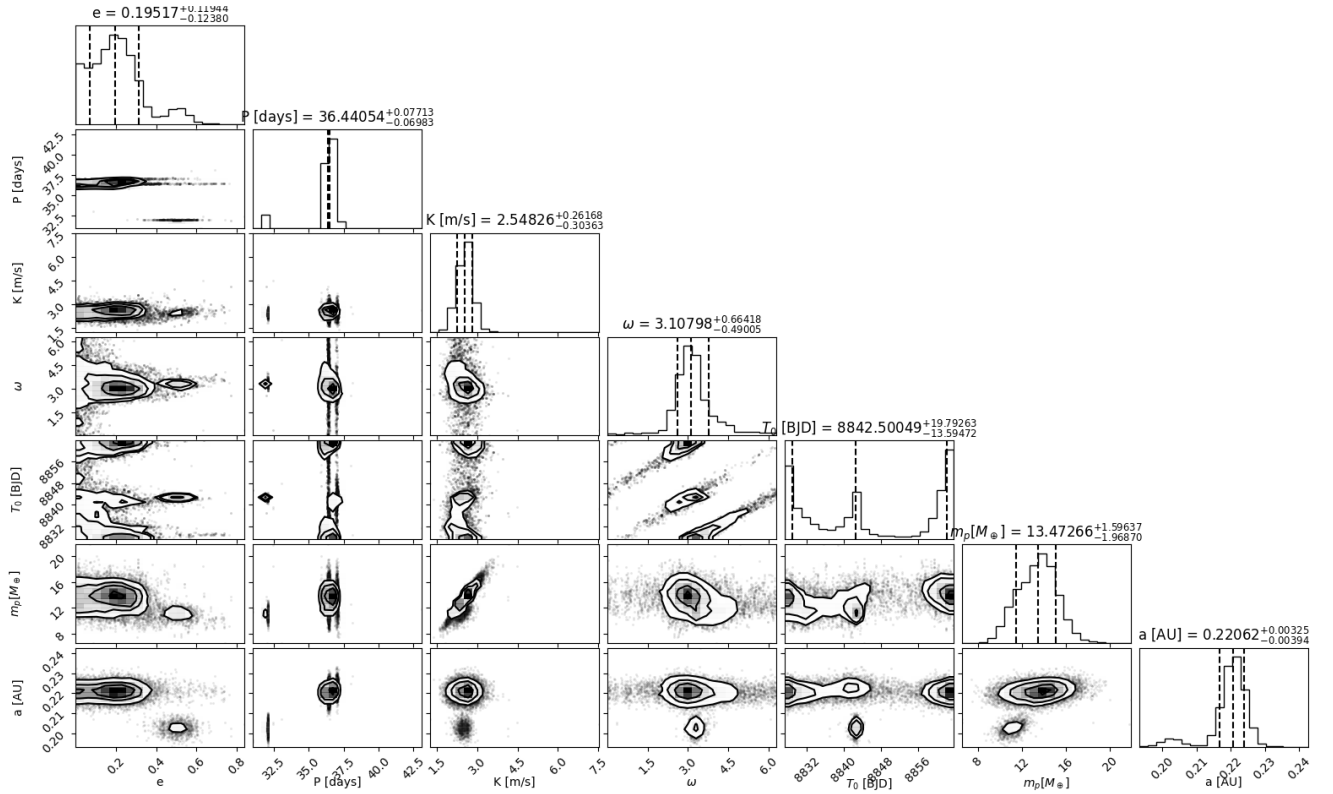


Figure E14. Corner plot for HD67200 / DMPP-6 c.

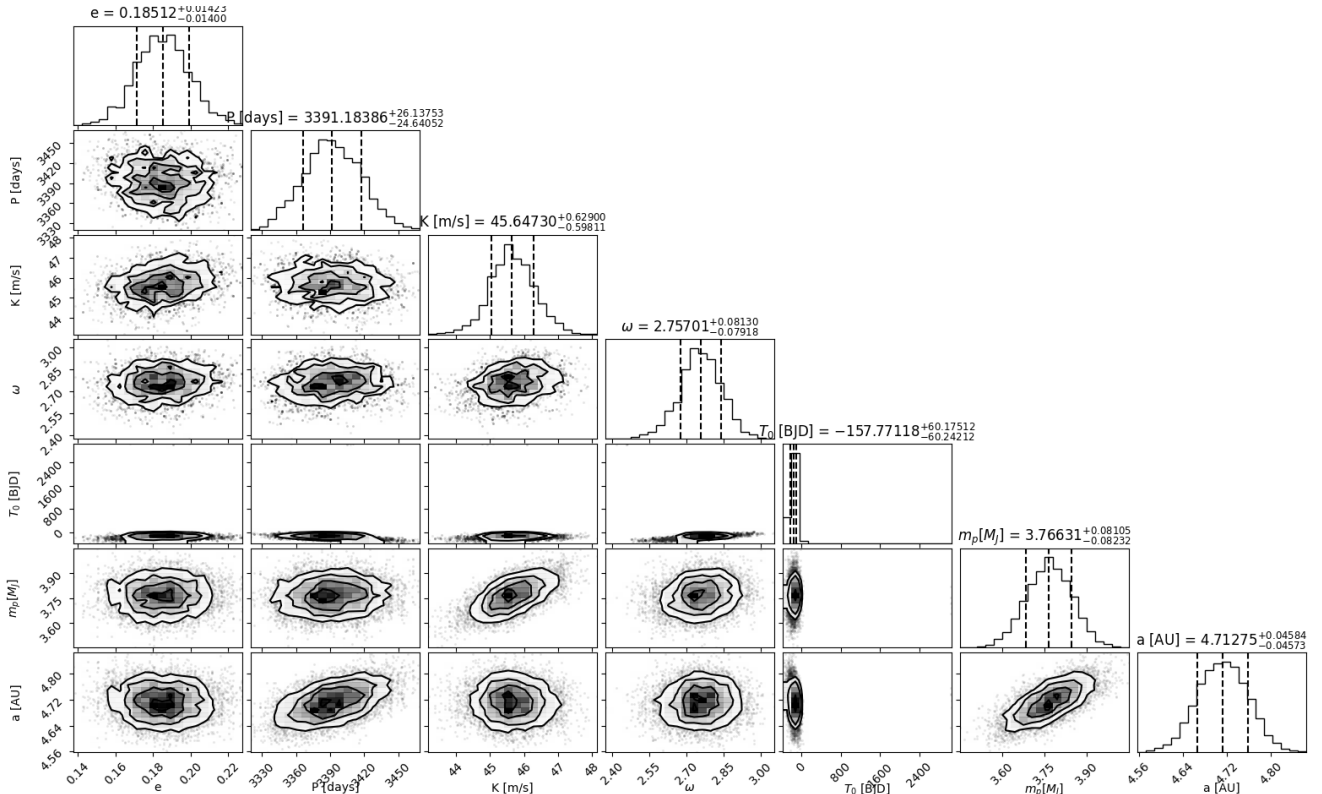


Figure E15. Corner plot for HD89839 b.

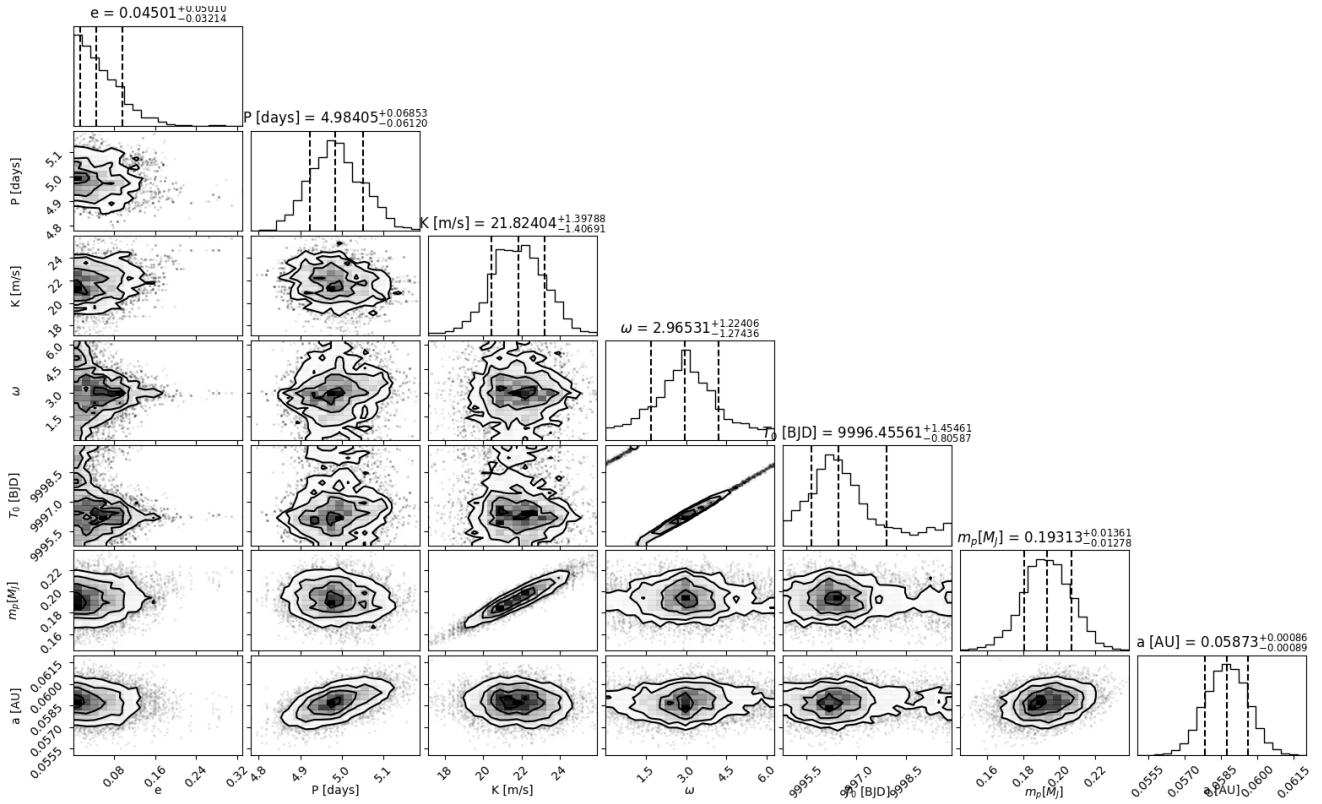


Figure E16. Corner plot for HD118006 / DMPP-7 b.

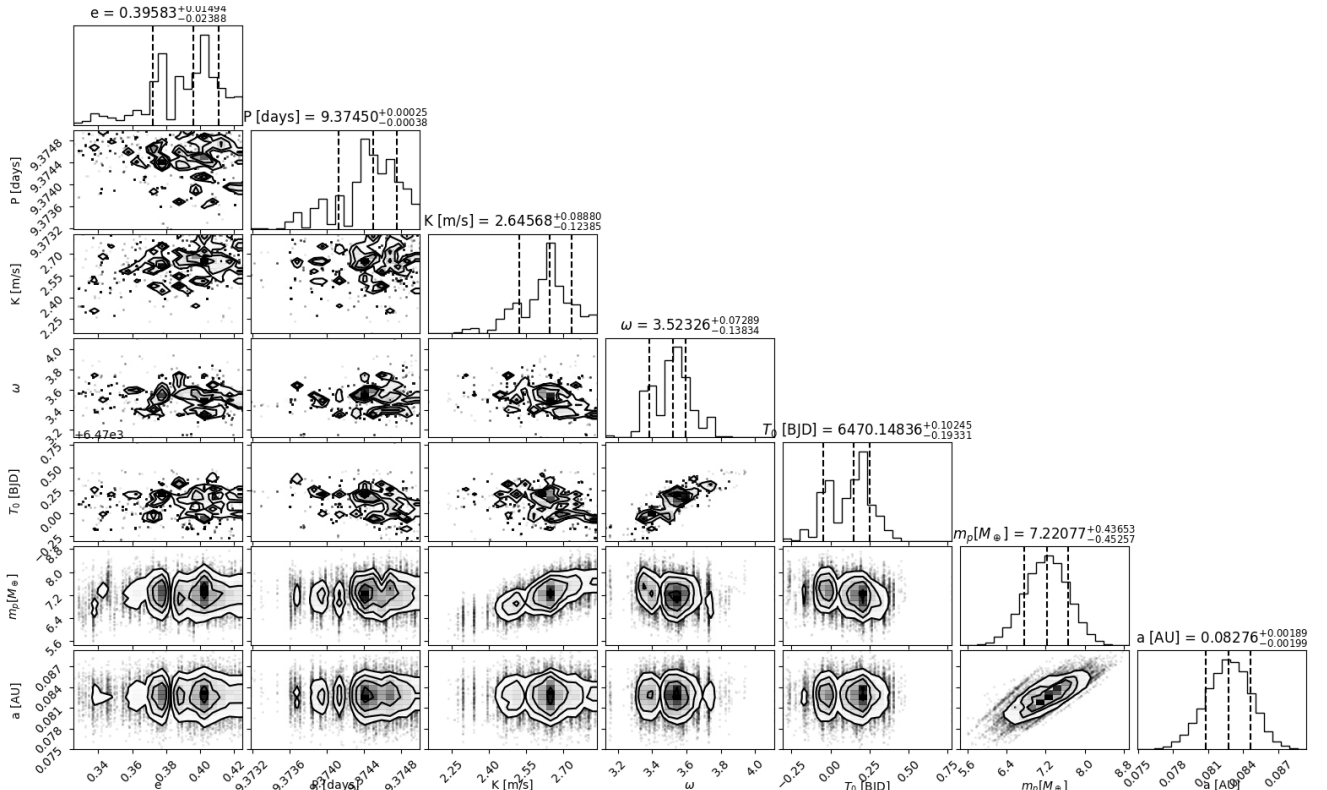


Figure E17. Corner plot for HD181433 b.

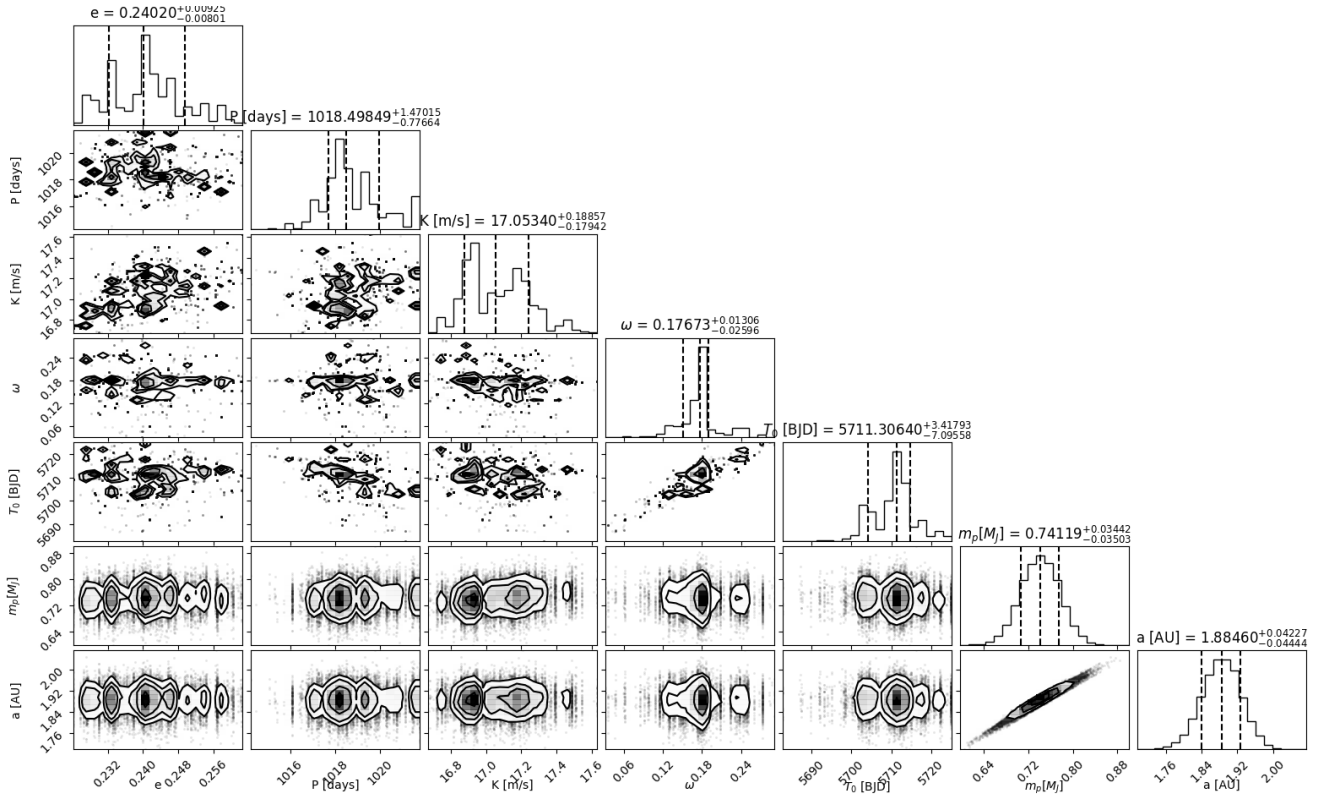


Figure E18. Corner plot for HD181433 c.

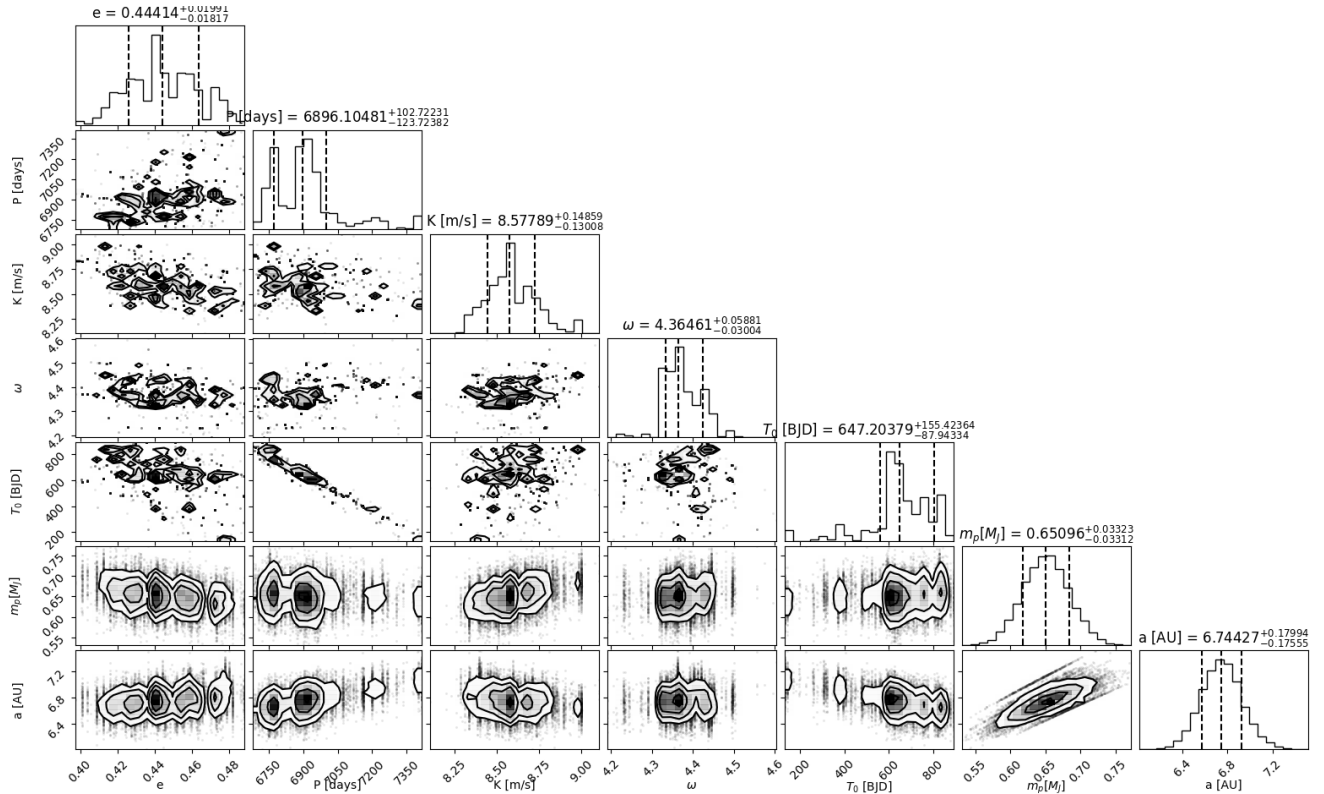


Figure E19. Corner plot for HD181433 d.

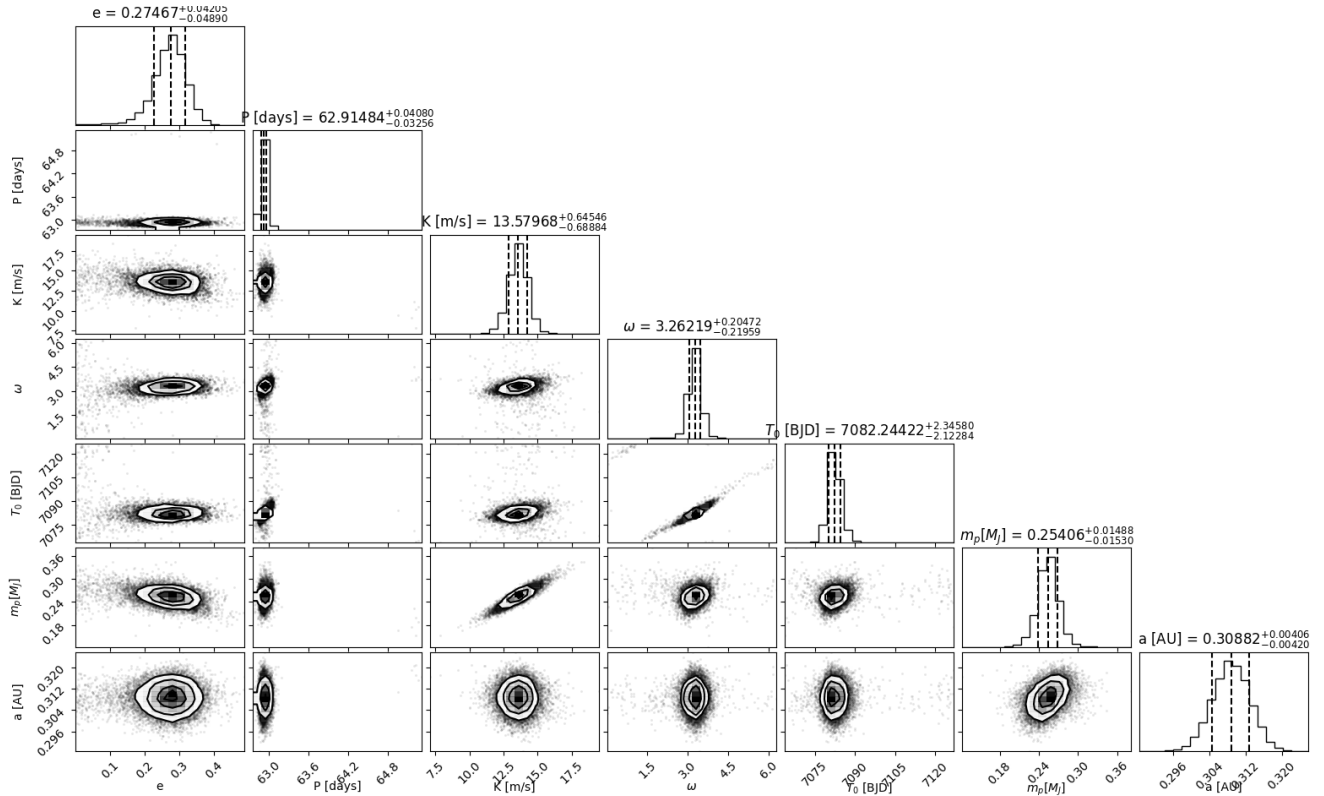


Figure E20. Corner plot for HD191122 / DMPP-8 b.

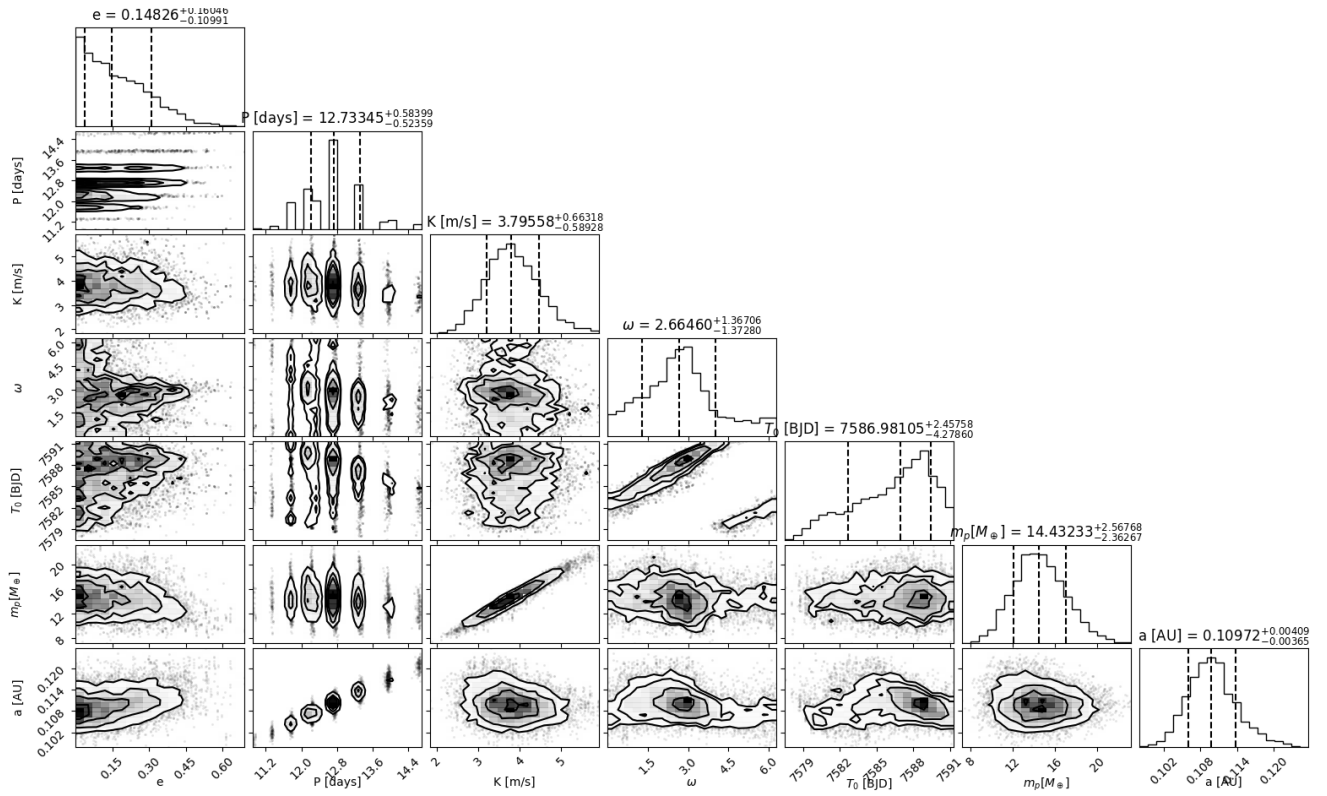


Figure E21. Corner plot for HD200133 / DMPP-9 b.